

AD-A271 329



2

**FINITE ELEMENT MESH GENERATION
AND ANALYSIS OF SOLDER JOINTS
FOR FATIGUE LIFE PREDICTIONS**

Final Report

N. Paydar, Y. Tong, H.U. Akay and W. Boehmer

August 1993

**DTIC
ELECTE
OCT 20 1993
S B D**

U.S. ARMY RESEARCH OFFICE

Grant No: 29042-MS

93-24856



**Department of Mechanical Engineering
Indiana University-Purdue University at Indianapolis
Indinapolis, Indiana 46202**

Approved for Public Release; Distribution Unlimited.

93 10 18 126

**Best
Available
Copy**

**FINITE ELEMENT MESH GENERATION
AND ANALYSIS OF SOLDER JOINTS
FOR FATIGUE LIFE PREDICTIONS**

Final Report

N. Paydar, Y. Tong, H.U. Akay and W. Boehmer

August 1993

U.S. ARMY RESEARCH OFFICE

Grant No: 29042-MS

**Department of Mechanical Engineering
Indiana University-Purdue University at Indianapolis
Indinapolis, Indiana 46202**

Approved for Public Release; Distribution Unlimited.

REPORT DOCUMENTATION PAGE			Form Approved OMB No. 0704-0188	
<small>Public reporting burden for this collection of information is estimated to average 1 hour per response, including the time for reviewing instructions, searching existing data sources, gathering and maintaining the data needed, and completing and reviewing the collection of information. Send comments regarding this burden estimate or any other aspect of this collection of information, including suggestions for reducing this burden, to Washington Headquarters Services, Directorate for Information Operations and Reports, 1215 Jefferson Davis Highway, Suite 1204, Arlington, VA 22202-4302, and to the Office of Management and Budget, Paperwork Reduction Project (0704-0188), Washington, DC 20503.</small>				
1. AGENCY USE ONLY (Leave blank)	2. REPORT DATE August 30, 1993	3. REPORT TYPE AND DATES COVERED <i>Final, 19 Jul 91 - 30 Jun 93</i>		
4. TITLE AND SUBTITLE Finite Element Mesh Generation and Analysis of Solder Joints for Fatigue Life Predictions		5. FUNDING NUMBERS <i>DAAL03-91-G-0187</i>		
6. AUTHOR(S) N. Paydar, Y. Tong, H.U. Akay and W. Boehmer				
7. PERFORMING ORGANIZATION NAME(S) AND ADDRESS(ES) Department of Mechanical Engineering Indiana University - Purdue University Indianapolis 723 W. Michigan Street SL 2250 Indianapolis, Indiana 46202-5132		8. PERFORMING ORGANIZATION REPORT NUMBER		
9. SPONSORING / MONITORING AGENCY NAME(S) AND ADDRESS(ES) U.S. Army Research Office P.O. Box 12211 Research Triangle Park, NC 27709-2211		10. SPONSORING MONITORING AGENCY REPORT NUMBER <i>ARO 29042.1-M5</i>		
11. SUPPLEMENTARY NOTES The views, opinions and/or findings contained in this report are those of the author(s) and should not be construed as an official Department of the Army position, policy, or decision, unless so designated by other documentation.				
12a. DISTRIBUTION / AVAILABILITY STATEMENT Approved for public release; distribution unlimited.		12b. DISTRIBUTION CODE		
13. ABSTRACT (Maximum 200 words) Tools for fatigue life prediction of solder joints are developed. This report consists of two parts. In Part One, the creep and plastic deformations stored in a solder joint are calculated by implementing appropriate plastic and creep constitutive models in a nonlinear finite element program. The calculated damage in each cycle is then related to the life of the material using two failure criteria: strain-life and energy-partitioning. The importance of parameters affecting the fatigue life of solders are evaluated. In Part Two, the finite element analysis is combined with x-ray and laser imaging systems, from which real solder joint geometries can be constructed. The approaches presented herein provide a useful tool in the design and manufacturing of surface-mount assemblies.				
14. SUBJECT TERMS Solder, Solder Joint, Fatigue Life, Creep, Thermal Stress, Finite Element Analysis, Mesh Generation.		15. NUMBER OF PAGES 164		16. PRICE CODE
17. SECURITY CLASSIFICATION OF REPORT UNCLASSIFIED	18. SECURITY CLASSIFICATION OF THIS PAGE UNCLASSIFIED	19. SECURITY CLASSIFICATION OF ABSTRACT UNCLASSIFIED	20. LIMITATION OF ABSTRACT UL	

TABLE OF CONTENTS

ABSTRACT.....	1
 PART ONE FINITE ELEMENT ANALYSIS OF CREEP RESPONSE FOR FATIGUE LIFE CALCULATIONS	
1. STATEMENT OF THE PROBLEM.....	3
2. FINITE ELEMENT ANALYSIS OF SOLDER JOINTS UNDER THERMAL CYCLIC LOADING	5
2.1 <i>Finite Element Mesh</i>	5
2.2 <i>Constitutive Relationships for Solder</i>	6
2.3 <i>Fatigue Life Prediction</i>	8
3. NUMERICAL RESULTS AND DISCUSSIONS.....	15
3.1. <i>A Two-dimensional Resistor-Joint-Board Assembly - A Parametric Study</i>	15
3.2. <i>A Three-dimensional Assembly of Three Joints</i>	21
3.3 <i>A Two-dimensional Resistor-Joint-Board Assembly -- Comparison with Experiments</i>	21
4. CONCLUSIONS	82
REFERENCES.....	85

PART TWO CREATION OF FINITE ELEMENT MESHES FROM INSPECTION MACHINES

1. STATEMENT OF THE PROBLEM.....	88
1.1 Solder Joint Inspection System.....	89
1.1.1 Laser-Vision Systems.....	89
1.1.2 X-Ray Systems	90
1.1.3 Solder Joints.....	90
2. CREATION OF MESHES FROM FOUR PI SYSTEM.....	93
2.1 Four Pi and Its Characteristics.....	93
2.2 Procedure for Creating Geometry	94
2.2.1 Knowledge Base	94
2.2.2 Image Acquisition.....	94
2.2.3 Image Processing	95
2.2.4 Image Segmentation	96
2.2.5 Image Recognition.....	97
2.2.6 Image Conversion.....	97
2.3 Generation of a Session File.....	97
2.4 Computer Program	98
2.4.1 Limitations of the Existing Program	99
2.4.2 Modifications of the Existing Program	99
2.4.3 Boundary Finding Techniques	100
2.5.3.1 Threshold Method	101
2.5.3.2 Gradient Method	101
2.5 3-D Reconstruction Process.....	102
3. CREATION OF MESHES FROM RVSI SYSTEM	113
3.1 RVSI and Its Characteristics	113
3.2 Procedure for Creating Geometry	113
3.2.1 Knowledge Base	114
3.2.2 Image Acquisition.....	115
3.2.3 Image Processing	115
3.2.4 Image Segmentation	116
3.3 Generation of a Session File.....	116

4. ADDITIONAL RESULTS AND DISCUSSIONS	140
4.1 Repeatability	140
4.2 Accuracy	141
4.3 Discussions	142
4.3.1 Four Pi Versus RVSI	142
4.3.1.1 Four Pi System	143
4.3.1.2 RVSI System	143
5. INTERACTIVE MESH GENERATION WITH RVSI DATA	152
5.1 Problems with Locating Boundaries	152
5.2 User Interaction	154
5.3 Generating the Mesh	154
6. CONCLUSIONS	157
REFERENCES	158
APPENDIX A	159
APPENDIX B	163
APPENDIX C	164

Accession For	
NTIS	<input checked="" type="checkbox"/>
DTIC TAB	<input type="checkbox"/>
Unannounced	<input type="checkbox"/>
Justification	
By	
Distribution/	
Availability Codes	
Dist	Avail and/or Special
A-1	

LIST OF FIGURES

PART ONE

Figure 2.1 Two dimensional solid model of solder-resistor-board assembly	14
Figure 3.1 A typical temperature loading used for thermal cycling	29
Figure 3.2 Maximum von Mises stress for different ramp times.....	30
Figure 3.3 Maximum equivalent total strain for different ramp times.....	31
Figure 3.4(a) Maximum equivalent plastic strain for different ramp times	32
Figure 3.4(b) Maximum equivalent creep strain for different ramp times	33
Figure 3.5(a) Maximum von Mises stress for different hold times.....	34
Figure 3.5(b) Maximum equivalent creep strain for different hold times	35
Figure 3.6(a) The distribution of von Mises stress (MPa) after 5 minutes ramp from 125°C to -55°C.....	36
Figure 3.6(b) The distribution of von Mises stress (MPa) after 10 minutes hold at -55°C.....	36
Figure 3.7(a) The distribution of equivalent creep strain after 5 minutes ramp from 125°C to -55°C.....	37
Figure 3.7(b) The distribution of equivalent creep strain after 10 minutes hold at -55°C.....	37
Figure 3.8 Maximum equivalent total strain versus time for different grain sizes	38
Figure 3.9 Maximum equivalent total strain versus time for different constitutive equations.....	39

Figure 3.10 Maximum von Mises stresses for different material constants	40
Figure 3.11 Maximum equivalent total strain for different material constants from Equation (2.9).....	41
Figure 3.12 Maximum equivalent total strains for different material constants from Equation (3.2).....	42
Figure 3.13 Elastic strain energy density at R	43
Figure 3.14 Plastic energy dissipation density at R	44
Figure 3.15 Creep energy dissipation density at R.....	45
Figure 3.16 Number of cycles to failure at the singularity point using both criteria.....	46
Figure 3.17 Number of cycles to failure at R=0.03 mm using both criteria	47
Figure 3.18(a) Maximum von Mises stress versus time of the cycle with 1.0E-5 sec ramp and 10 minutes hold for different Young's moduli.....	48
Figure 3.18(b) Maximum von Mises stress versus time of the cycle with 5 minutes ramp and 10 minutes hold for different Young's moduli	49
Figure 3.19(a) Maximum equivalent creep strain versus time of the cycle with 1.0E-5 sec ramp and 10 minutes hold for different Young's moduli.....	50
Figure 3.19(b) Maximum equivalent creep strain versus time of the cycle with 5 minutes ramp and 10 minutes hold for different Young's moduli.....	51
Figure 3.20 Maximum equivalent plastic strain versus time of the cycle with 1.0E-5 sec ramp and 10 minutes hold for different Young's moduli.....	52
Figure 3.21 Maximum equivalent total strain versus time of the cycle with 1.0E-5 sec ramp and 10 minutes hold for different Young's moduli.....	53
Figure 3.22(a) Maximum von Mises stress versus time for initial temperature conditions 125°C and -55°C	54
Figure 3.22(b) Maximum equivalent total strain versus time for initial temperature conditions 125°C and -55°C	55
Figure 3.23(a) 3-D finite element model.....	56

Figure 3.23(b) Maximum equivalent creep strain versus time for 2D and 3D models.....	57
Figure 3.24(a) Maximum von Mises stress versus time for different mesh refinements	58
Figure 3.24(b) Maximum equivalent total strain versus time for different mesh refinements	59
Figure 3.25(a) The distribution of von Mises stress (MPa) after 5 minutes ramp from 125°C to -55°C with the mesh of 232 elements.....	60
Figure 3.25(b) The distribution of von Mises stress (MPa) after 5 minutes ramp from 125°C to -55°C with the mesh of 1701 elements.....	60
Figure 3.25(c) The distribution of equivalent creep strain after 10 minutes hold at 125°C with the mesh of 232 elements	60
Figure 3.25(d) The distribution of equivalent creep strain after 10 minutes hold at 125°C with the mesh of 1701 elements	60
Figure 3.26 A close proximity of the concentration points are chosen on the arc with its characteristic radius R for predicting fatigue.....	61
Figure 3.27 Number of cycles to failure of two mesh refinement using strain criterion	62
Figure 3.28 Number of cycles to failure using energy criterion	63
Figure 3.29(a) Number of cycles to failure as a function of hold time, predicted by Engelmaier equation.....	64
Figure 3.29(b) Number of cycles to failure as a function of hold time, predicted by Coffin-Manson equation.....	65
Figure 3.30 Three dimensional finite element mesh for a three-joint structure.....	66
Figure 3.31 Von Mises stress distribution after 5 minutes ramp from 125°C to -55°C	67
Figure 3.32 Von Mises stress distribution after 10 minutes hold at -55°C	68
Figure 3.33 Creep strain distribution after 5 minutes ramp from 125°C to -55°C	69
Figure 3.34 Creep strain distribution after 10 minutes hold at -55°C	70
Figure 3.35 Maximum von Mises stress versus time of a cycle for the three-joint structure	71

Figure 3.36 Maximum equivalent creep strain versus time of a cycle for the three-joint structure	72
Figure 3.37 Creep energy dissipation density.....	73
Figure 3.38 Temperature cycling profile	74
Figure 3.39 Finite element mesh of an assembly with void in solder joint.....	75
Figure 3.40 Maximum von Mises stress versus time of a cycle for an assembly with void in solder joint	76
Figure 3.41 Maximum creep strain magnitude versus time of a cycle for an assembly with void in solder joint.....	77
Figure 3.42 Creep energy dissipation density.....	78
Figure 3.43 Fatigue life of the solder predicted by both failure criteria	79
Figure 3.44 Finite element mesh of an assembly without void in the solder joint.....	80
Figure 3.45 Finite element mesh of an assembly with void in the solder joint - a different mesh refinement from Figure 3.39	81

PART TWO

Figure 1.1 Surface-mount chip resistor.....	92
Figure 2.1 Scanned-beam laminography.....	105
Figure 2.2 Four Pi problem solving flow chart.....	106
Figure 2.3 Typical laminography of a chip resistor	107
Figure 2.4 Bimodal gray level histogram	108
Figure 2.5 Thickness versus gray scale.....	108
Figure 2.6 Flagging first pair of data points	109
Figure 2.7 Flagging second pair of data points	110
Figure 3.1 RVSI problem solving flow chart	120
Figure 3.2 Type A joint.....	121
Figure 3.3 Type B joint.....	122
Figure 3.4 Manufacture's design specifications of the chip resistor	123
Figure 3.5 Output data points from RVSI HR-2000	124
Figure 3.6 Raw data from slice 26	125
Figure 3.7 Averaged data from slice 26.....	125

Figure 3.8 Grid points of slice 34 of the solder joint imaged by laser vision.....	126
Figure 3.9 Closed curve of slice 34.....	127
Figure 3.10 Method 1 (Hyperpatches from cross-sectional patches)	128
Figure 3.11 Method 2 (Hyperpatches from surface patches)	129
Figure 3.12 Lines fitted and drawn to the grid points (method 1).....	130
Figure 3.13 Edge patches defined by the lines (method 1).....	131
Figure 3.14 Hyperpatches defined between two patches (method 1)	132
Figure 3.15 Finite element mesh (method 1)	133
Figure 3.16 Solid model (method 1).....	134
Figure 3.17 Line fitted and drawn to the grid points (method 2)	135
Figure 3.18 Surface patches defined by the lines (method 2)	136
Figure 3.19 Hyperpatches defined by surface patches (method 2)	137
Figure 3.20 Finite element mesh (method 2).....	138
Figure 3.21 Solid model (method 2).....	139
Figure 4.1 Dimensions (in mils) of known solder object.....	146
Figure 4.2. Comparison of known solder object with Four Pi imaging results.....	147
Figure 4.3. Different camera settings showing how the distortion can change for the same known solder object used in Figure 4.2.....	148
Figure 4.4. Mesh obtained from the modified program using Four Pi data	149
Figure 4.5. Side view comparison of Four Pi results (purple) to RVSI results (red).....	150
Figure 4.6. Mesh obtained from program using RVSI data	151
Figure 5.1 The finite element mesh obtained from the interactive method	156

LIST OF TABLES

PART ONE

Table 2.1 The values of coefficients in Equation (2.1)	13
Table 2.2 The elastic and thermal expansion properties of the materials.	13
Table 3.1 The effect of grain size on the number of cycles to failure (5 min ramp, 10 min hold)	23
Table 3.2 The comparison of the results using different constitutive laws (5 min ramp, 10 min hold)	23
Table 3.3 Elastic materials properties at room temperature (24°C)	24
Table 3.4(a) Elastic, plastic, and creep strains, and the number of cycles to failure at the singularity point (887-element mesh)	25
Table 3.4(b) Strain energy, plastic energy dissipation, and creep energy dissipation values, and the number of cycles to failure at singularity point (887-element mesh)	25
Table 3.5(a) Elastic, plastic, and creep strains, and the number of cycles to failure at $R = 0.03$ mm (887-element mesh)	26
Table 3.5(b) Strain energy, plastic energy dissipation, and creep energy dissipation values, and the number of cycles to failure at $R = 0.03$ mm (887 element mesh)	26
Table 3.6(a) Elastic, plastic, and creep strains, and the number of cycles to failure at the maximum strain point (three-joint model)	27
Table 3.6(b) Strain energy, plastic energy dissipation, and creep energy dissipation values, and the number of cycles to failure at the maximum strain and stress point (three -joint model)	27
Table 3.7(a) Elastic, plastic, and creep strains, and the number of cycles to failure at the maximum strain point (JPL model)	28

Table 3.7(b) Strain energy, plastic energy dissipation, and creep energy dissipation values, and the number of cycles to failure at the maximum strain and stress point (JPL model).....	28
Table 4.1 CPU times for some typical 2D cases	84

PART TWO

Table 1.1 Summary of the evaluation parameters for the different solder joint inspection systems	91
Table 2.1 Typical 3X3 edge finding filters.....	104
Table 2.2 Gradient 3X3 edge finding filters	104
Table 3.1 Portion of RVSI HR-2000 data slice	119
Table 4.1 Repeatability test results of the known object.....	145
Table 5.1 Pad height of select portion of four slices from RVSI results	155

FOREWORD

The findings presented in this report are based on a research activity initiated by a grant from U.S. Army Research Office to study and develop predictive methods for reliability and manufacturability of solder joints. The work was monitored by George K. Lucey and his group at U.S. Army Research Laboratory at Adelphi, Maryland. In order to investigate the use of state-of-the-art solder inspection machines for modeling of solder geometries, an access to two inspection systems: *Four Pi* and *RVSI*, was provided by Electronics Manufacturing Productivity Facility (EMPF) at Indianapolis, Indiana.

The authors would like to acknowledge the support and encouragement of several individuals to this project. These include: George K. Lucey, Andrew Bayba and Abraham Frydman from U.S. Army Research Laboratory; Gary Burkart, Harold Rife and Rick James from EMPF.

The algorithms studied for the *Four Pi* x-ray system were based on the previous development of David Read of National Institute of Standards and Technology (NIST) at Boulder, Colorado; the solder inspection data utilized in developing the mesh generation procedures for solder geometries were obtained with the assistance of Tony Burnet and Ken Reid of EMPF. Their contribution to this project is gratefully appreciated.

ABSTRACT

Tools for fatigue life prediction of solder joints are developed. This report consists of two parts. In Part One, the creep and plastic deformations stored in a solder joint are calculated by implementing appropriate plastic and creep constitutive models in a nonlinear finite element program. The calculated damage in each cycle is then related to the life of the material using two failure criteria: strain-life and energy-partitioning. The importance of parameters affecting the fatigue life of solders are evaluated. In Part Two, the finite element analysis is combined with x-ray and laser imaging systems, from which real solder joint geometries can be constructed. The approaches presented herein provide a useful tool in the design and manufacturing of surface-mount assemblies.

PART ONE

**FINITE ELEMENT ANALYSIS OF CREEP
RESPONSE FOR FATIGUE LIFE
CALCULATIONS**

1. STATEMENT OF THE PROBLEM

Pb-Sn solder alloys have been used extensively in electrical connections because of their softness and low melting temperature. Due to its viscoplastic nature, large creep and plastic deformations accumulate in a solder joint during thermal cycling, which eventually lead to thermal fatigue failures. The reliability of the solder joints subjected to thermal fatigue loading has become one of the critical issues in modern electronic packaging. Many attempts have been made in understanding the basic mechanisms involved, but most of them remain as an empirical or at best a semi-empirical approach. Sophisticated methods are needed to determine the damage stored in each cycle and relate this damage to the life of the material. The purpose of this study is to develop a fatigue life prediction approach based on finite element method, associated with the deformation mechanisms, and failure mechanism of solder joints, to evaluate the importance of parameters affecting fatigue life of solders. Many progress have been made during this study (Paydar *et al.*, 1992, 1993, Akay *et al.*, 1993). We have shown that by interacting with laminography and laser vision system, a real solder joint geometry can be constructed and analyzed. This approach will guide the mechanical design process toward higher reliability and longer life cycle for devices.

A reliable life prediction of solder requires an accurate determination of creep and plastic deformations and the resulting stresses developed during thermal cyclic loads. The present work illustrates the use of plastic flow and creep constitutive models for solder joints under thermal loads, using the finite element program ABAQUS (1989). Several finite element models of solder joints are generated. Due to the large number of iterations involved in an elasto-plastic-creep analysis, a 3D finite element modeling and analysis is very time consuming. Therefore, majority of the analyses presented here are performed based on two-dimensional plane stress models, which have been

proven giving very close results when compared with the respective results of the 3D model. At the sametime, we have generated and analyzed a few three-dimensional finite element models of real solder geometry from RVSI and X-ray imaging. The procedures of generating the finite element models from these image are demonstrated and results are discussed.

Following a thermal stress analysis, the total strain and energy magnitude in each cycle calculated from the finite element method are converted to the fatigue life to failure using two failure criteria: strain-life and energy-partitioning. The results are compared to establish the appropriateness and range of applicability of each approach. The relative merits of each approach are discussed.

The parameters studied for fatigue life predictions include: ramp time, hold time, grain size, initial temperature, constitutive equations, material properties for solder alloys, mesh refinement, voids in the solder joint, and three-dimensional effects. The effects of these variations on the fatigue life of solder joints are illustrated. The calculated results have also been compared with the experimental observations.

2. FINITE ELEMENT ANALYSIS OF SOLDER JOINTS UNDER THERMAL CYCLIC LOADING

The prediction of the fatigue life of a solder joint requires a thorough understanding of the deformation and failure mechanisms of solder alloy, and a sophisticated methodology to accurately calculate the strains and stresses in the solder joint. The finite element method is chosen here because of its capability of solving complex non-linear problems and the availability of pre- and post-processing computer-aided modeling and analysis techniques. An elastic-plastic-creep model is adapted to investigate the solder joint performance under thermal cycling between 125°C and -55°C.

2.1 Finite Element Mesh

Finite element meshes for solder joints were generated using the finite element mesh generation program PATRAN (1990). A typical solder joint shown in Figure 2.1 is about 670 μm long, and 500 μm tall. It connects a resistor to an SMT board. The mesh of this model consists of 887 plane stress elements with 963 nodes. Assuming a symmetry plane, only half of the resistor geometry was considered. With x-symmetry along the right-hand edge, this model represents a two joint structure. On the symmetry plane the board was constrained in x-direction. To avoid any rigid body motion in the y-direction, the point on the right bottom corner of the board was constrained against the y-displacement.

2.2 Constitutive Relationships for Solder

The central problem in the study of high temperature creep is the choice of a reliable constitutive equation to represent the creep characteristics. Since a precise constitutive equation cannot be obtained, an empirical relation known as Dorn's Equation in the literature has been used here. According to Dorn's Equation, the creep deformation mechanism can be expressed by a power law expression (Lam *et al.*, 1979) in the form:

$$\dot{\epsilon} = \frac{AGb}{kT} \left(\frac{b}{d}\right)^p \left(\frac{\sigma}{G}\right)^n D_0 \exp(-Q/RT) \quad (2.1)$$

where $\dot{\epsilon}$ is the effective strain rate, σ is the equivalent stress, T is the absolute temperature, G is the shearing modulus, A is a dimensionless constant, d is the grain size (5.5×10^{-5} mm), b is the characteristic length of crystal dislocation (3.2×10^{-7}), D_0 is the frequency factor (100 mm^2), R is the gas constant, Q is the activation energy for plastic flow, k is the Boltzmann's constant, p is the grain size exponent, and n is the stress exponent. Choosing appropriate values of the four parameters A , Q , p and n , the high temperature deformation mechanism can be completely defined. The constants of Dorn's equation have been determined experimentally by several authors, e.g., Lam *et al.* (1979), Grivas *et al.* (1979), and Mohamed and Langdon (1976). The experimental procedure to obtain these constants are summarized in the following, based on the work done by Mohamed and Langdon (1975, 1976).

The specimens are tested using either an Instron testing machine or a constant-stress creep machine. On the Instron machine, the steady-state stress applicable to any imposed strain rate is determined using the established strain rate cycling procedure. On the creep machine, the steady-state strain rate applicable to any imposed stress is determined by stress cycling (Mohamed and Langdon, 1975, 1976).

The stress exponent n is determined from the logarithmic plot of $\dot{\epsilon}$ versus σ , i.e., $n = \partial(\ln \dot{\epsilon}) / \partial(\ln \sigma)$.

The strain rate dependence on grain size p is determined from the logarithmic plot of $\dot{\epsilon}$ versus d , i.e., $p = -\partial(\ln \dot{\epsilon}) / \partial(\ln d)$.

Following from Equation (2.1), the true activation energy for plastic flow is given by:

$$Q = -R \left(\frac{\partial \ln(\dot{\epsilon}) G^{n-1} T}{\partial (1/T)} \right) \quad (2.2)$$

The value A is obtained by setting $D_0 = 1 \text{ s}^{-1}$ and fitting Equation (2.1) to the experimental data.

The values of A , Q , p and n obtained by different authors are summarized in Table 2.1. As may be observed, there is a significant variation in the values determined by each investigator, especially for the dimensionless constant A in Equation (2.1). The effect of these different constants for Dorn's equation as well as a hyperbolic sine relation used by Pan (1991) on creep response have been studied during this project.

We have used the following temperature dependent relationships for the shearing modulus and yield stress of solder, respectively:

$$G(T) = 2.2 \times 10^4 - 16.1 \times T \quad \text{MN} / \text{m}^2 \quad (2.3)$$

$$\sigma_y(T) = 101.6 - 0.227 \times T \quad \text{MN} / \text{m}^2 \quad (2.4)$$

In addition, a 10 % strain hardening was assumed after the yield. These temperature-dependent properties together with the creep law given in Equation (2.1) were implemented into the non-linear finite element program ABAQUS (1989) with a user defined material subroutine. Table 2.2 gives the elastic and thermal expansion properties of the materials used in the model at different temperatures.

2.3 Fatigue Life Prediction

Failure Mechanisms. Early studies have discovered that several fatigue damage mechanisms exist in solder joints (Frear et al., 1990, Lau, 1991), which include: propagation of a major crack, wedge cracking at grain corners, and grain boundary cavitation. It has been adopted in solder fatigue research that fatigue crack initiation and growth is the dominant damage mechanism. Based upon this assumption, a number of fatigue life prediction models have been proposed. These include: strain-life relationship, and strain energy partitioning approaches.

Crack Propagation and Fatigue Life. Coffin (1954) and Manson (1965), working independently on the thermal fatigue problem, found that the low cycle fatigue data for many metals may be fit to the empirical plastic strain-life relation, which can be linearized on log-log coordinates in the following form:

$$\frac{\Delta \epsilon_p}{2} = \epsilon_f (2N_f)^c \quad (2.5)$$

where, $\frac{\Delta \epsilon_p}{2}$ is the plastic strain amplitude, ϵ_f is the fatigue ductility coefficient, N_f is the number of cycles to failure, and c is the fatigue ductility exponent. Many efforts have been made to explain the power-law relation between plastic strain range and life. Such an analysis was made by Manson (1965) and Solomon (1990), which is based on the assumption that a power-law relation between crack-growth rate and $\Delta \epsilon_p \sqrt{\ell}$, i.e.,

$$\frac{d\ell}{dN} = C (\Delta \epsilon_p \sqrt{\ell})^s \quad (2.6)$$

where ℓ is the crack length, N is the number of cycles, $\Delta \epsilon_p$ is the plastic strain range, and C and s are constants. By further assuming that the crack length at fracture is approximately constant, the plastic power-law relation analogous to Equation (2.5) was obtained from Equation (2.6).

Strain-Life Relationship. Following Equation (2.5), an empirical strain-life relationship proposed by Coffin (1954) and Manson (1965) can be written as:

$$N_f = \frac{1}{2} \left(\frac{\Delta \epsilon_{IE}}{2\epsilon_f} \right)^{\left(\frac{1}{c} \right)} \quad (2.7)$$

where

N_f = mean cycle to failure

$\Delta \epsilon_{IE}$ = inelastic strain range in one cycle of loading

ϵ_f = fatigue ductility coefficient = 0.325

c = fatigue ductility exponent = -0.5 ~ -0.7, it is assumed as -0.5 here in the comparison of Engelmaier's Equation.

Although Equation (2.7) is simple to use, it does not account for the effect of cyclic frequency and mean cyclic temperature. Engelmaier (1983) modified the Coffin-Manson relationship for near eutectic Sn-Pb solders to include an empirical description of the effect of cyclic frequency and mean temperature. The modified expression is:

$$N_f = \frac{1}{2} \left(\frac{\Delta \gamma}{2\epsilon_f} \right)^{\left(\frac{1}{c} \right)} \quad (2.8)$$

where

N_f = mean cycle to failure

$\Delta \gamma$ = total shear strain range in one cycle of loading

ϵ_f = fatigue ductility coefficient = 0.325

c = fatigue ductility exponent

$$= -0.442 - 6 \times 10^{-4} T_m + 1.74 \times 10^{-2} \ln(1 + f)$$

T_m = mean cyclic solder joint temperature °C

$$= \frac{1}{2} (T_{\max} + T_{\min})$$

T_{\max} = maximum cyclic temperature °C

T_{\min} = minimum cyclic temperature °C

f = cyclic frequency, $1 < f < 1000$ cycles/day

The equivalent strain is defined from the components of the strain tensor as:

$$\varepsilon = \sqrt{\frac{2}{3} \varepsilon_{ij} \varepsilon_{ij}} \quad (2.9)$$

where,

$$\varepsilon_{ij} = \int d\varepsilon_{ij} \quad (2.10)$$

is the total strain tensor which is the sum of elastic, plastic, and creep components, and $d\varepsilon_{ij}$ is the incremental strain tensor. The equivalent strain ε is then converted to the equivalent shear strain γ by the following relationship:

$$\gamma = \sqrt{3} \varepsilon \quad (2.11)$$

The total equivalent shear strain amplitude is the sum of the elastic, plastic and creep strain amplitudes obtained from the finite element analysis:

$$\gamma = \gamma_e + \gamma_p + \gamma_c \quad (2.12)$$

Energy-Partitioning Approach. Energy-partitioning approach was proposed by Dasgupta et al. (1992). The advantage of this method is that it includes both strain and stress information in life prediction, while the Coffin-Manson type strain-life relationships include the effect of strain information only. The solder joint response to cyclic thermal loading in this method is characterized by hysteresis loops on the stress/strain plane. The area of these hysteresis loops are representative of the creep energy dissipation density, plastic energy dissipation density, and elastic strain energy density, respectively, over one cycle. Obviously, the constitutive relation of the solder affect the shape of the stress-strain relationship.

Dasgupta et al. (1992) indicated that the power-law relationship between strain range and life also implies a power-law relationship between energy density dissipated per cycle and fatigue life. Thus:

$$\text{Energy} = U_e + W_p + W_c = U_0 N_{fe}^{b'} + W_{p0} N_{fp}^{c'} + W_{c0} N_{fc}^{d'} \quad (2.13)$$

where

$$U_e = U_0 N_{fe}^{b'} = \frac{1}{2} G \gamma_e^2,$$

$$W_p = W_{p0} N_{fp}^{c'} = \int \tau d\gamma_p$$

$$W_c = W_{c0} N_{fc}^{d'} = \int \tau d\gamma_c$$

where b' , c' , d' are the slopes and U_0 , W_{p0} , and W_{c0} are the intercepts of the plots of U_e , W_p , and W_c , respectively, versus cycles to failure on a log-log scale. The fatigue constants U_0 , W_{p0} , W_{c0} , b' , c' , and d' were derived in terms of the strain-life fatigue constants by Dasgupta et al. (1992) as follows:

$$b' = -0.18$$

$$c' = -0.6$$

$$d' = -1.16$$

$$U_0 = 100 \text{ (lb-in/cycle-in}^3\text{)} = 11.30\text{E6 (N-mm/cycle-mm}^3\text{)}$$

$$W_{p0} = 24,200 \text{ (lb-in/cycle-in}^3\text{)} = 27.35\text{E8 (N-mm/cycle-mm}^3\text{)}$$

$$W_{c0} = 9250 \text{ (lb-in/cycle-in}^3\text{)} = 10.45\text{E8 (N-mm/cycle-mm}^3\text{)}$$

Consequently, the fatigue damage per cycle due to elastic, plastic and creep energy dissipation can be written as:

$$D_e = \frac{1}{N_{fe}}, D_p = \frac{1}{N_{fp}}, D_c = \frac{1}{N_{fc}}, \quad (2.14)$$

respectively. The total damage D_T is given by:

$$D_T = D_e + D_p + D_c \quad (2.15)$$

The solder joint fatigue life, N_f , is given by:

$$N_f = \frac{1}{D_T} \quad (2.16)$$

Table 2.1 The values of coefficients in Equation (2.1)

Investigators	A	Q (KJ/mol)	p	n
Grivas (1974)	3.2×10^{12}	79.1	2.0	3.0
Mohamed and Langdon (1975)	1.5×10^{14}	84.1	2.3	3.0
Lam <i>et al.</i> (1979)	40.0	44.0	1.6	2.4

Table 2.2 The elastic and thermal expansion properties of the materials.

Material	Temperature (°C)	Young's Modulus GN/m ²	Poisson's Ratio	Coefficient of Thermal Expansion μm/m°C
Resistor (ceramic)	-55	255.1	0.30	6.0
	24	255.1	0.30	6.0
	125	255.1	0.30	6.0
Board (FR-4)	-55	11.1	0.30	15.0
	24	11.1	0.28	15.0
	125	11.1	0.30	15.0
Solder (Pb-Sn)	-55	51.8	0.40	25.0
	24	48.2	0.40	25.0
	125	43.7	0.40	25.0

patran2 Release 2.5 PDA Engineering

COMMAND

NAME

DISPLAY

ACTIVE

WINDOW

VIEW

SET/SHOW

PLOT

DISPLA

FINITE ELEMENT MESH (887 ELEMENTS)

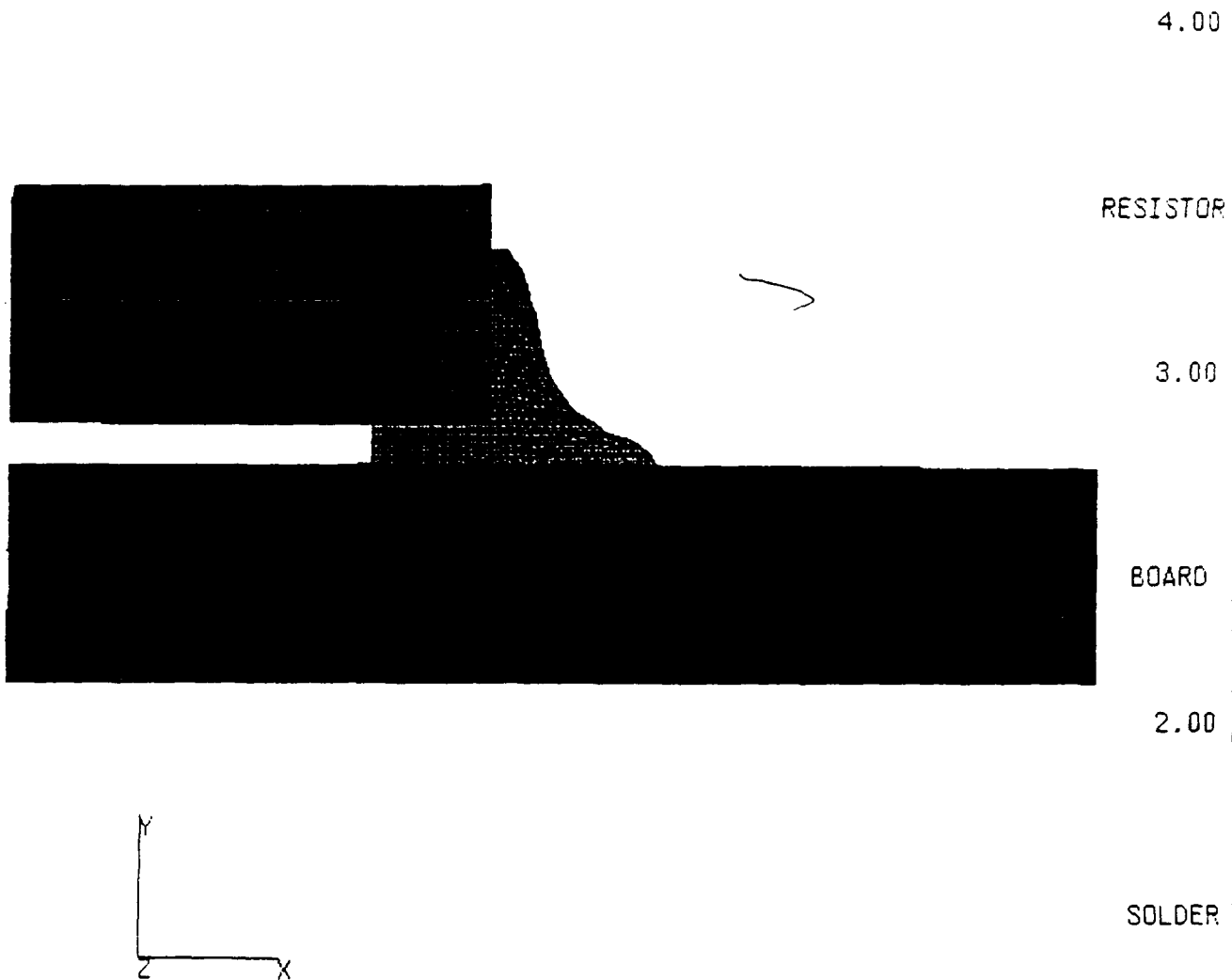


Figure 2.1 Two dimensional solid model of solder-resistor-board assembly

COLOR CODE BY PROPERTY ID

INPUT DIRECTIVE OR "END"

E

3. NUMERICAL RESULTS AND DISCUSSIONS

In most cases of our numerical calculations, Equation (2.1) is used with constants given by Lam *et al.* (1979) in Table 2.1. Unless otherwise stated, the thermal cycle is started at 125°C in each case. The whole model is assumed to have a uniform temperature, stress free condition at the starting temperature. A full cycle consisted of cool-down and heat-up between 125°C and -55°C using the same ramp and hold times during the cool-down and heat-up stages. A typical thermal loading history curve with 5 minutes ramp time and 10 minutes hold time is shown in Figure 3.1. The grain size of solder is chosen as 5.5×10^{-3} mm, unless otherwise specified.

3.1. A Two-dimensional Resistor-Joint-Board Assembly - A Parametric Study

In this case, a parametric study has been done for a two-dimensional finite element model of a typical solder joint described in Section 2.1.

Effect of Ramp Time. The calculated effect of ramp time on the maximum equivalent stress and strain is shown in Figures 3.2 through 3.4. Figure 3.2 shows the maximum von Mises stress history. The maximum stress increases as the ramp time decreases. For the cases when the ramp time is smaller than 2 minutes, the maximum stress reaches the yield stress and hardening takes place. Especially for the case of very fast ramp time, such as 10^{-5} sec ramp time, the stress continues to increase after the solder has yielded during the temperature ramp down. Also, a stress relaxation at the hold time is observed for all cases due to creep. The maximum equivalent total strain in Figure 3.3 shows that the total strain decreases with the increase of the ramp

time. The effect of ramp time on the maximum equivalent plastic strain and creep strain history is shown in Figures 3.4(a) and 3.4(b), respectively, for the same case. It is observed that the faster ramp time causes more plastic strain but less creep strain, while the slower ramp causes more creep strain but less plastic strain.

Effect of Hold Time. The effect of hold time on maximum equivalent stress and strain is also studied as shown in Figures 3.5(a) and 3.5(b), respectively. The results showed that there are no significant changes in the maximum stress and strain magnitudes due to the changes in hold time duration.

Figures 3.6 and 3.7 show the distribution of von Mises stress and creep strain, respectively, after 5 minutes ramp from 125°C to -55°C and after 10 minutes hold at -55°C. It is observed from Figure 3.6 that the stress is redistributed after 10 minutes hold, and its magnitude reduces due to creep relaxation. The effect of creep relaxation is also depicted in Figure 3.8, where the creep strain has increased after 10 minutes hold at -55°C. The maximum stress and creep strain are determined at the interface between the solder and the resistor.

Effect of Grain Size. The effect of grain size on the maximum equivalent stress and strain was also investigated. Although, the grain size changes are usually accompanied by the changes in material properties, here, due to the lack of sufficient material data, only grain size change was considered. It is observed in our study that the maximum von Mises stress and plastic strain increase when the grain size increases, while the maximum creep strain and total strain magnitudes decrease. Figure 3.8 shows the maximum equivalent total strain history curve. The effect of the grain size on number of cycles to failure is rather insignificant as summarized in Table 3.1.

Effect of Constitutive Models and Constants. The sensitivity of results to different constitutive equations and material constants given by different investigators were also investigated. The results are shown in Figure 3.9 for a cycle with 5 minutes ramp time and 10 minutes hold time. Although the values of partitioned strains (plastic and creep) vary, it was observed that there is no significant difference in the maximum equivalent total strain

magnitudes with different constitutive equations. The fatigue life predicted by different constitutive equations and constants are given in Table 3.2.

The sensitivity of results to different material constants given by different investigators were studied using the both failure criteria. The results obtained by using the basic 887-element mesh are summarized in Figures 3.10-3.15. Figures 3.10 and 3.11 are the maximum von Mises stress and the maximum total strain history curves for one cycle of loading with 2 minutes ramp and 10 minutes hold. These curves tend to repeat the same behavior for all other cycles, with a strain magnitude shift in each cycle equal to the residual strains shown at the end of the first cycle.

The equivalent strain magnitudes in Figure 3.11 were calculated from Equation (2.9). The equivalent strains can also be determined using the summation of the incremental equivalent strain values calculated at every time-step of the solution procedure as follows:

$$\epsilon = \int d\epsilon \quad (3.1)$$

where $d\epsilon$ is the value of the incremental effective strain evaluated from:

$$d\epsilon = \sqrt{\frac{2}{3} d\epsilon_{ij} d\epsilon_{ij}} \quad (3.2)$$

and $d\epsilon_{ij}$ is the incremental strain tensor. The ABAQUS computer program provides an option of calculating the effective strains either from Equation (2.9) or from Equation (3.1). Since in Equation (3.2), $d\epsilon$ is always positive, Equation (3.1) yields a continuously increasing effective strain values throughout a loading cycle. This is illustrated in Figure 3.12. Comparing Figures 3.11 and 3.12 shows that Equation (3.1) gives approximately twice as much creep strain than what is calculated from Equation (2.9). However, since Equation (2.9) reflects the strain relaxation properly, it may physically be more meaningful to use for determining the total strain range, $\Delta\epsilon$, in fatigue-life calculations. It is seen from the results of the strain-life

prediction, in spite of significant variations in creep properties given in Table 2.1, the resulting total maximum strains as well as the number of cycles to failure are rather insensitive to the variations in these properties. However, the stresses are more sensitive to the changes in creep properties.

Figures 3.13-3.15 are the hysteresis loops which represent the viscoplastic strain energy density. Equation (2.9) was used again for calculation of the equivalent strains. Figures 3.16-3.17 shows life prediction results from two failure criteria. The correspondence results of elastic, plastic and creep strain and energy as well as the fatigue life predicted by both methods are summarized in Table 3.4-3.5. These results indicate that the strain energy density is more sensitive to the changes in creep properties. It is observed that the energy-based and strain-based failure laws may give conflicting predictions of fatigue damage accumulation. The energy criterion gives more conservative life prediction, especially in the cases when stress and strain are calculated away from singularity point.

Effect of Young's Modulus. For the cycles of 5 minutes ramp, 10 minutes hold, and 10^{-5} second ramp, 10 minutes hold, we have also investigated the change of the maximum strains and stresses of the solder joint with changing Young's moduli given by Equation (2.3) and by using a magnitude ten times smaller. Figures 3.18 through 3.21 show the history curves of maximum von Mises stress, maximum equivalent creep strain, maximum equivalent plastic strain, and maximum equivalent total strain, respectively, for both cases. It is found from these figures that higher Young's modulus results with higher maximum von Mises stress and higher maximum equivalent plastic strain, but lower maximum equivalent creep strain. The effect of Young's modulus on the maximum plastic and creep strain magnitude is pronounced in the case of faster ramps. There is, however, only an insignificant change of the total strain due to the change of the Young's modulus.

Effect of Initial Temperature. The effect of initial temperature (stress free) has also been investigated. Maximum stress and strain history curves of three thermal cycles with different initial temperatures are shown in Figures 3.22(a) and 3.22(b), respectively. Although there is a phase shift in the maximum stress response, there are no significant differences for the

maximum cyclic stress as well as the total strain. For the cycle started at -55°C , the stress increases at the very beginning and decreases throughout the rest of the ramp. This indicates that the effect of the solder creep is more significant than the temperature increases. At the high temperature hold, the stress is very small, but it does not reach zero. During the temperature ramp down, the stress increases continuously, and some stress relaxation is observed at the low temperature hold.

Three-Dimensional Effects. To assess the accuracy of the two-dimensional (2D) modeling assumptions, a three-dimensional (3D) finite element model is generated, as shown in Figure 3.23(a). Figure 3.23(b) shows the comparison of current plane stress model with plane strain, generalized plane strain and 3D models. It is observed in this case that the plane stress results in creep strain are closer to the 3D model than those of plane strain and generalized plane strain models.

Effect of Mesh Refinement. Several cases of mesh refinement have been studied and compared. It is found in Figures 3.24(a) and 3.24(b) that there are two singularity points at the sharp corner of the solder-resistor interface where the maximum total strain and the maximum von Mises stress increase as the number of element increases. Figures 3.25(a) through 3.25(d) show von Mises stress and equivalent creep strain distribution of two mesh refinements (the mesh with 232 elements, and the mesh with 1701 elements), respectively. It is found that the results of the denser mesh are in close agreement with the one of coarser mesh after a certain distance away from the singularity point. In predicting the life cycle, we propose the choice of a characteristic radius R , which is sufficiently far from the singularity point but close enough to represent the maximum strain area. An arc with its center at the singularity point and its radius equal to R is drawn as shown in Figure 3.26. The average total strain on the arc is calculated, and the total effective shear strain range is obtained using Equations (2.7) - (2.10). With this procedure, the results are less sensitive to mesh refinements.

To further study this, the same joint have been analyzed by increasing the mesh density to 887 and 1701 elements. The maximum total strain as well as the elastic, plastic and creep energy density on the arc are also calculated,

these are then converted to fatigue life to failure using both failure criteria. As it is shown in Figure 3.27-3.28, the results on the arc are rather insensitive to the mesh refinement for both life prediction criteria. It is also interesting to observe that the strain energy partitioning criteria is less sensitive to the mesh refinement even at the singularity point.

Fatigue Life Prediction. The calculated total shear strain range and energy density are introduced to the equation (2.8) and equation (2.16), respectively, to estimate the number of cycles to failure. Based on equation (2.8), it is observed that the number of cycles to failure decreases when the hold time increases as shown in Figure 3.29. This is mainly because the reduction in frequency decreases the number of cycles to failure. It is interesting to observe that the fatigue life is very sensitive to the hold duration up to 5 minutes, but much less sensitive at longer duration. A few minutes of hold time reduce the number of cycles to failure by almost 70%. The effect of the ramp time on the fatigue life of solder is governed by two factors, the total shear strain range as well as the frequency. The increase of the ramp time lowers the frequency of cycles which in turn tends to reduce the number of cycles to failure due to grain boundary cavitation, grain boundary sliding, and environmental effect (which are time dependent). In the mean time, the increase of the ramp time reduces the shear strain range leading to the increase of the number of cycles to failure. The combination of these two factors determines the number of cycles to failure, as shown in Figure 3.29(a). Figure 3.29(b) shows the number of cycles to failure versus holding time using the Coffin-Manson Equation (2.7). It is observed that the fatigue life predicted by Equation (2.7) is considerably lower than the one predicted by Equation (2.8). The fatigue life predicted using energy criterion gives the results quite different from those predicted by Equation (2.8) as we have discussed earlier. The energy criterion is more sensitive to the changes in creep properties but less sensitive in mesh refinement. Also, as we will mention later in section 3.3, it results in the number of life to failure very close to the one of the experiment test.

3.2. A Three-dimensional Assembly of Three Joints

A finite element model of a three-joints structure is shown in Figure 3.30. The geometry of this three-joints structure was obtained from RVSI laser system. In Section 3.3 of Part 2, we describe the detailed procedure of generating 3D finite element mesh from RVSI data. Here we show some of the numerical results of creep-plastic analysis of the solder joints under a thermal cycling. Figures 3.31-3.34 show the distribution of von Mises stress and creep strain, respectively, after 5 minutes ramp from 125°C to -55°C and after 10 minutes hold at -55°C. As it was discussed in Section 3.1, the stress is redistributed after 10 minutes hold, and its magnitude reduces due to creep relaxation. It is also found that the highest von Mises stress of the solder joints are located at the interface of the solder and the transistor, while the highest creep strain are at the interface of the solder and solder pad. Figures 3.35-3.36 show the stress and creep history curves for the same model. Figure 3.37 is the hysteresis loops which represent the creep strain energy density. The elastic and plastic energy density are zero in this case. The fatigue life of the solder joints is calculated using both failure criteria. The corresponding results of elastic, plastic and creep strain and energy as well as the fatigue life predicted by both methods are summarized in Table 3.6. As may be observed, both methods yield close results in this case.

In this three-dimensional case, the maximum strains occurred at solder-pad interfaces, while the maximum stresses occurred at solder-capacitor interfaces.

3.3 A Two-dimensional Resistor-Joint-Board Assembly -- Comparison with Experiments

A program for establishing of solder joint life prediction methodologies and experimental data of various surface mount components have been recently initiated by the Jet Propulsion Laboratory (Wen and Kovak, 1993). The results of an initial test case will be discussed here.

An assembly consisting of solder joint, resistor, solder pad, PC board and aluminum plate has been tested under a thermal-cycle loading at Motorola. The temperature cycling profile is shown in Figure 3.38, and the material properties of each component is shown in Table 3.3. It is observed from the test that the solder joint failed in about 200 cycles. A finite element model was generated based on the information given, and is shown in Figure 3.39. Notice that there is a small void in the solder joint in adjacent of the solder pad. Figures 3.40-3.41 are the maximum von Mises stress and maximum creep strain history curves, respectively. Figure 3.42 is the hysteresis loops which represents the creep energy dissipation density. The fatigue life of the solder joint are predicted using both failure criteria based on these curves, the results are shown in Figure 3.43. The corresponding results of elastic, plastic and creep strain and energy as well as the fatigue life predicted by both methods are summarized in Table 3.7. It is seen from the figure that the fatigue life predicted using energy criterion results with the number of life to failure prediction very close to the one of the experiment. The strain criterion yielded much shorter fatigue life. The same joint, in the absence of void was also analyzed as shown in Figure 3.44. It is found from Figure 3.42 that the fatigue life predicted for the joint without void is very close to the one which has a void. This is because the void in this case is away from the highest strain and stress regions. Therefore, it is concluded that in this specific case, the void in the solder joint has insignificant effect on the fatigue life to failure. In the mean while, we have also tried different mesh refinement as shown in Figure 3.45, and found that there is no significant variation in stress and strain distribution due to the mesh refinement, especially at the maximum stress and strain location. Therefore, the location where the maximum stress and strain occurred were chosen for the life prediction.

In this case, the corner of solder, pad and resistor interface shown in Figure 3.39 was the location of maximum strain and stress magnitudes.

Table 3.1 The effect of grain size on the number of cycles to failure (5 min ramp, 10 min hold)

Grain size (mm)	Shear Strain Range	Number of Cycles to Failure
2.2	0.0276	1478
5.5	0.0267	1615
18.4	0.0259	1736

Table 3.2 The comparison of the results using different constitutive laws (5 min ramp, 10 min hold)

Constitutive Law	Shear Strain Range	Number of Cycles to Failure
Lam <i>et al.</i> (1979)	0.0267	1615
Grivas (1974)	0.0291	1293
Mohamed & Langdon (1975)	0.0270	1563
Pan (1991)	0.0276	1478

Table 3.3 Elastic materials properties at room temperature (24°C)

Material	Young's Modulus GN/m ²	Poisson's Ratio	Coefficient of Thermal Expansion μm/m°C
Resistor (ceramic)	255.1	0.30	6.0
PC Board (FR-4)	11.1	0.28	15.0
Pad (copper)	126.0	0.37	13.0
Aluminum plate	63.7	0.36	23.5
Solder (Pb-Sn)	48.2	0.40	25.0

Table 3.4(a) Elastic, plastic, and creep strains, and the number of cycles to failure at the singularity point (887-element mesh)

Investigators	γ_e	γ_p	γ_c	N_f
Lam <i>et al.</i> (1979)	6.50E-4	1.31E-3	2.39E-2	1880
Grivas (1974)	7.69E-4	1.82E-3	2.46E-2	1659
Mohamed and Langdon (1975)	1.31E-3	4.66E-3	2.22E-2	1513

Table 3.4(b) Strain energy, plastic energy dissipation, and creep energy dissipation values, and the number of cycles to failure at singularity point (887-element mesh)

Investigators	U_e	W_p	W_c	N_f
Lam <i>et al.</i> (1979)	0.0	3.60E-2	3.50E-2	646
Grivas (1974)	0.0	5.18E-5	4.25E-2	547
Mohamed and Langdon (1975)	0.0	1.39E-1	2.64E-2	819

Table 3.5(a) Elastic, plastic, and creep strains, and the number of cycles to failure at $R = 0.03$ mm (887-element mesh)

Investigators	γ_e	γ_p	γ_c	N_f
Lam <i>et al.</i> (1979)	4.35E-4	0.0E+0	12.04E-3	12090
Grivas (1974)	7.22E-4	4.43E-5	11.88E-3	11846
Mohamed and Langdon (1975)	1.27E-3	1.09E-3	10.46E-3	11379

Table 3.5(b) Strain energy, plastic energy dissipation, and creep energy dissipation values, and the number of cycles to failure at $R = 0.03$ mm (887 element mesh)

Investigators	U_e	W_p	W_c	N_f
Lam <i>et al.</i> (1979)	0.0	0.0E+0	2.29E-2	933
Grivas (1974)	0.0	1.19E-3	2.88E-2	765
Mohamed and Langdon (1975)	0.0	3.21E-2	2.10E-2	1000

Table 3.6(a) Elastic, plastic, and creep strains, and the number of cycles to failure at the maximum strain point (three-joint model)

γ_e	γ_p	γ_c	N_f
0.757E-4	0.0	0.0611	198

Table 3.6(b) Strain energy, plastic energy dissipation, and creep energy dissipation values, and the number of cycles to failure at the maximum strain and stress point (three -joint model)

U_e	W_p	W_c	N_f
0.0	0.0	0.129	209

Table 3.7(a) Elastic, plastic, and creep strains, and the number of cycles to failure at the maximum strain point (JPL model)

Cases	γ_e	γ_p	γ_c	N_f
Perfect joint	0.977E-6	0.0	0.1136	32
Joint with void	0.736E-7	0.0	0.1140	32

Table 3.7(b) Strain energy, plastic energy dissipation, and creep energy dissipation values, and the number of cycles to failure at the maximum strain and stress point (JPL model)

Cases	U_e	W_p	W_c	N_f
Perfect joint	0.0	0.0	0.137	199
Joint with void	0.0	0.0	0.134	203

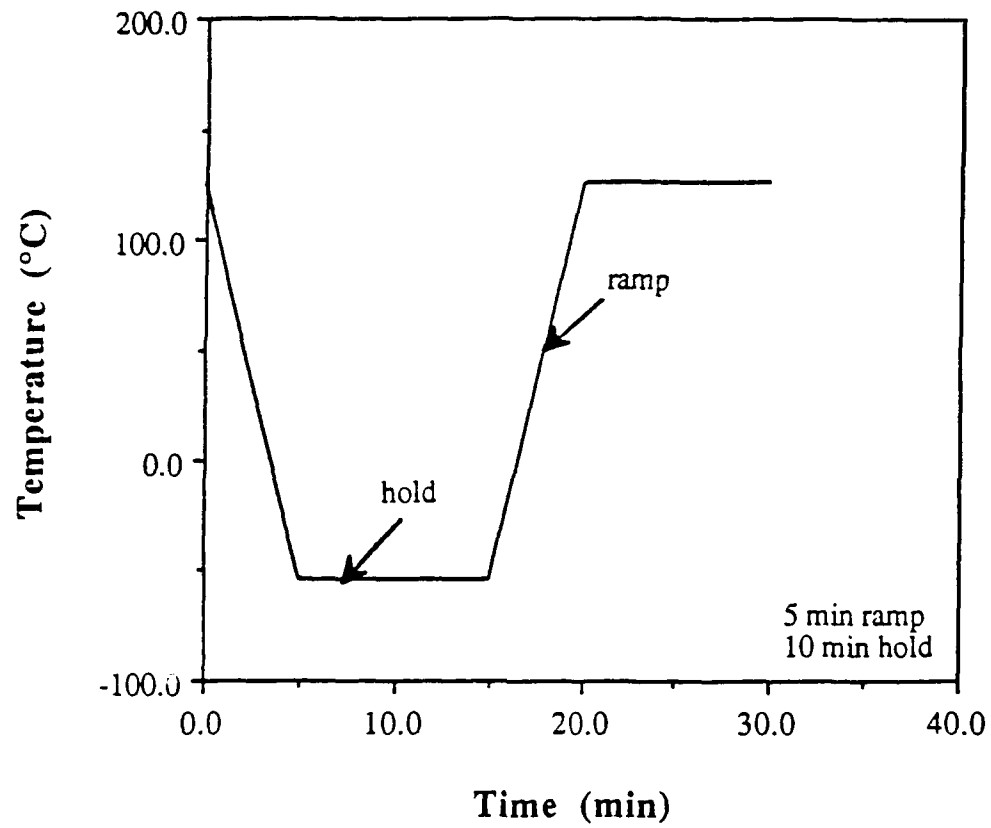


Figure 3.1 A typical temperature loading used for thermal cycling

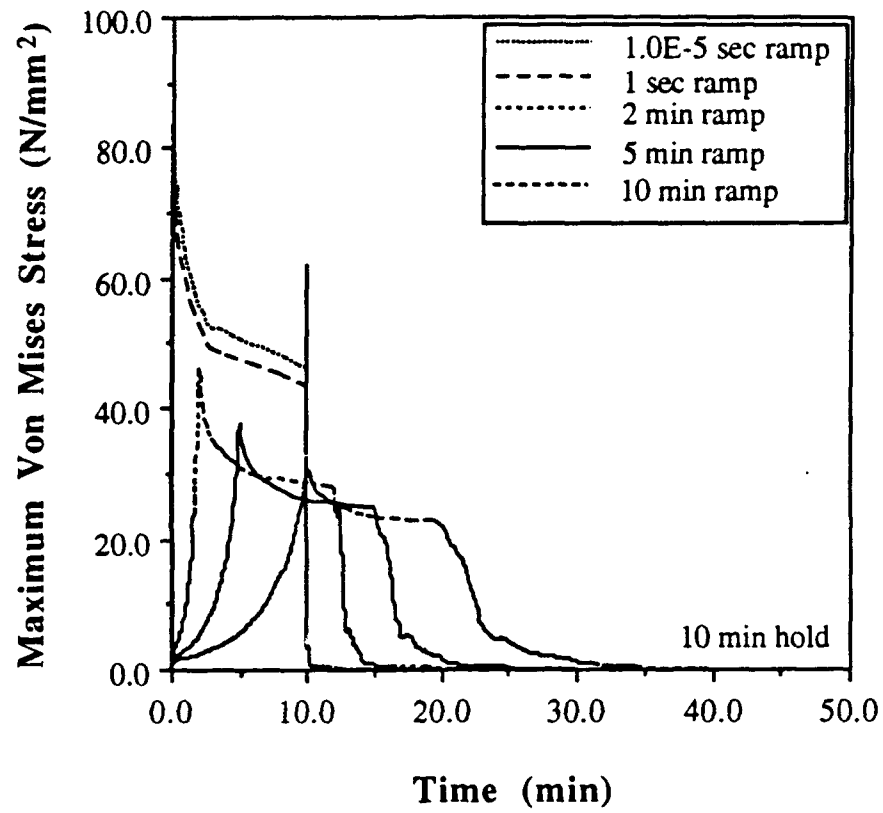


Figure 3.2 Maximum von Mises stress for different ramp times

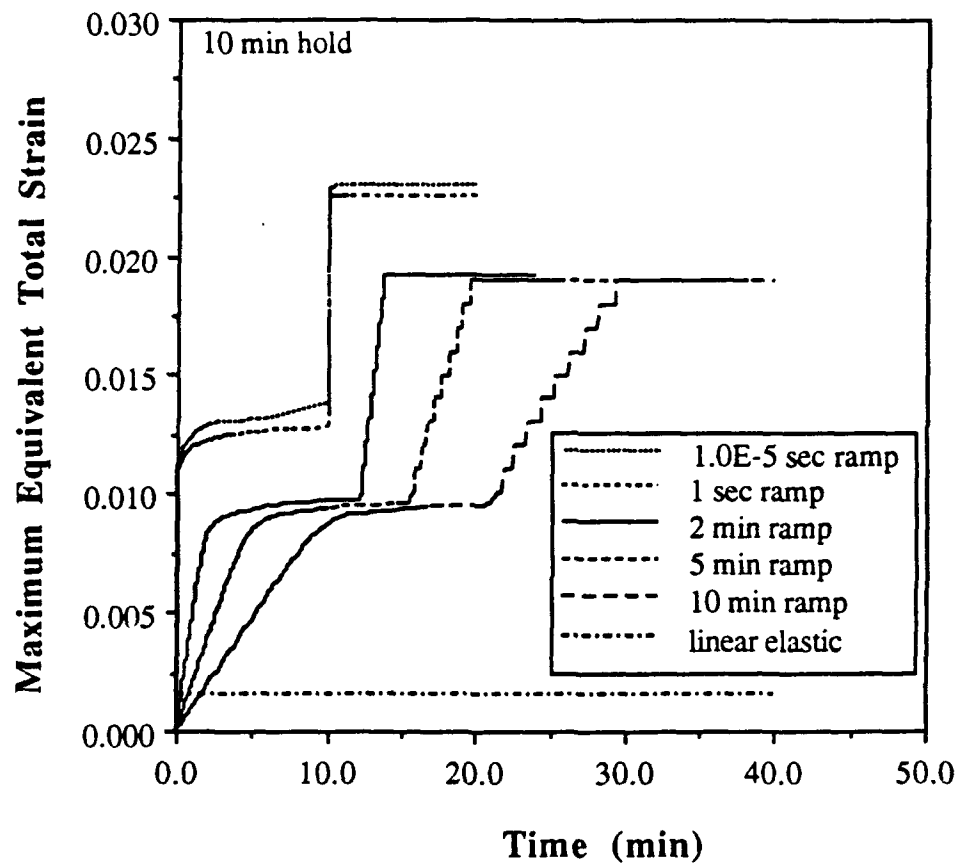


Figure 3.3 Maximum equivalent total strain for different ramp times

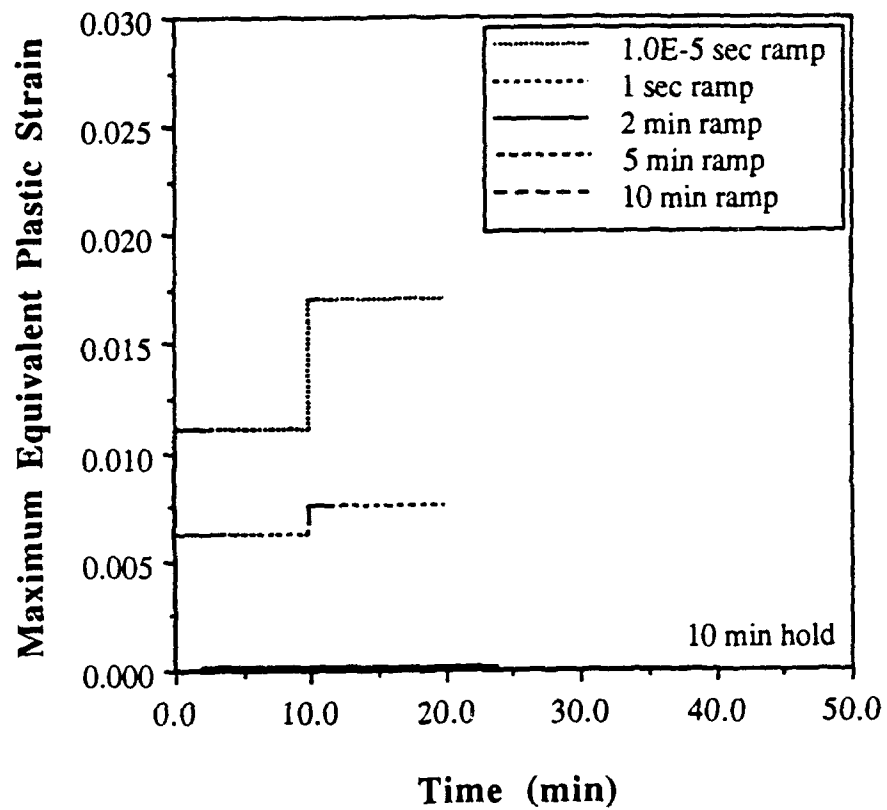


Figure 3.4(a) Maximum equivalent plastic strain for different ramp times

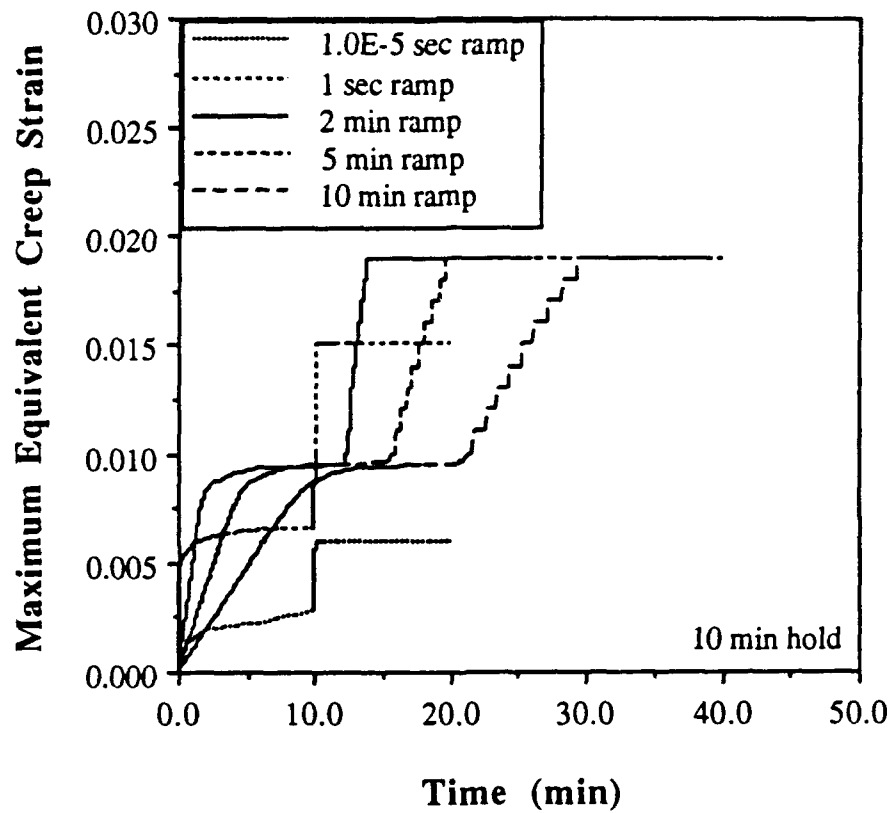


Figure 3.4(b) Maximum equivalent creep strain for different ramp times

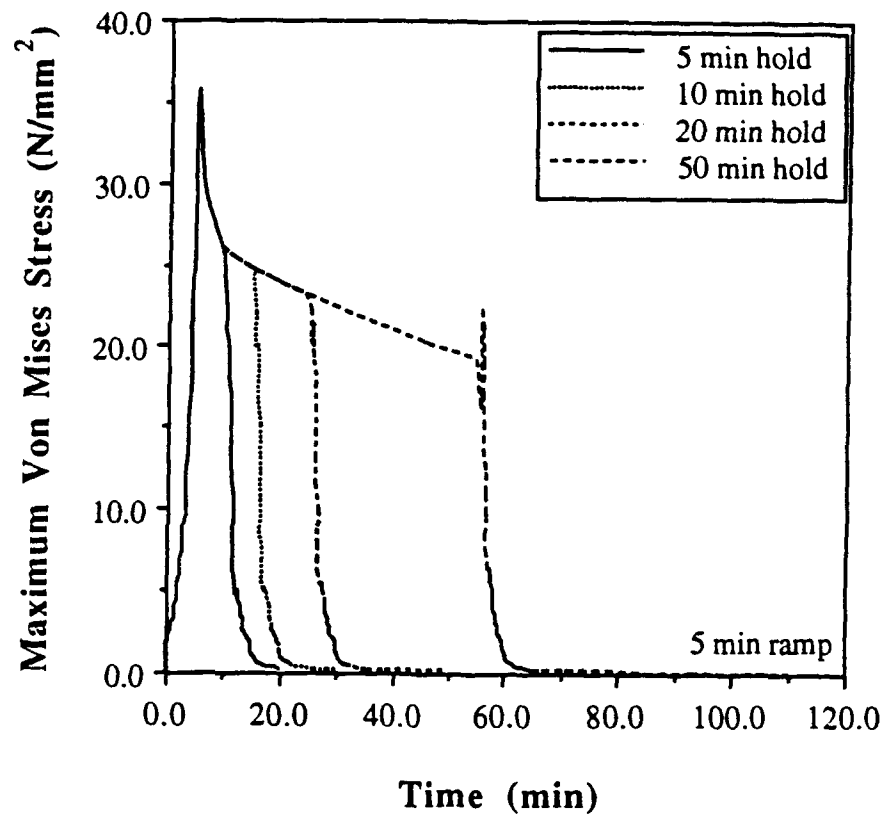


Figure 3.5(a) Maximum von Mises stress for different hold times

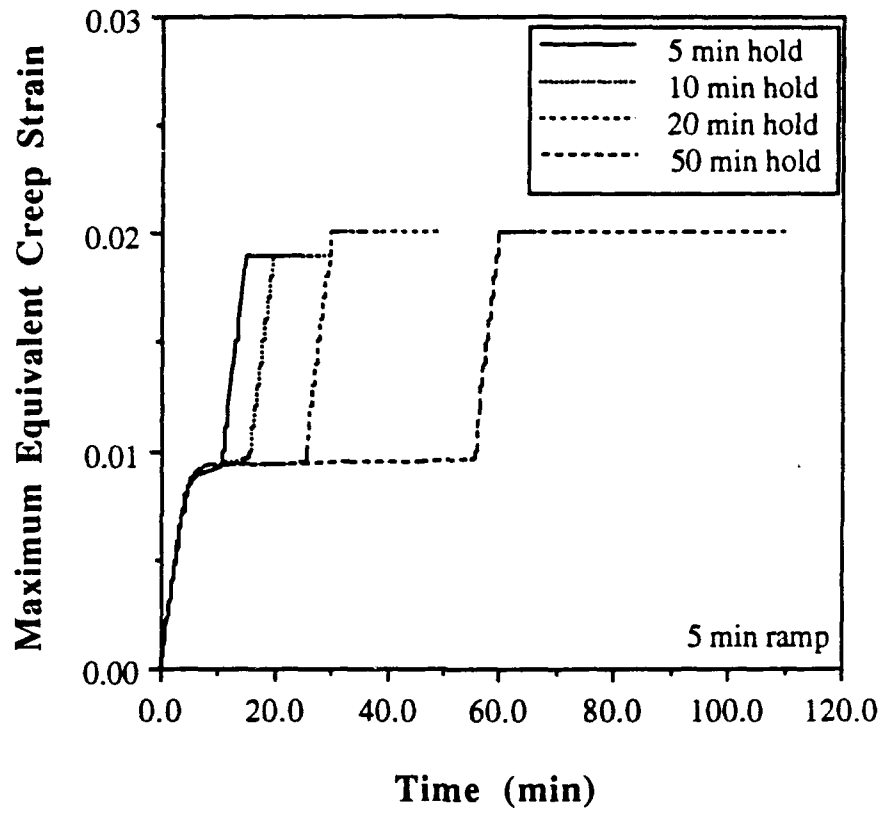


Figure 3.5(b) Maximum equivalent creep strain for different hold times

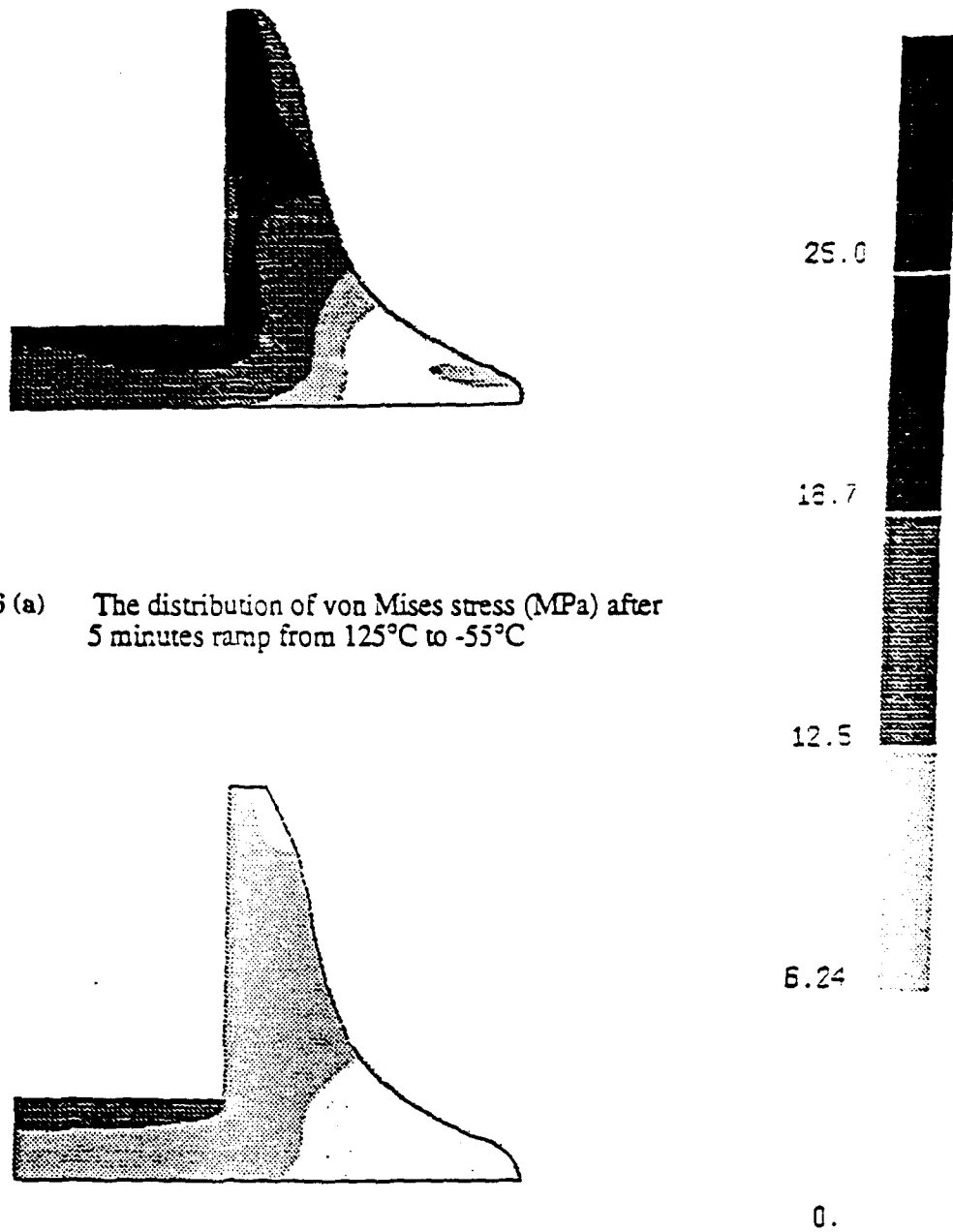


Figure 3.6 (a) The distribution of von Mises stress (MPa) after 5 minutes ramp from 125°C to -55°C

Figure 3.6(b) The distribution of von Mises stress (MPa) after 10 minutes hold at -55°C

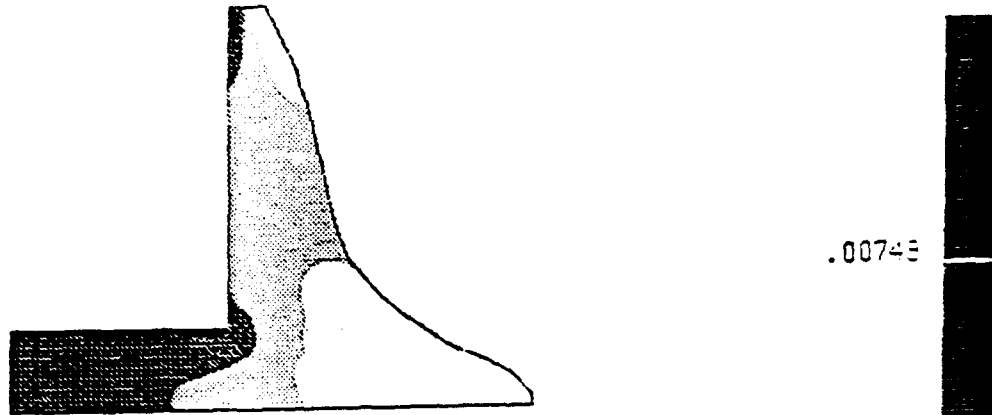


Figure 3.7(a) The distribution of equivalent creep strain after 5 minutes ramp from 125°C to -55°C

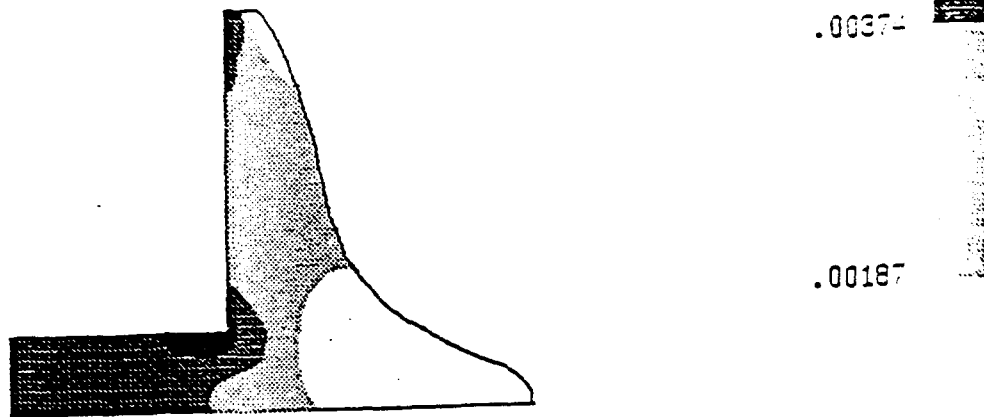


Figure 3.7(b) The distribution of equivalent creep strain after 10 minutes hold at -55°C

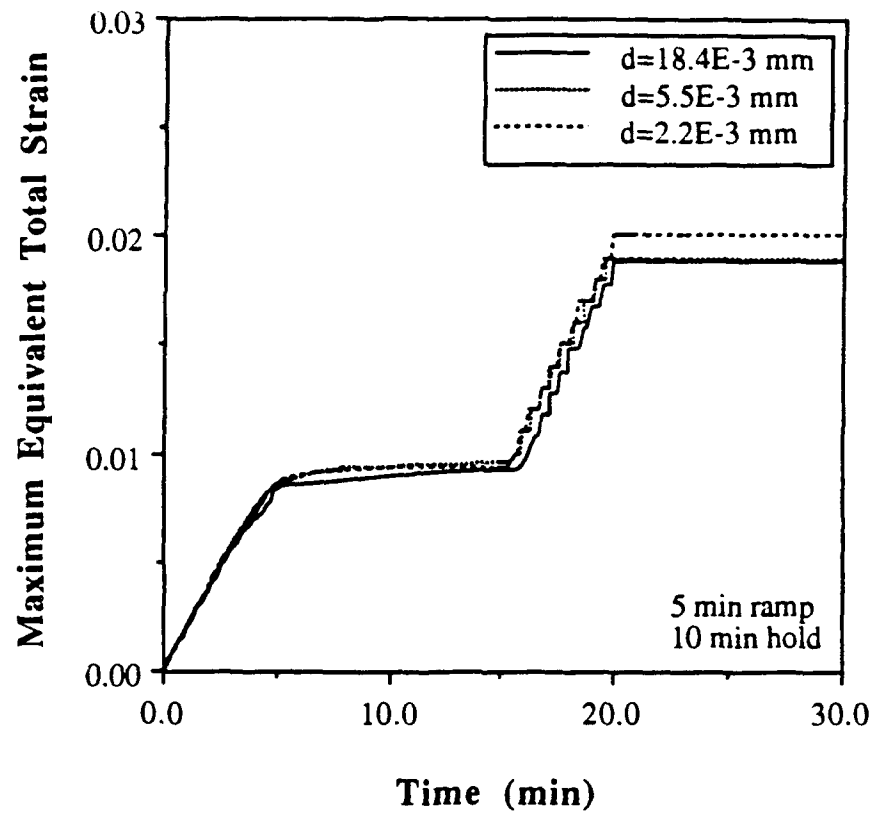


Figure 3.8 Maximum equivalent total strain versus time for different grain sizes

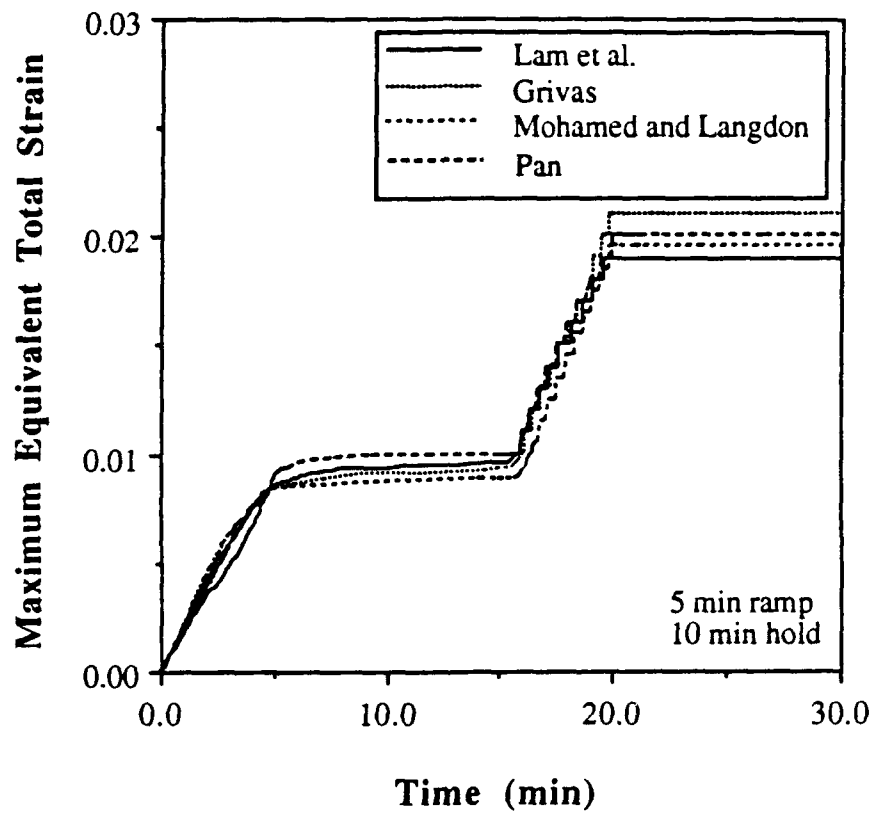


Figure 3.9 Maximum equivalent total strain versus time for different constitutive equations

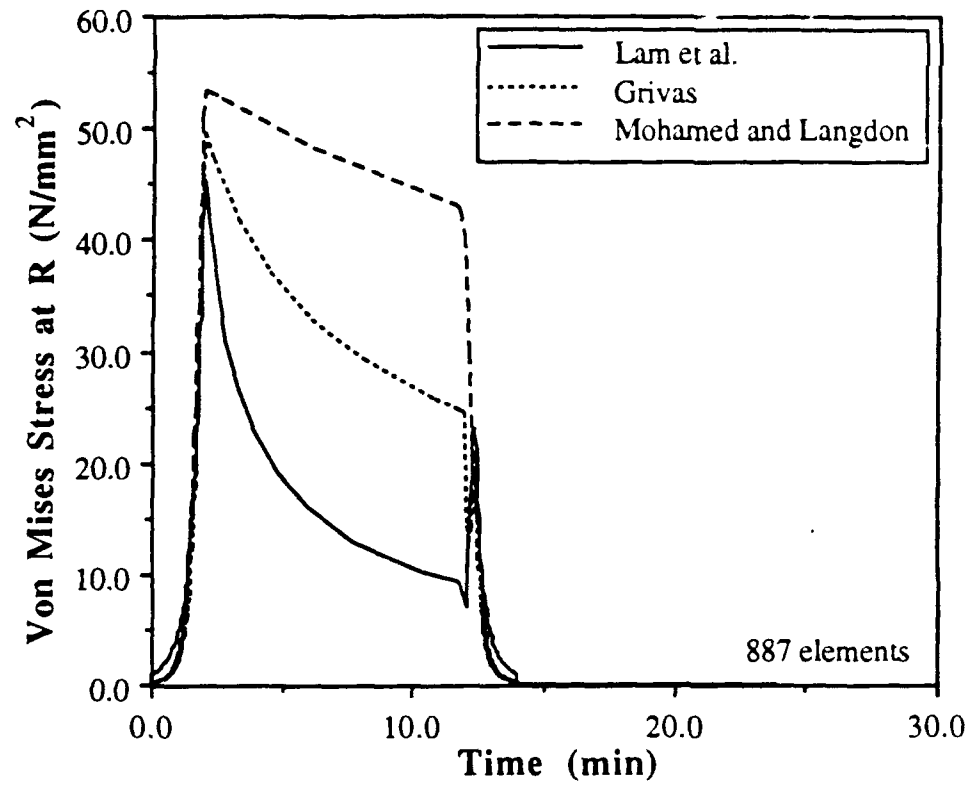


Figure 3.10 Maximum von Mises stresses for different material constants

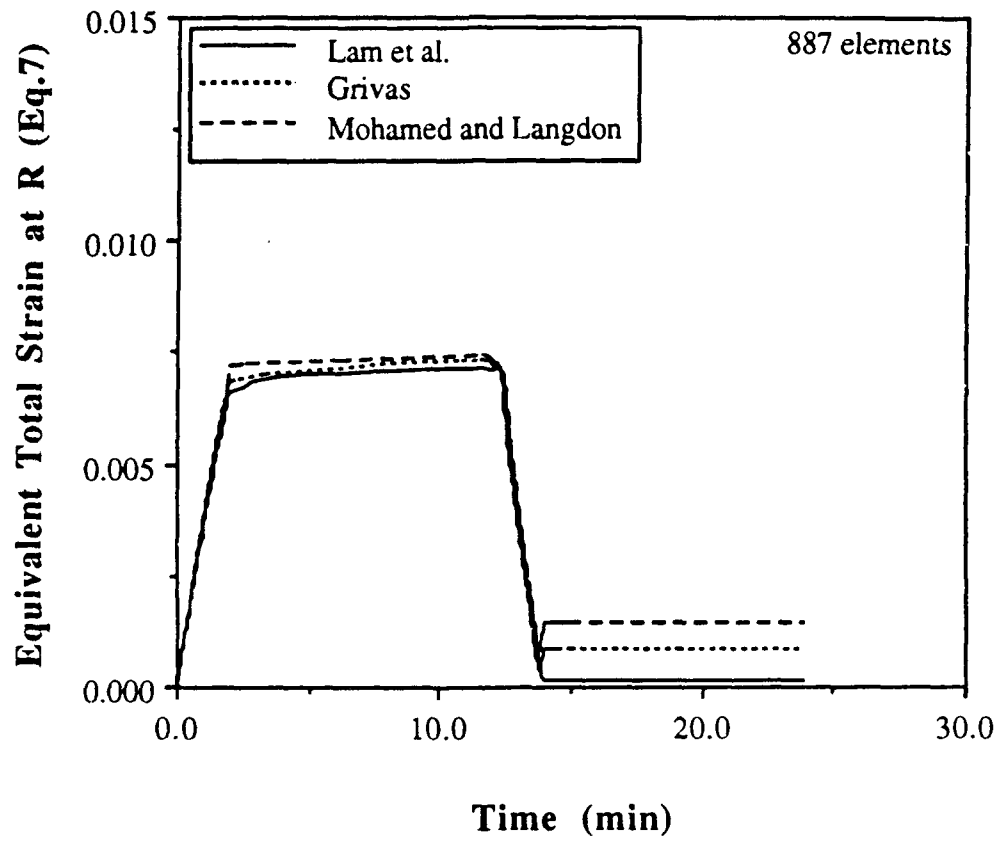


Figure 3.11 Maximum equivalent total strain for different material constants from Equation (2.9)

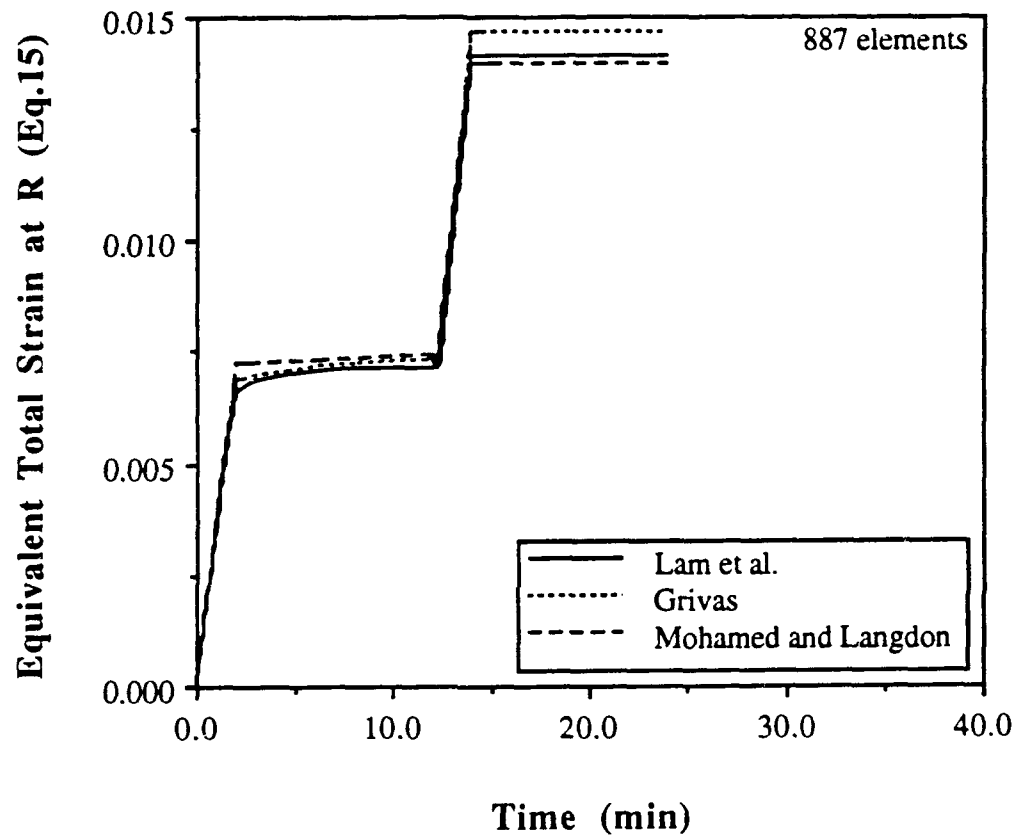


Figure 3.12 Maximum equivalent total strains for different material constants from Equation (3.2)

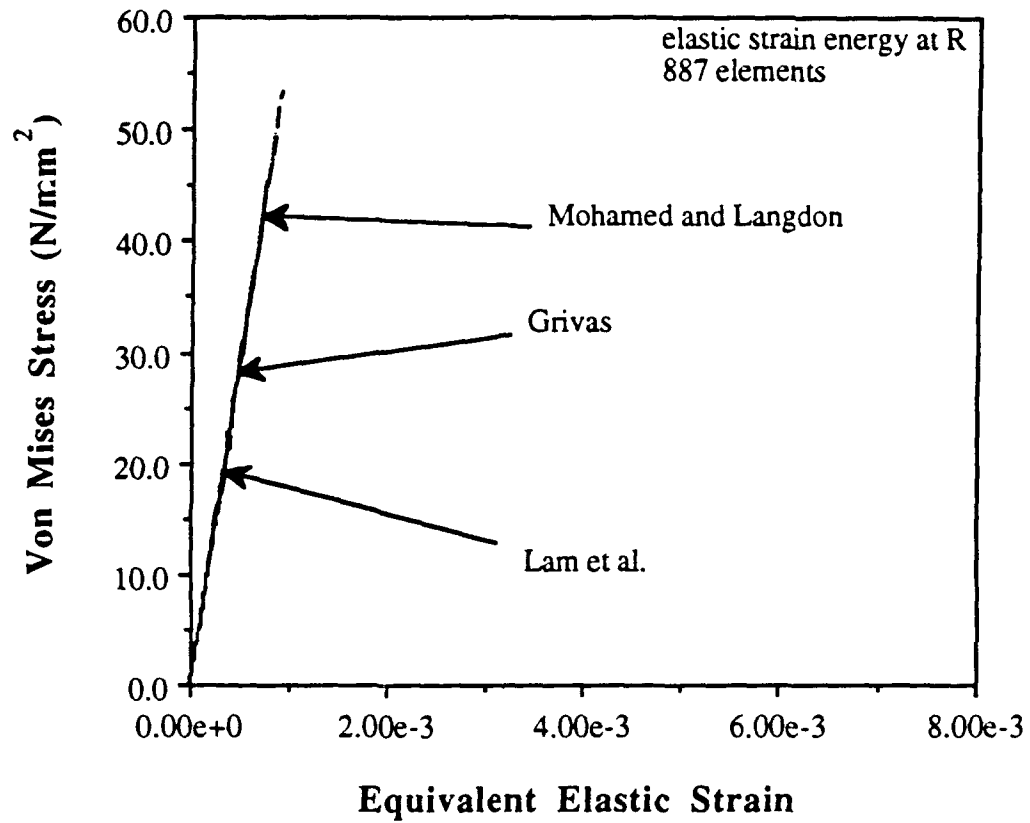


Figure 3.13 Elastic strain energy density at R

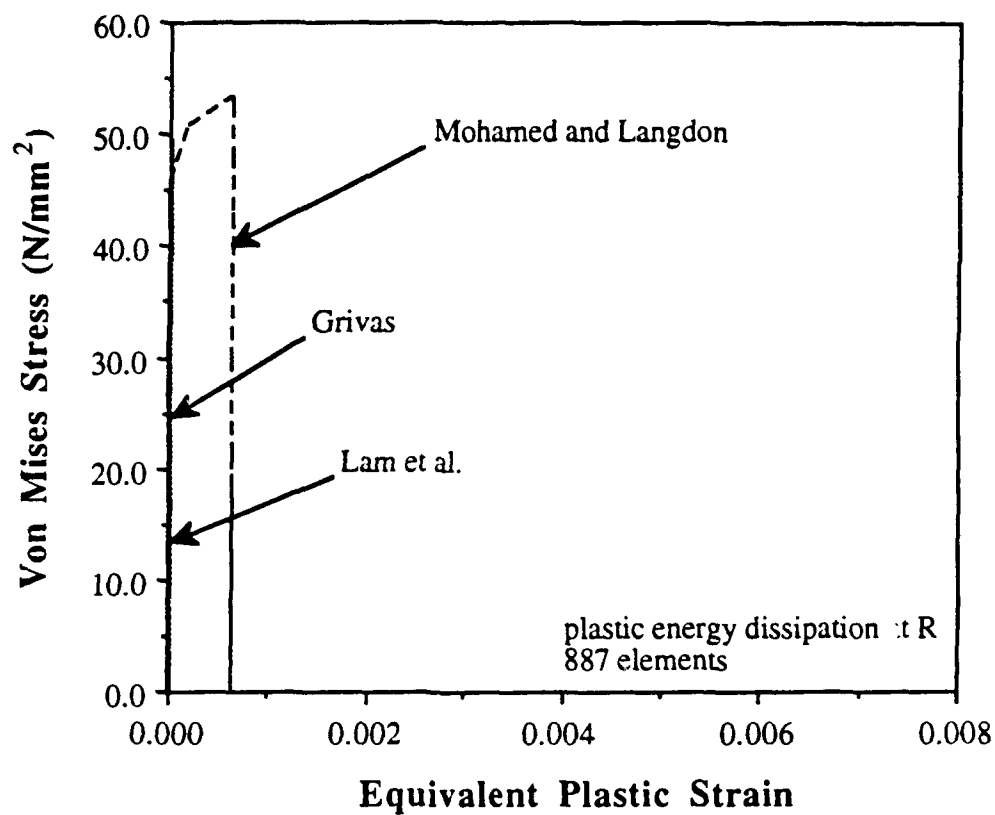


Figure 3.14 Plastic energy dissipation density at R

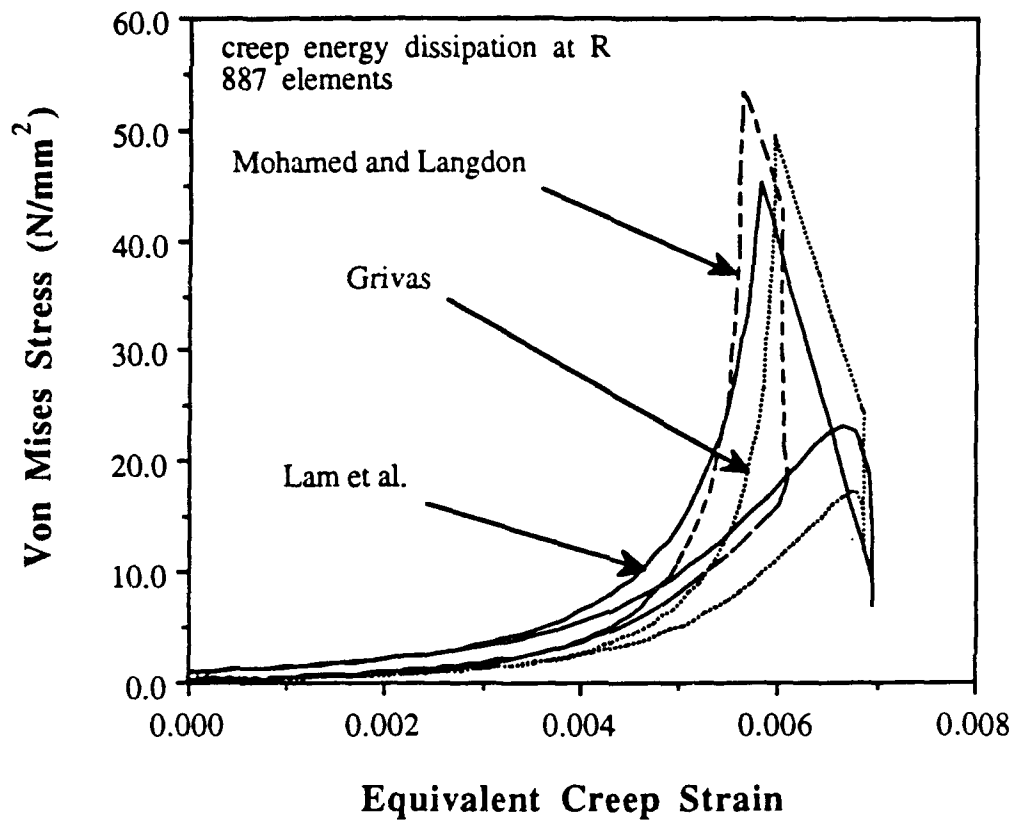


Figure 3.15 Creep energy dissipation density at R

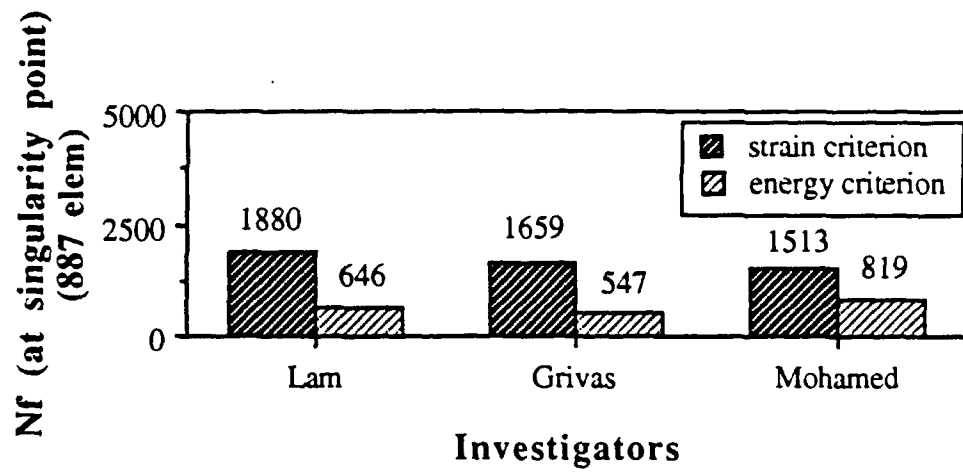


Figure 3.16 Number of cycles to failure at the singularity point using both criteria

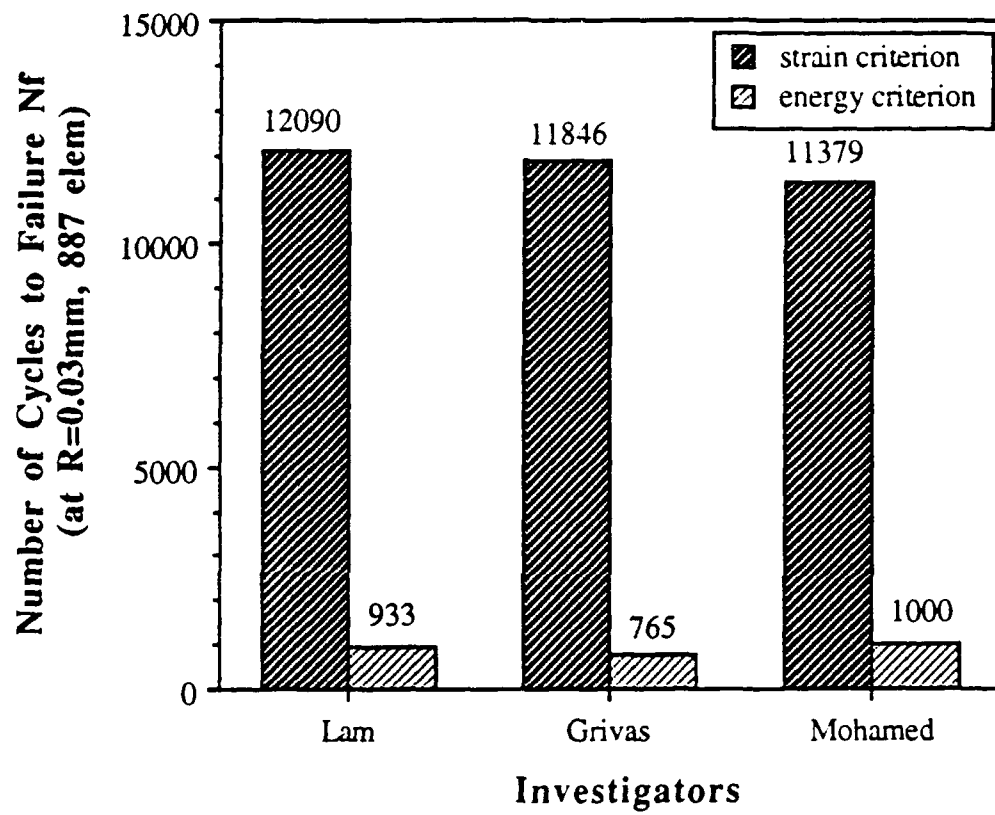


Figure 3.17 Number of cycles to failure at $R=0.03$ mm using both criteria

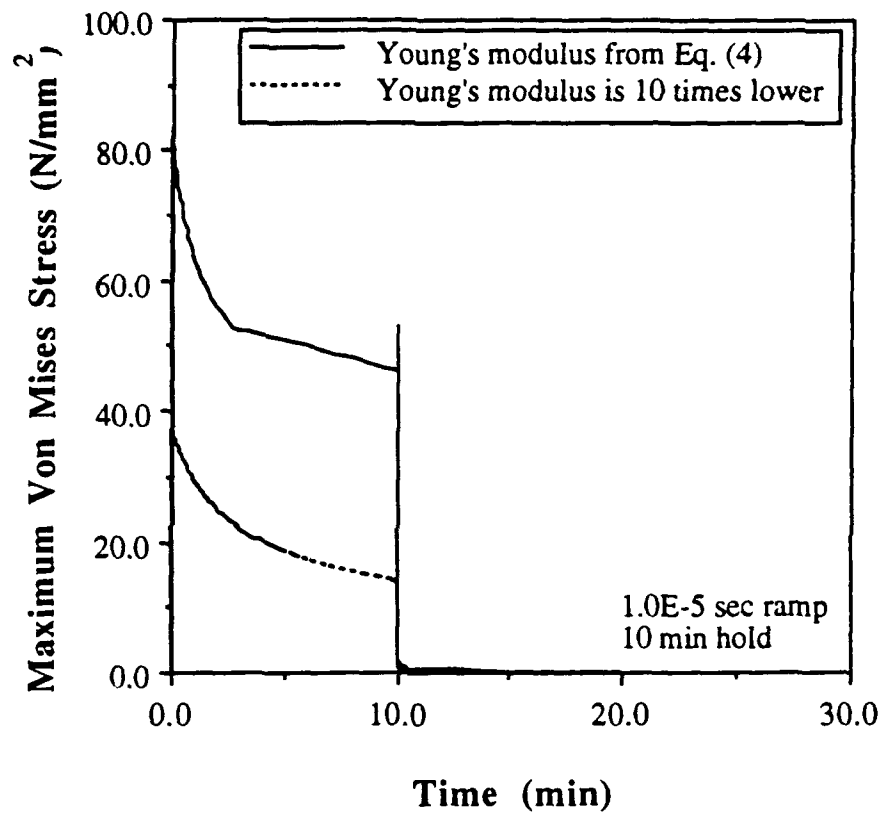


Figure 3.18(a) Maximum von Mises stress versus time of the cycle with 1.0E-5 sec ramp and 10 minutes hold for different Young's moduli

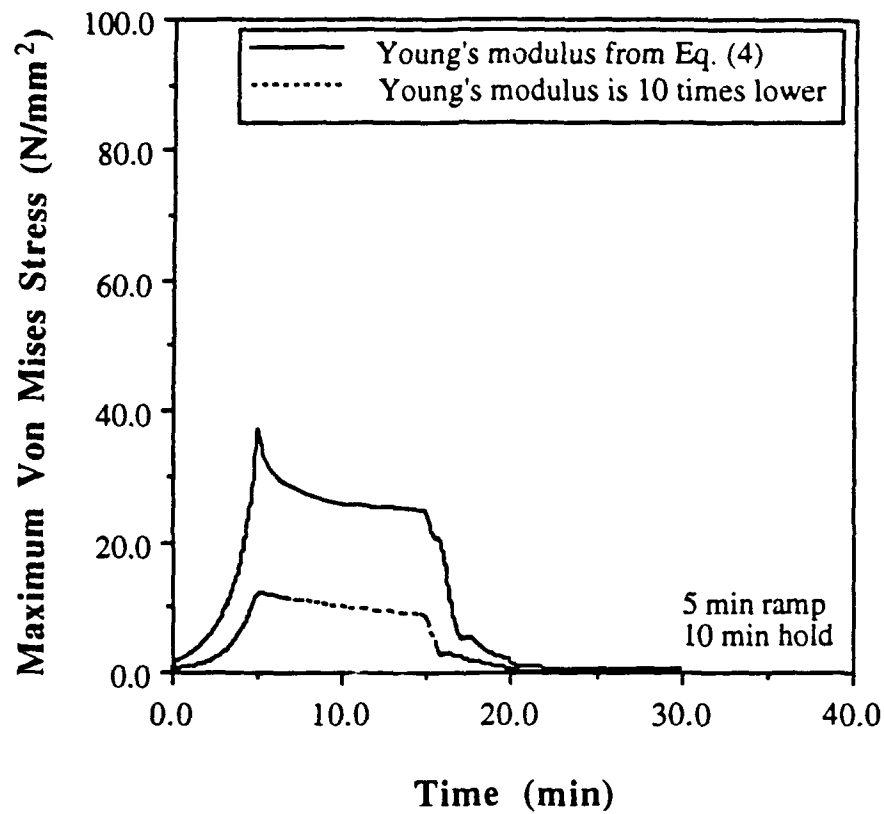


Figure 3.18(b) Maximum von Mises stress versus time of the cycle with 5 minutes ramp and 10 minutes hold for different Young's moduli

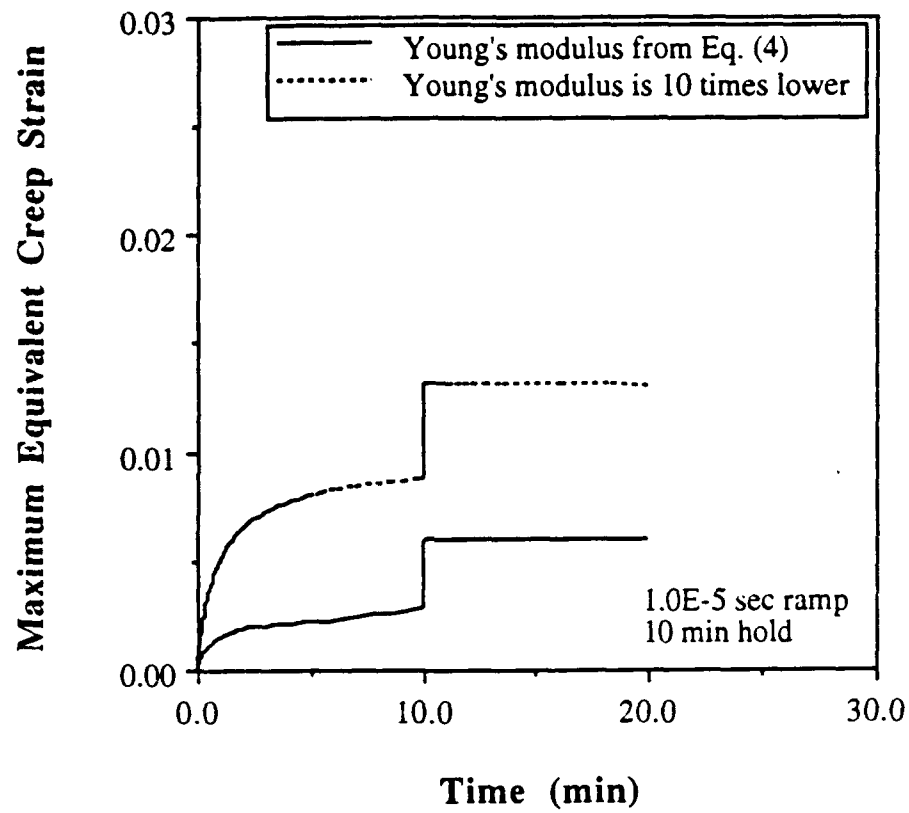


Figure 3.19(a) Maximum equivalent creep strain versus time of the cycle with $1.0\text{E-}5$ sec ramp and 10 minutes hold for different Young's moduli

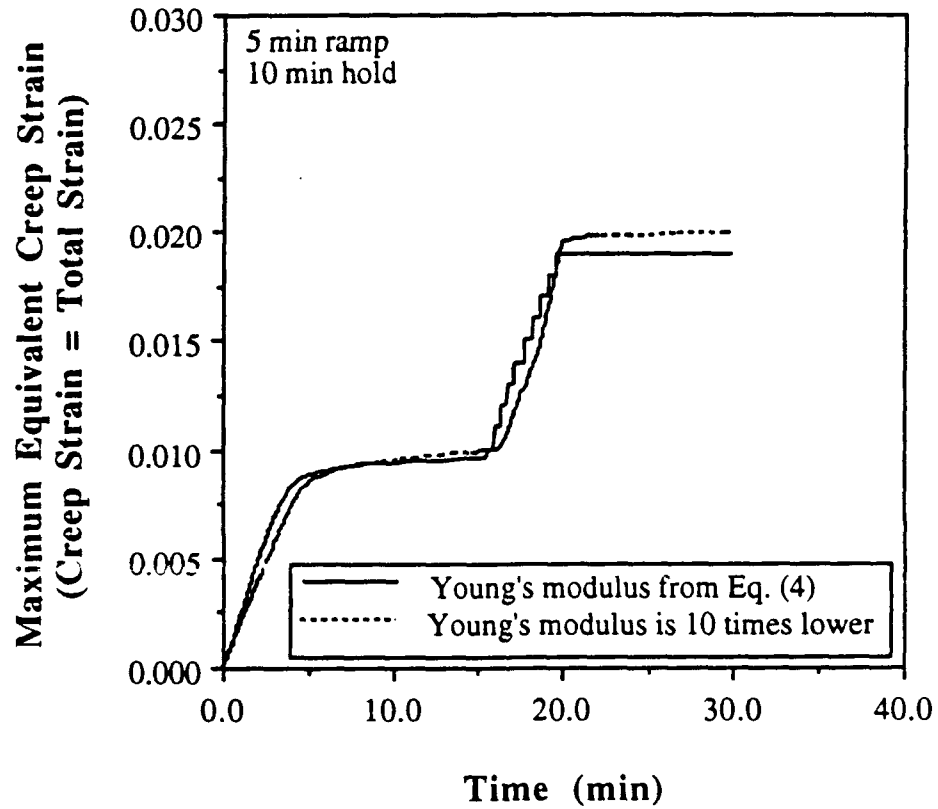


Figure 3.19(b) Maximum equivalent creep strain versus time of the cycle with 5 minutes ramp and 10 minutes hold for different Young's moduli

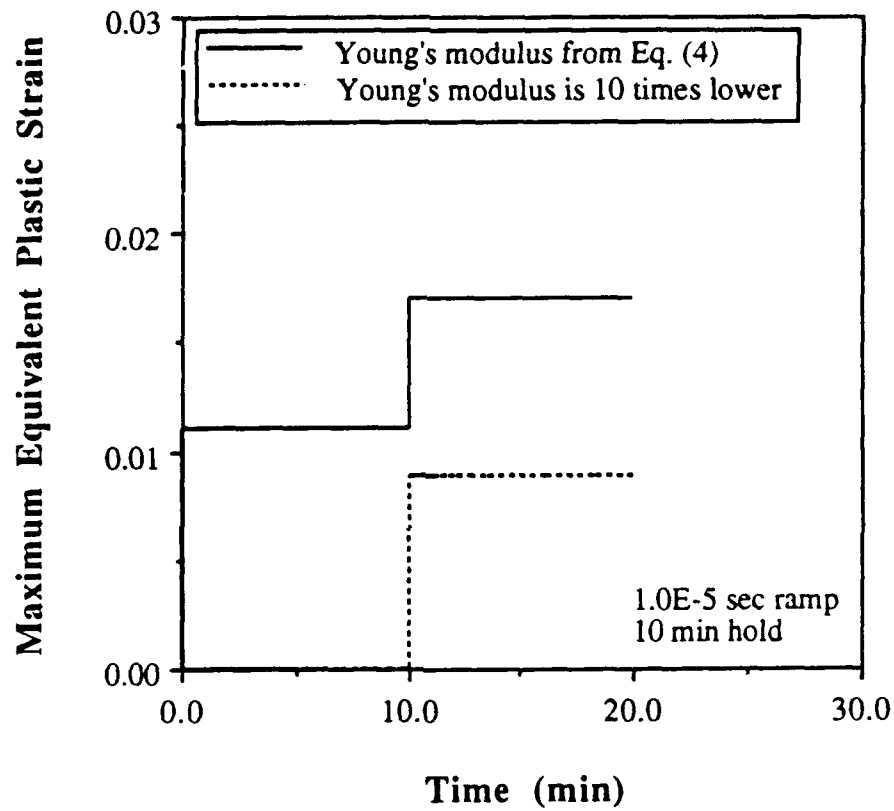


Figure 3.20 Maximum equivalent plastic strain versus time of the cycle with 1.0E-5 sec ramp and 10 minutes hold for different Young's moduli

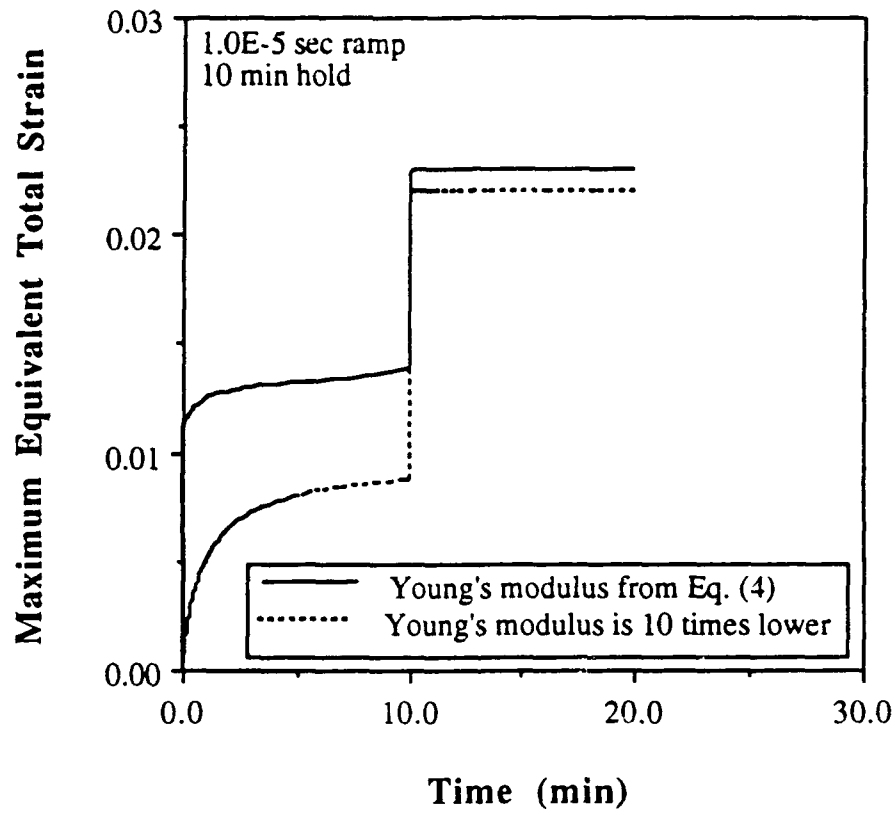


Figure 3.21 Maximum equivalent total strain versus time of the cycle with 1.0E-5 sec ramp and 10 minutes hold for different Young's moduli

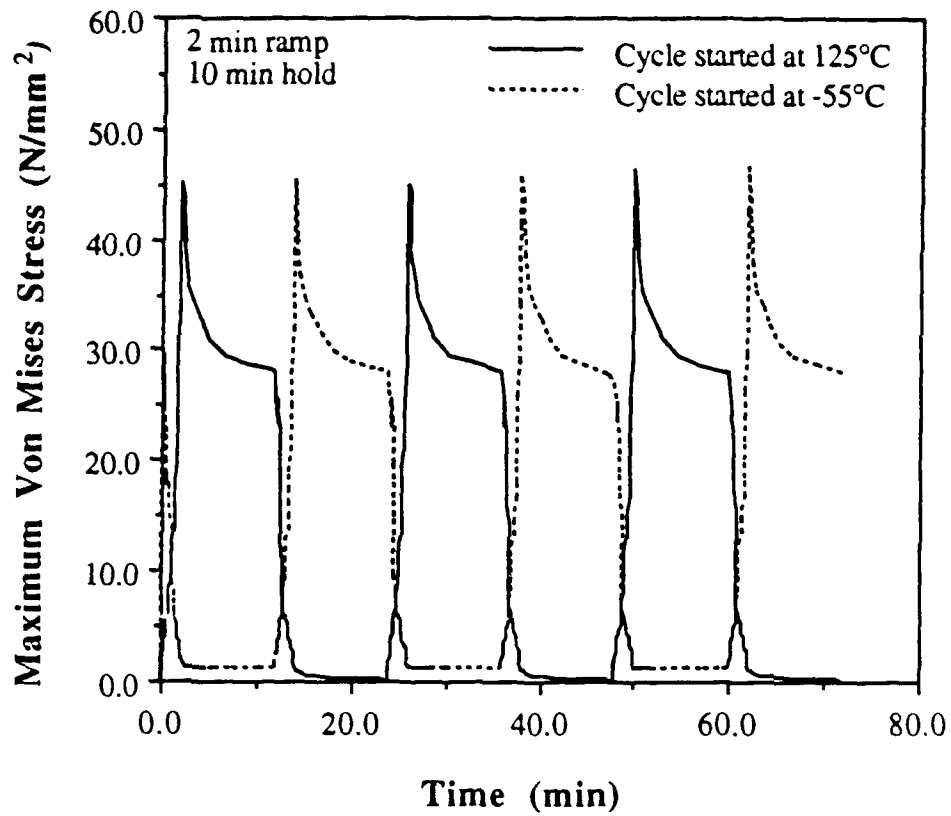


Figure 3.22(a) Maximum von Mises stress versus time for initial temperature conditions 125°C and -55°C

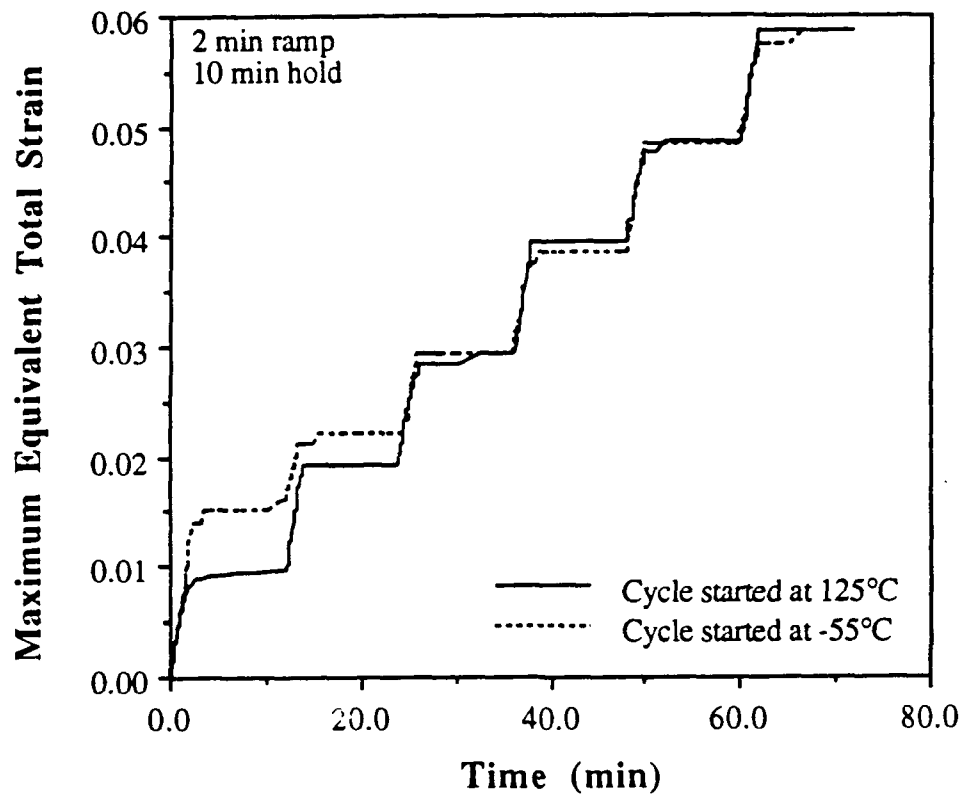


Figure 3.22(b) Maximum equivalent total strain versus time for initial temperature conditions 125°C and -55°C

COMMAND	NAME	DISPLAY	ACTIVE	WINDOW	VIEW	SET/SHOW	PLOT	HI
---------	------	---------	--------	--------	------	----------	------	----

FINITE ELEMENT MESH (ONE JOINT)

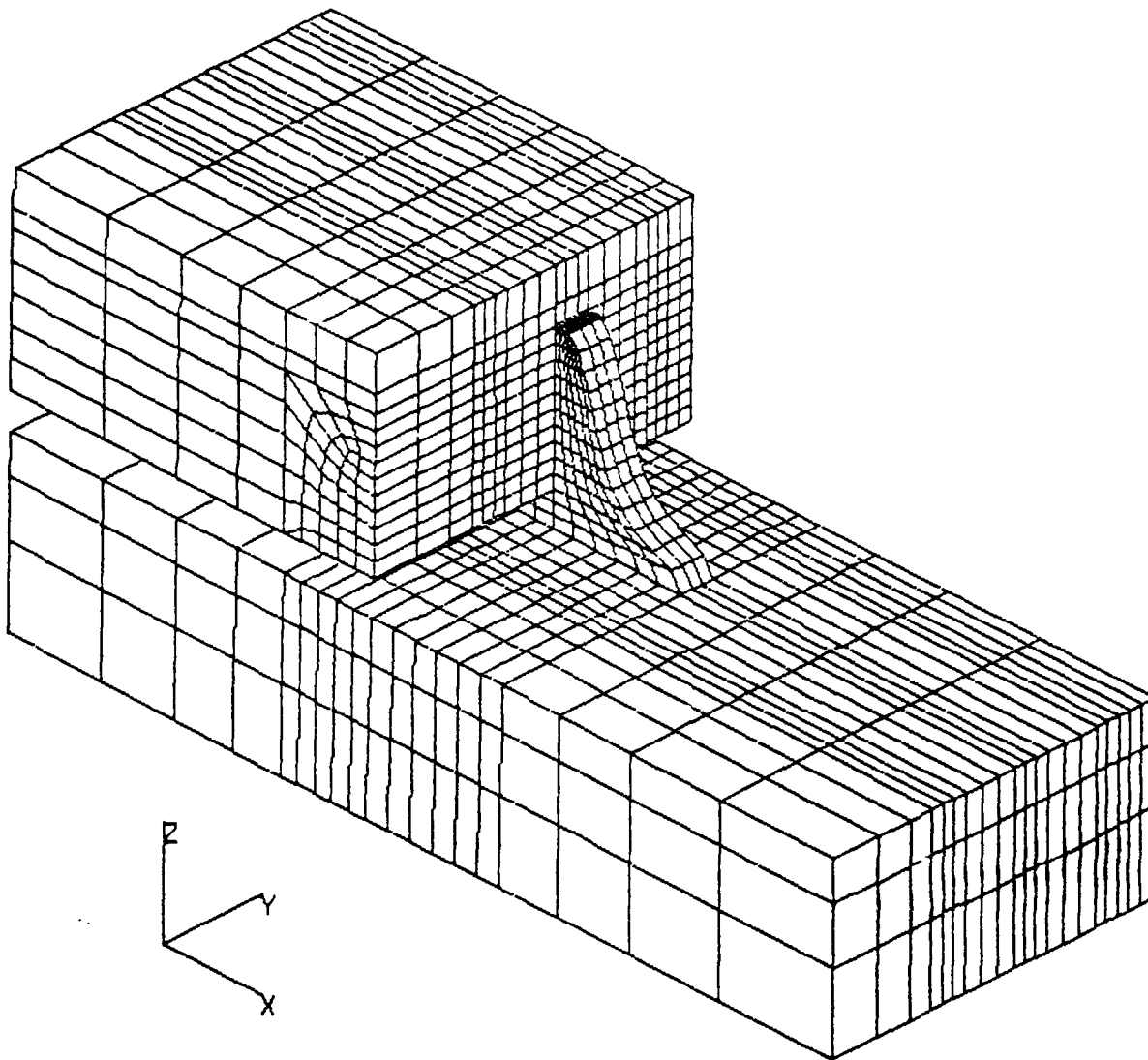


Figure 3.23(a) 3-D finite element model

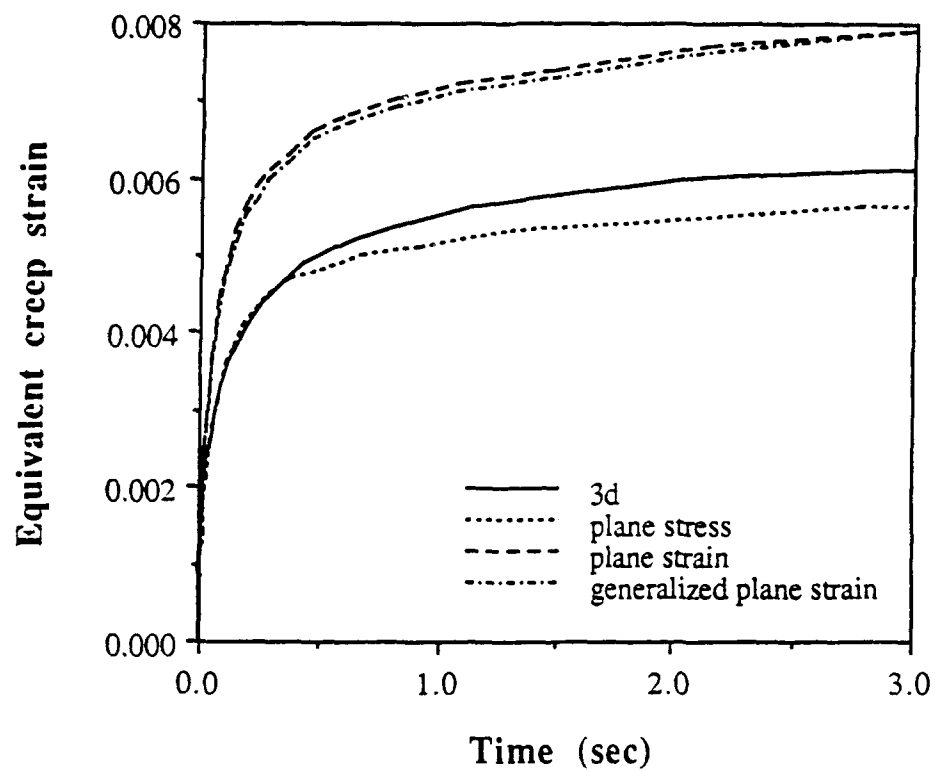


Figure 3.23(b) Maximum equivalent creep strain versus time for 2D and 3D models

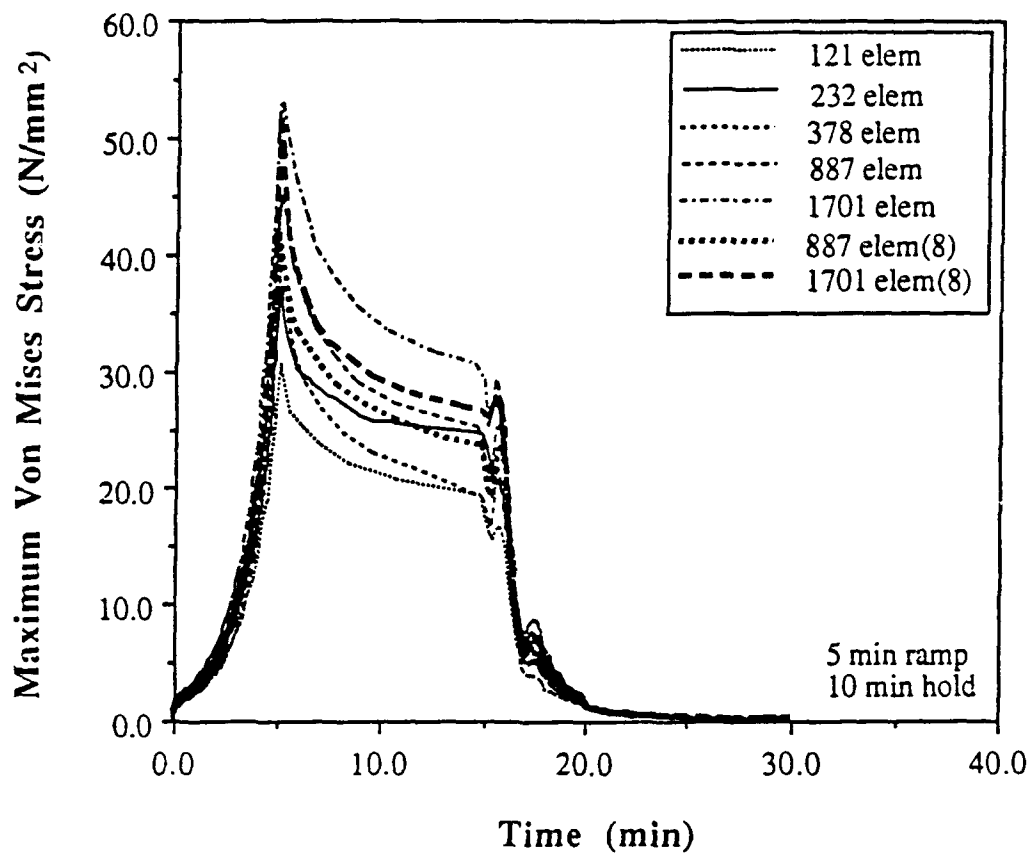


Figure 3.24(a) Maximum von Mises stress versus time for different mesh refinements

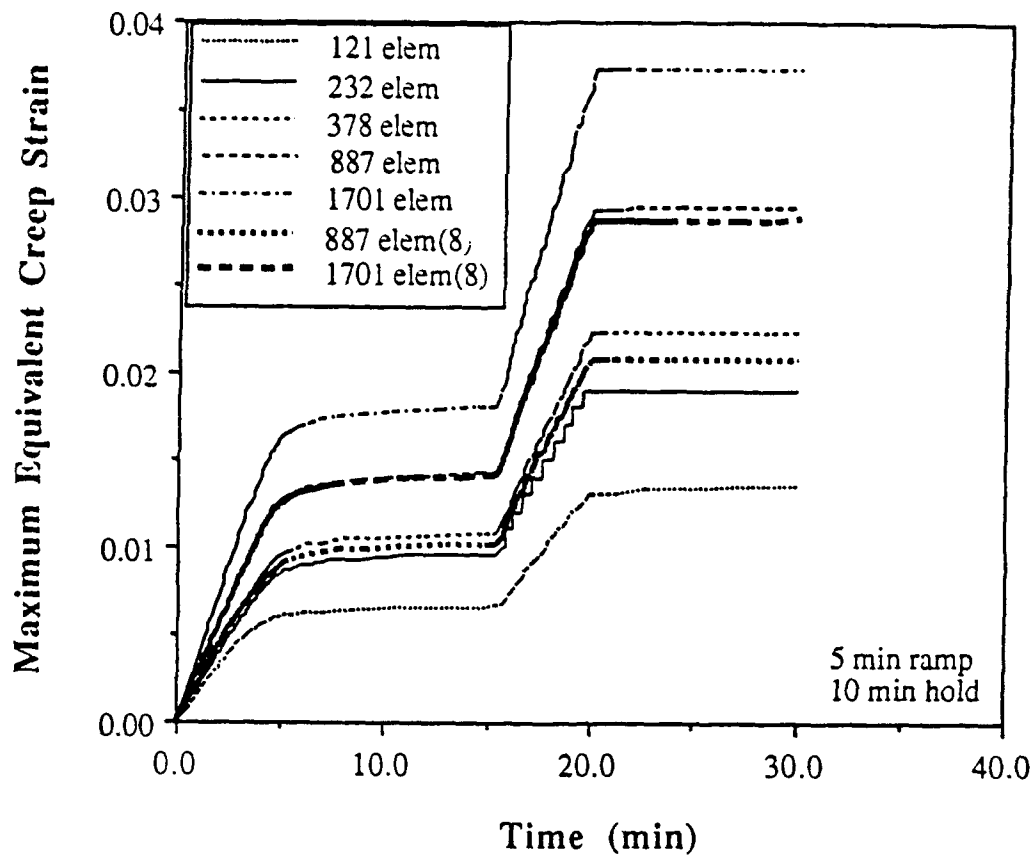


Figure 3.24(b) Maximum equivalent total strain versus time for different mesh refinements

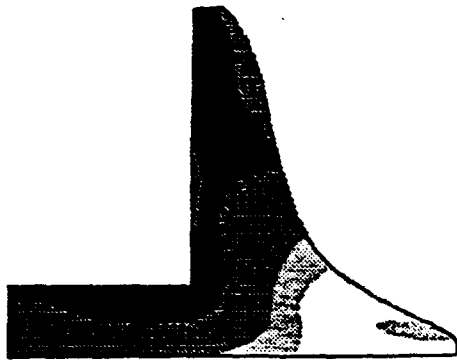


Figure 3.25(a)

The distribution of von Mises stress (MPa) after 5 minutes ramp from 125°C to -55°C with the mesh of 232 elements

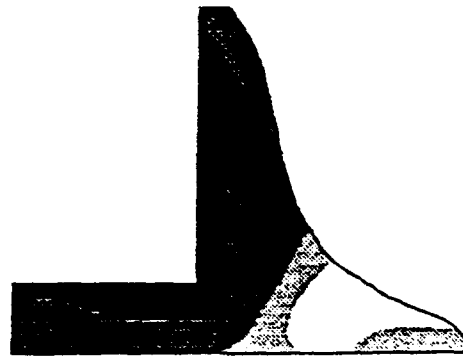


Figure 3.25(b)

The distribution of von Mises stress (MPa) after 5 minutes ramp from 125°C to -55°C with the mesh of 1701 elements

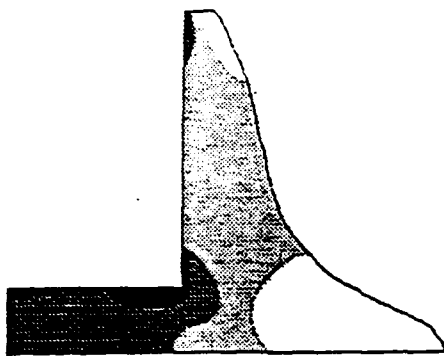


Figure 3.25(c)

The distribution of equivalent creep strain after 10 minutes hold at 125°C with the mesh of 232 elements

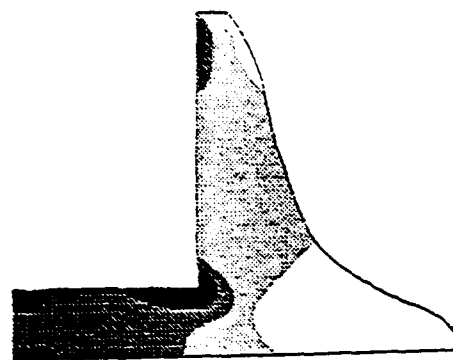


Figure 3.25(d)

The distribution of equivalent creep strain after 10 minutes hold at 125°C with the mesh of 1701 elements

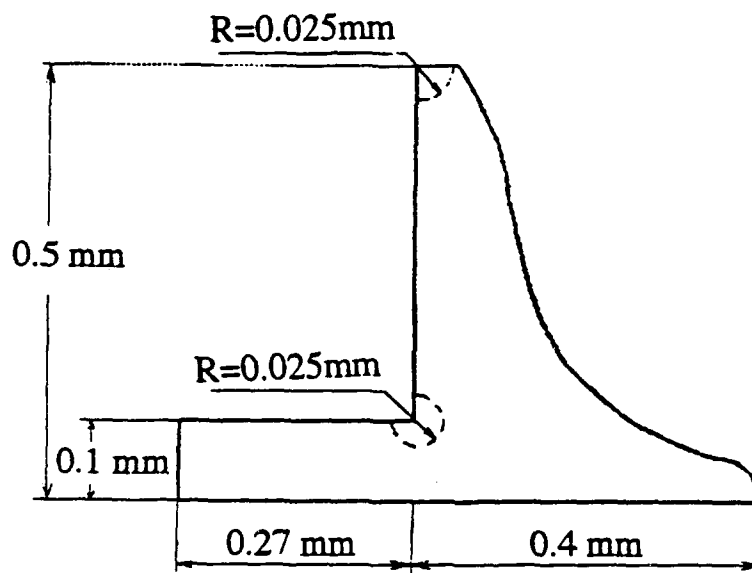


Figure 3.26 A close proximity of the concentration points are chosen on the arc with its characteristic radius R for predicting fatigue

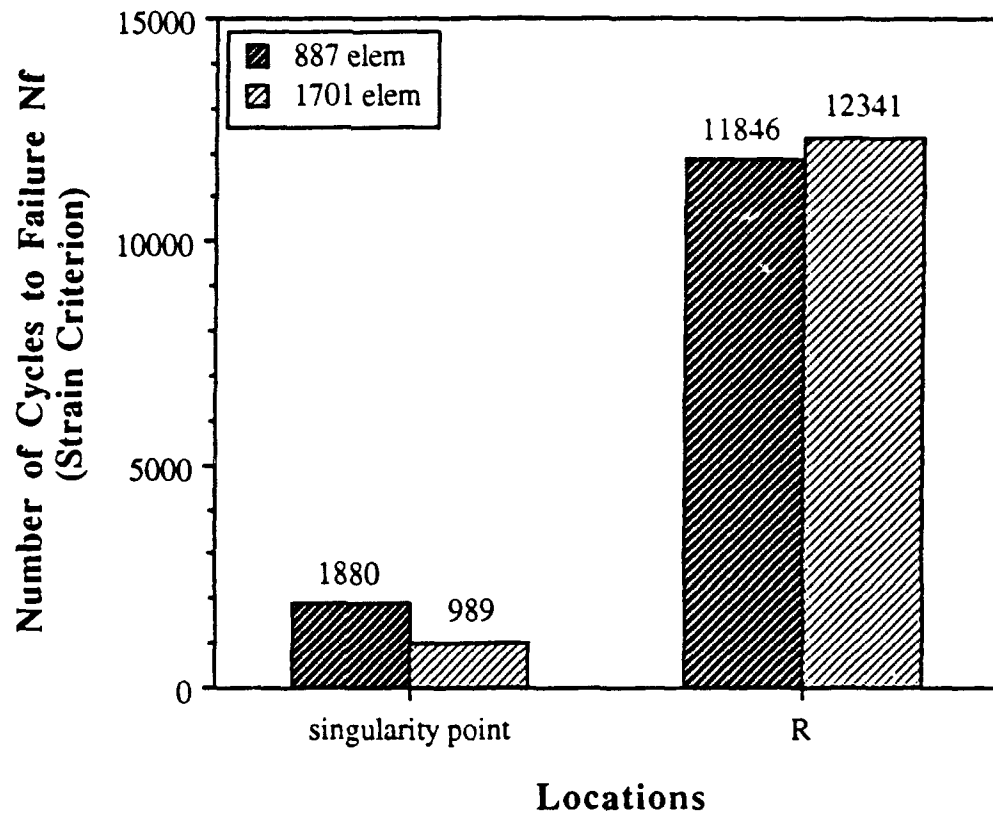


Figure 3.27 Number of cycles to failure of two mesh refinement using strain criterion

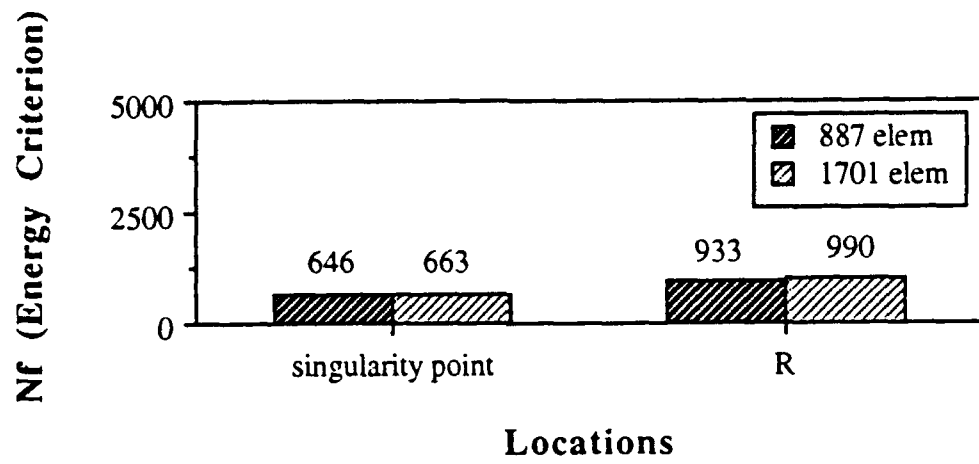


Figure 3.28 Number of cycles to failure using energy criterion

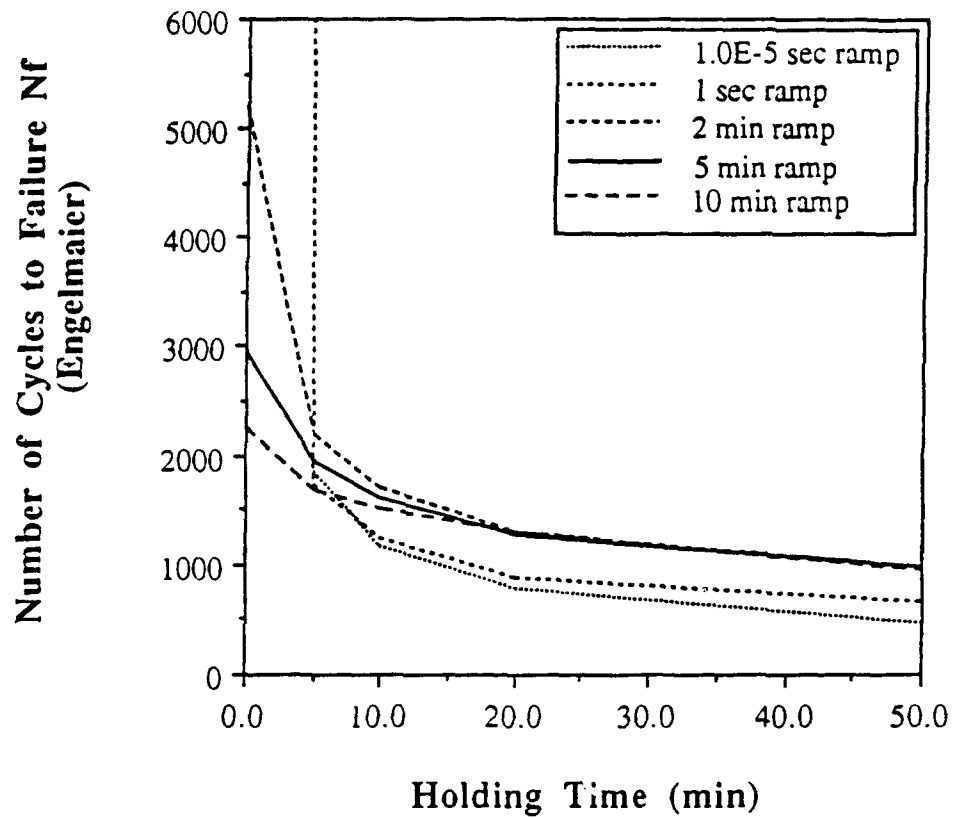


Figure 3.29(a) Number of cycles to failure as a function of hold time, predicted by Engelmaier equation

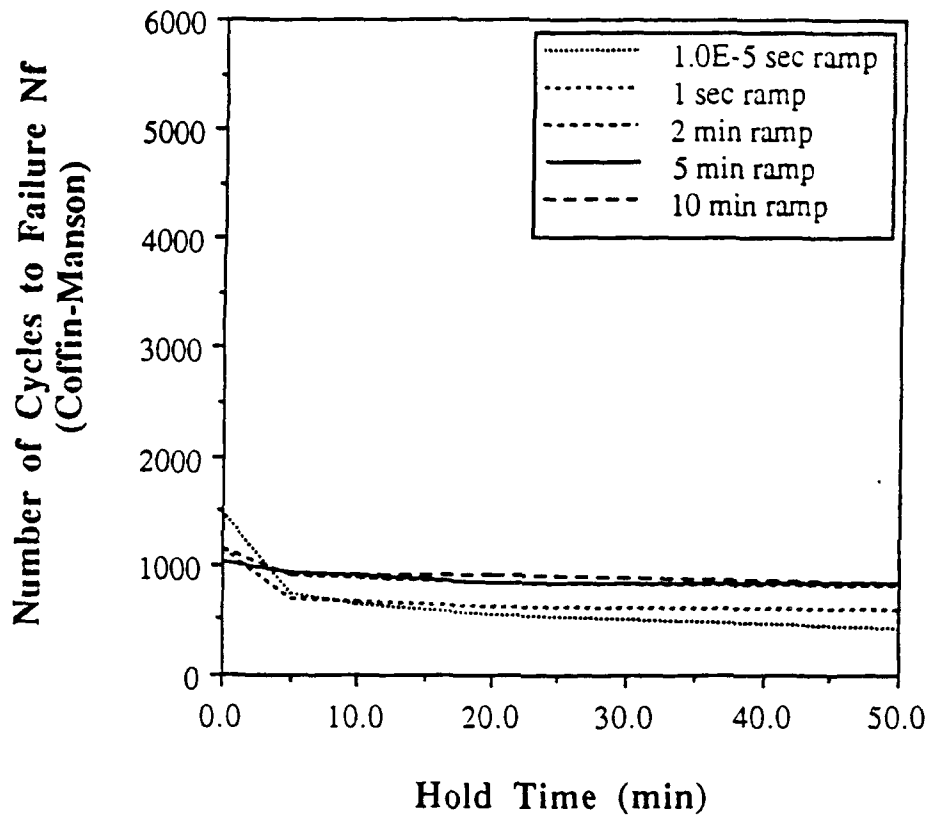


Figure 3.29(b) Number of cycles to failure as a function of hold time, predicted by Coffin-Manson equation

COMMAND	NAME	DISPLAY	ACTIVE	WINDOW	VIEW	SET/SHOW	PLOTTING
---------	------	---------	--------	--------	------	----------	----------

MATERIAL PROPERTIES

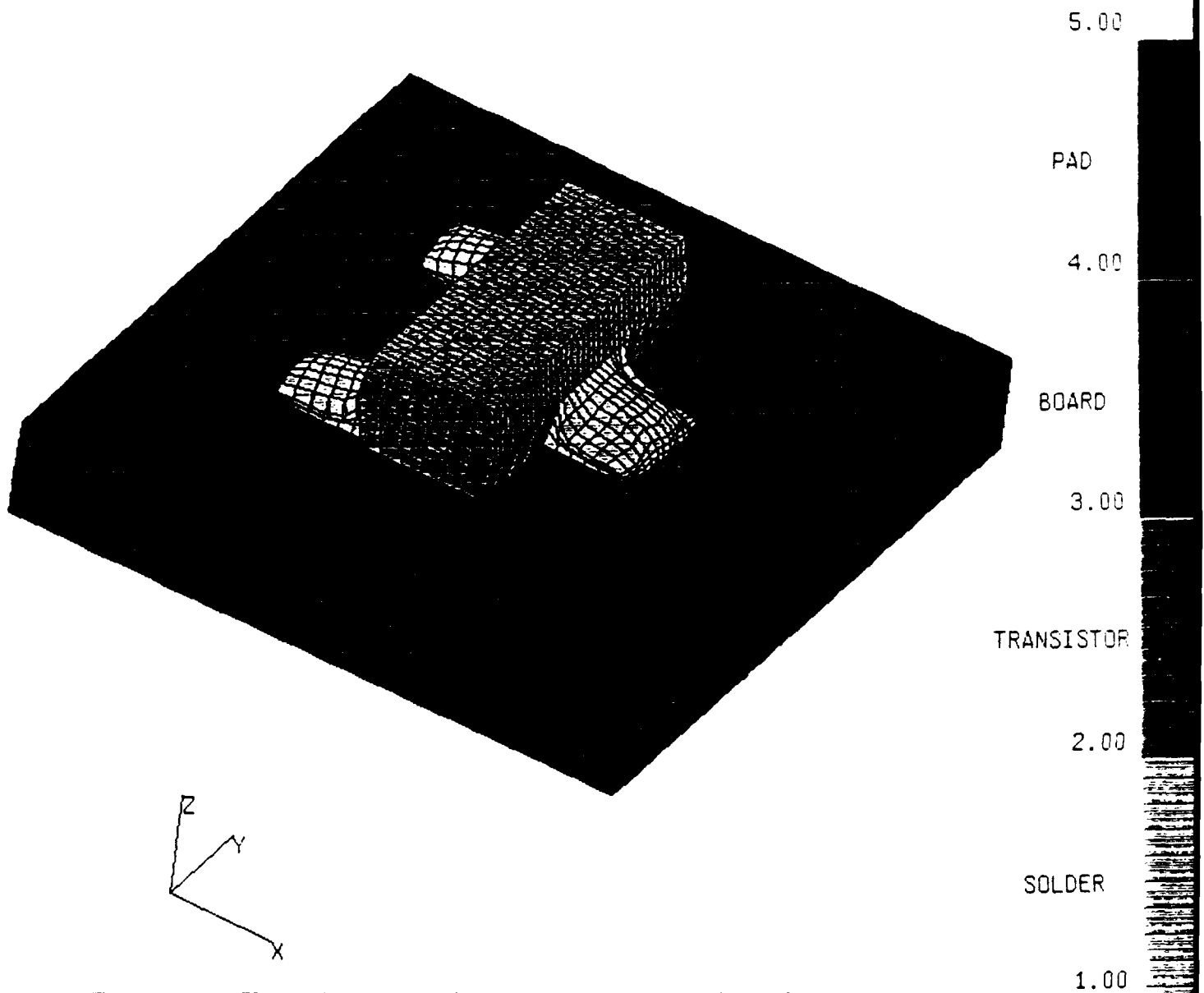


Figure 3.30 Three dimensional finite element mesh for a three-joint structure

COLOR CODE BY PROPERTY ID

```

INPUT CURSOR CONTROL COMMANDS TO DEFINE THE START OF THE TITLE
INPUT THE TITLE
MATERIAL PROPERTIES
INPUT DIRECTIVE OR "END"
  
```

COMMAND NAME DISPLAY ACTIVE WINDOW VIEW SET/SHOW PLOT

VON MISES STRESS (MPA)

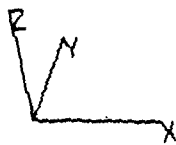
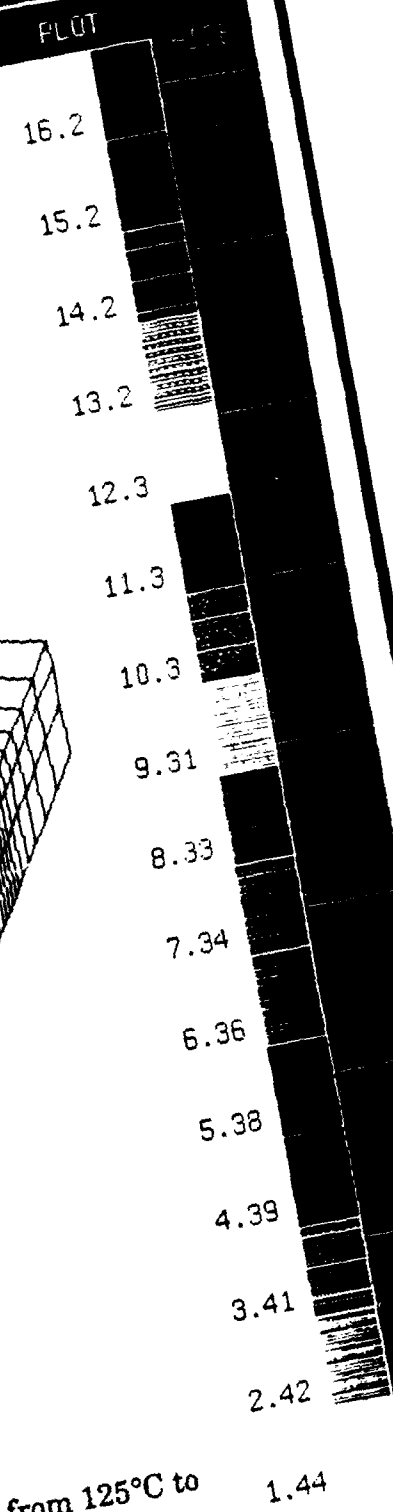
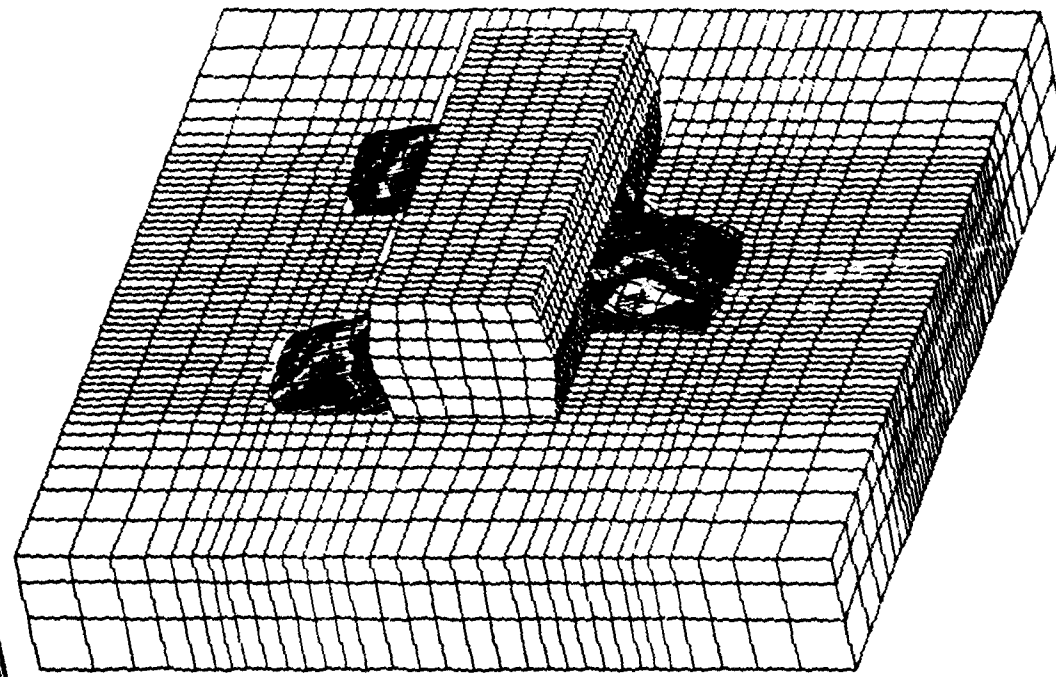


Figure 3.31 Von Mises stress distribution after 5 minutes ramp from 125°C to

-55°C

ABAQUS V4-9-1
PROCEDURE 21

23-FEB-93
TIME STEP

2 15:52:37
INCREMENT

6756

5

9254

END

HE

COMMAND

NAME

DISPLAY

ACTIVE

WINDOW

VIEW

SET/SHOW

PLOT

VON MISES STRESS (MPa)
10 MIN DWELL AT -55C

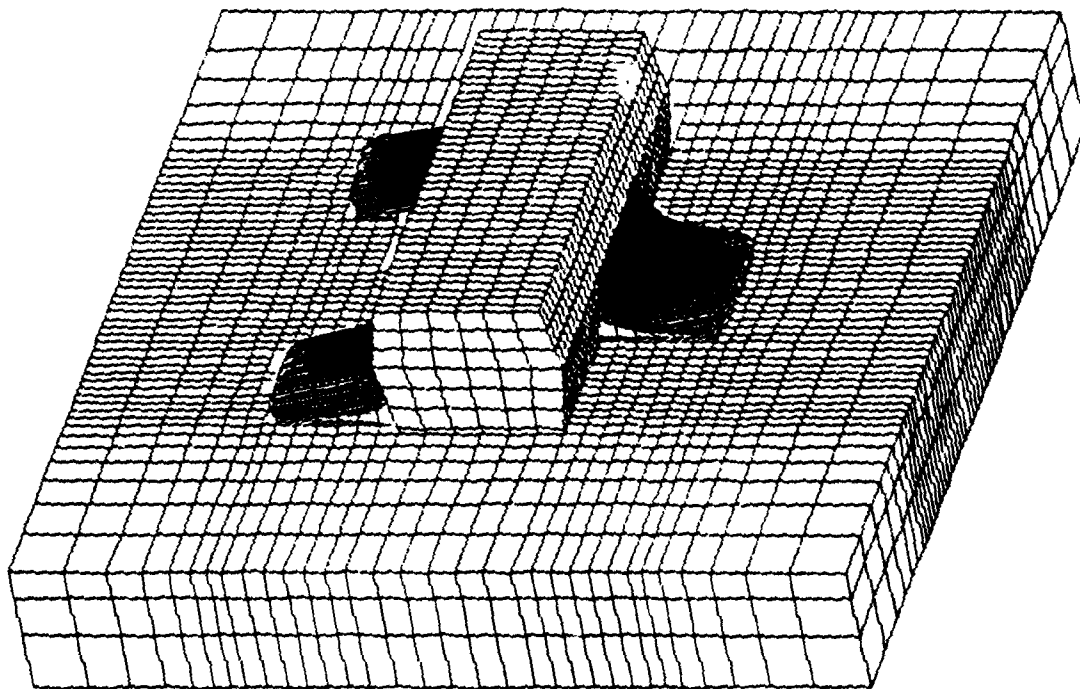


Figure 3.32 Von Mises stress distribution after 10 minutes hold at -55°C

ABAQUS V4-9-1
PROCEDURE 22

23-FEB-93
TIME STEP

2

15:52:37
INCREMENT

6756

105

9254

CONTINUE OR "END"

END

COMMAND

NAME

DISPLAY

ACTIVE

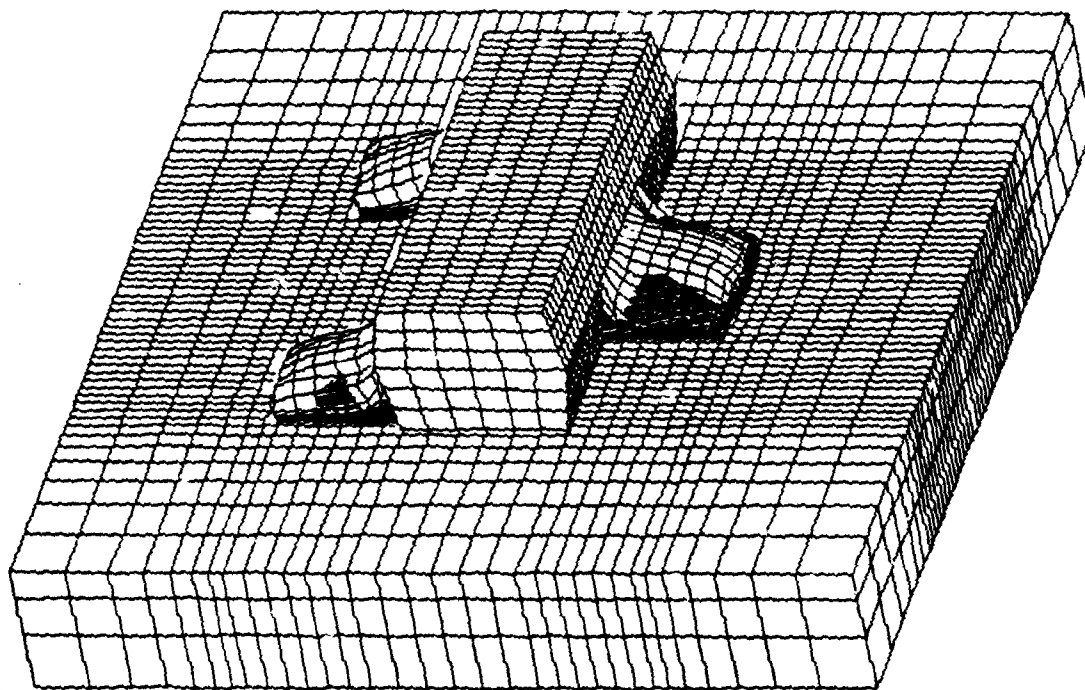
WINDOW

VIEW

GET/SHOW

PLOT

MAGNITUDE OF CREEP STRAIN



.0353

.0330

.0306

.0283

.0260

.0236

.0213

.0190

.0166

.0143

.0120

.00964

.00730

.00497

.00264

.000305

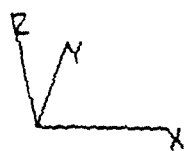


Figure 3.33 Creep strain distribution after 5 minutes ramp from 125°C to

-55°C

ABAQUS V4-9-1
PROCEDURE 21

23-FEB-93
TIME STEP

2 15:52:37
INCREMENT

6756
5

9254

END

HE

ABAQUS V4-9-1 23-FEB-93 15:52:37 6756 9254

COMMAND NAME DISPLAY ACTIVE WINDOW VIEW SET/SHOW PLOT

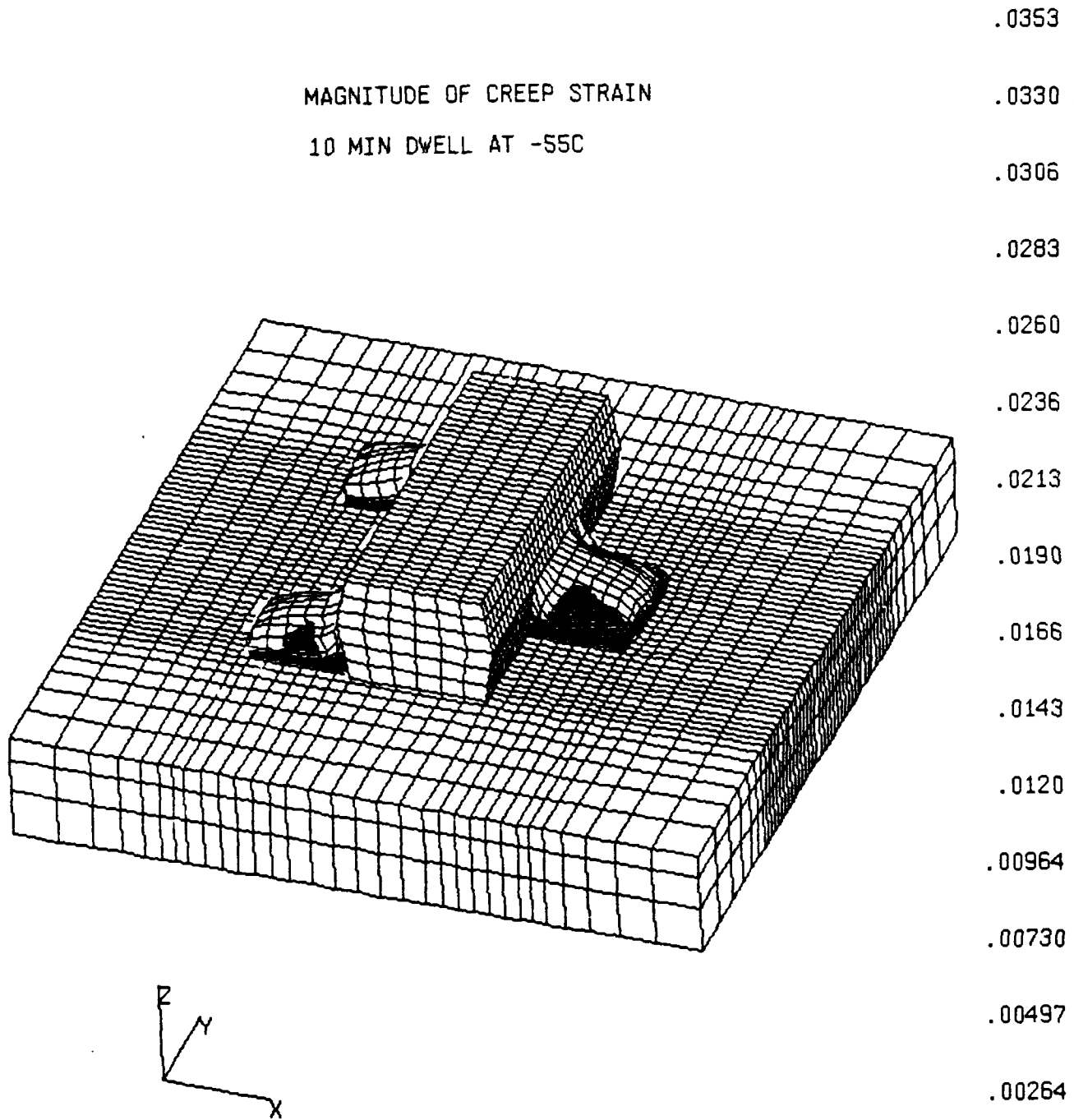


Figure 3.34 Creep strain distribution after 10 minutes hold at -55°C

ABAQUS V4-9-1 23-FEB-93 15:52:37 6756 9254
PROCEDURE 22 TIME STEP 2 INCREMENT 105

END

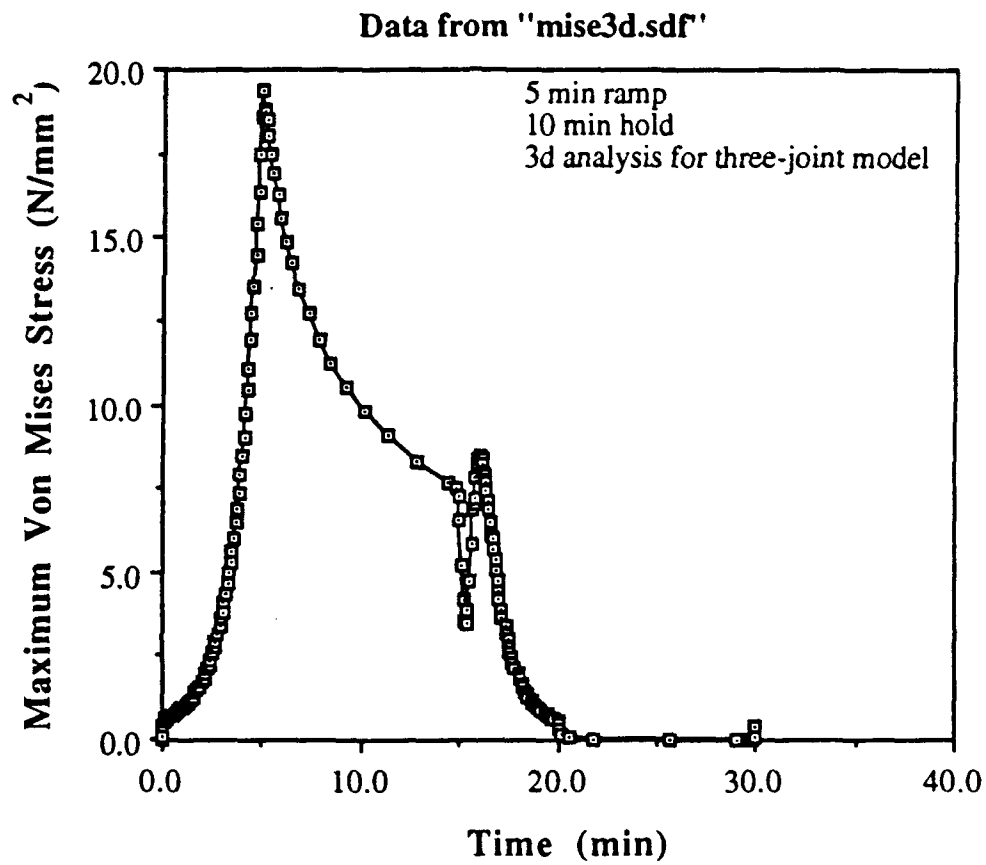


Figure 3.35 Maximum von Mises stress versus time of a cycle for the three-joint structure

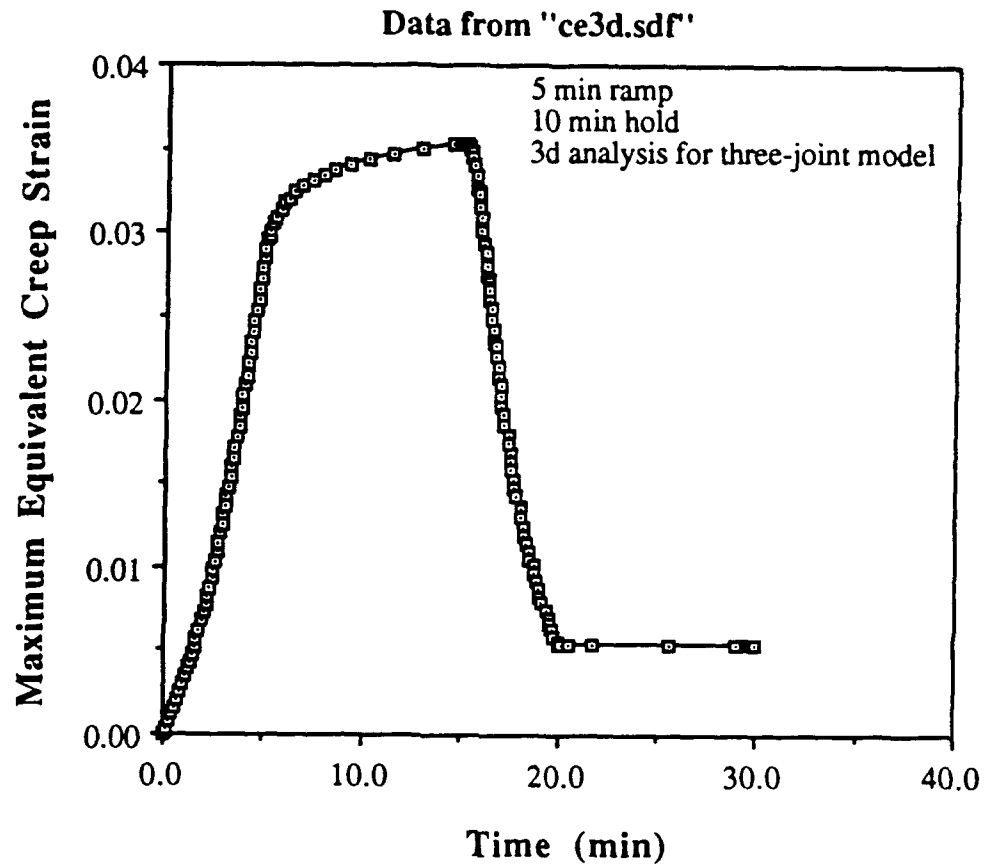


Figure 3.36 Maximum equivalent creep strain versus time of a cycle for the three-joint structure

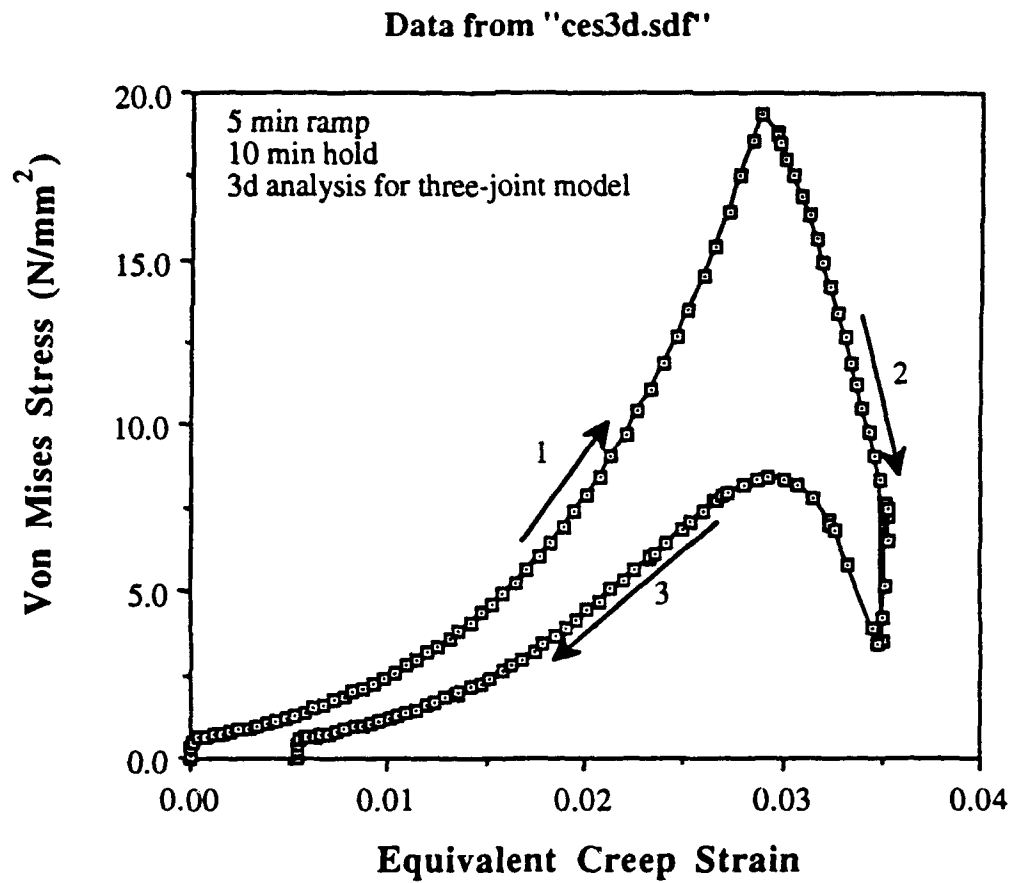


Figure 3.37 Creep energy dissipation density

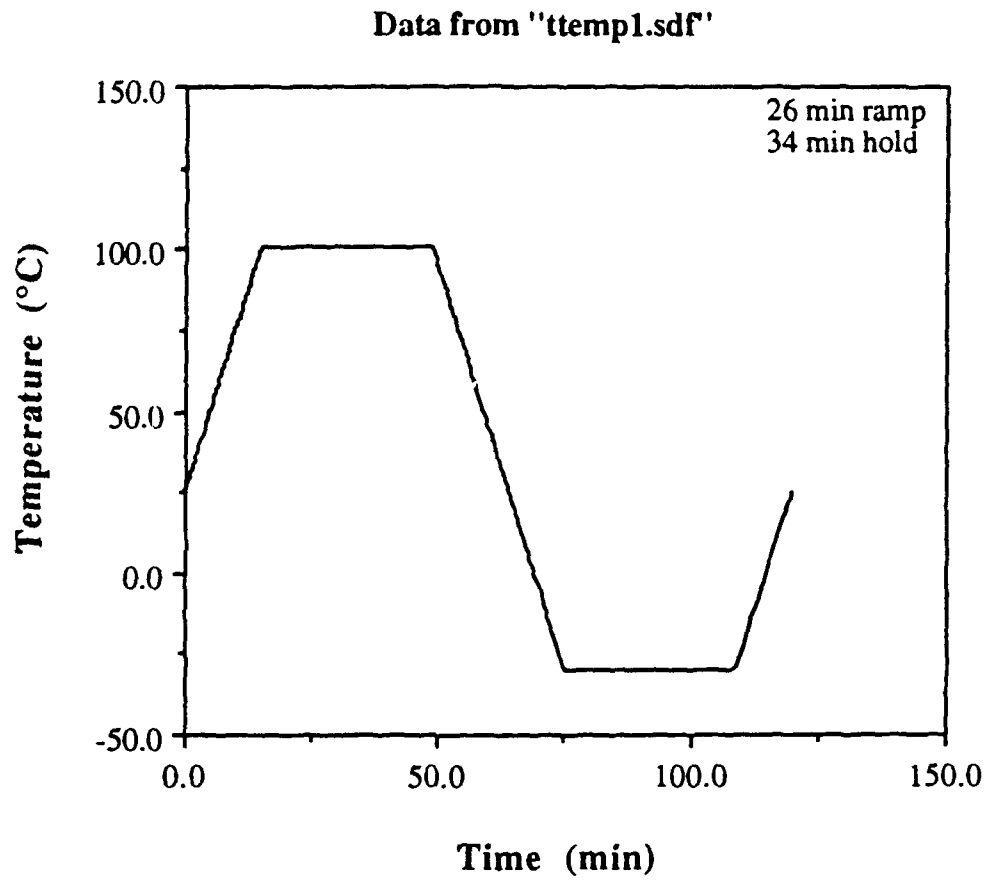


Figure 3.38 Temperature cycling profile

PCB and Release 3.5 PDA Engineering

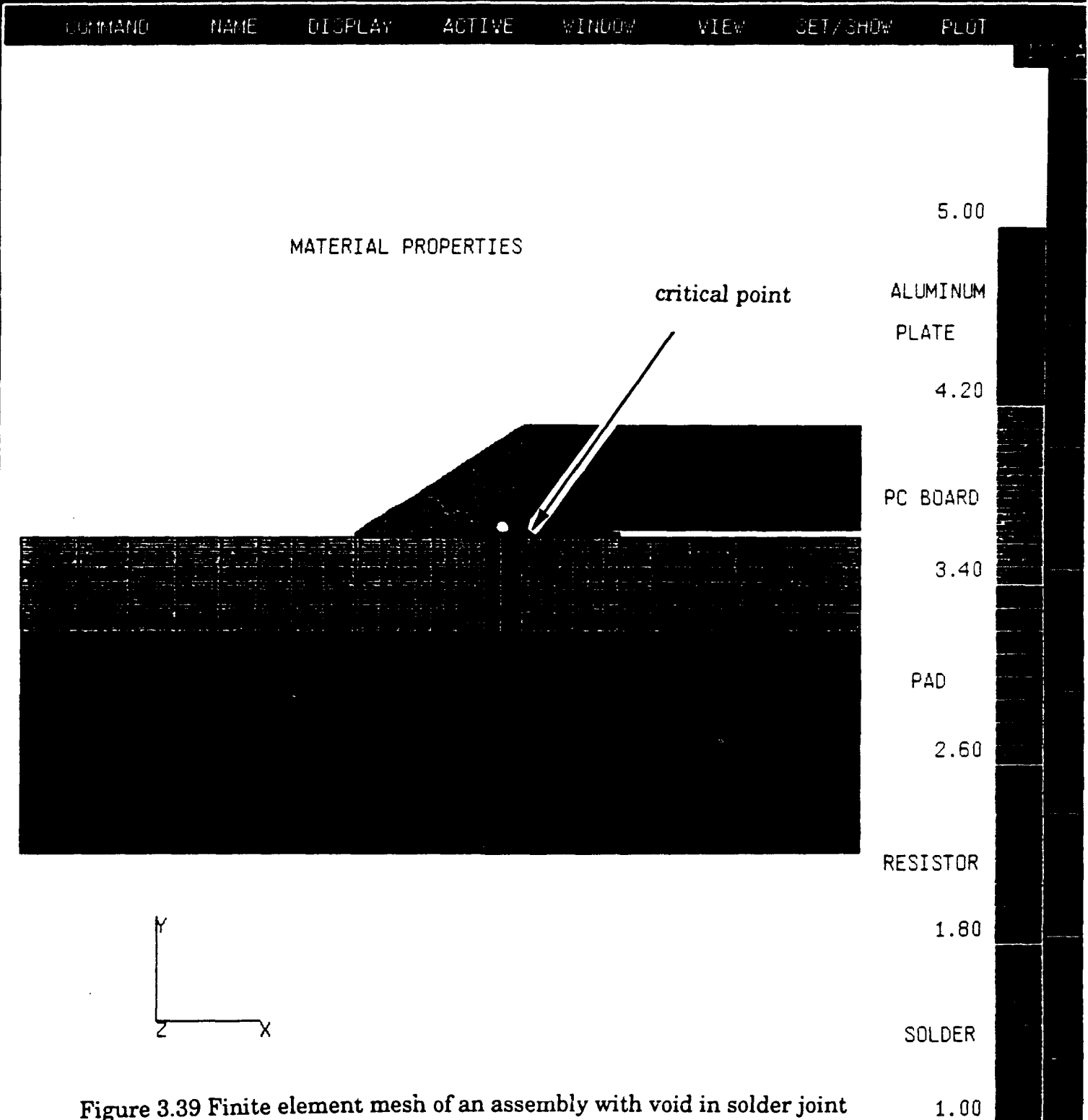


Figure 3.39 Finite element mesh of an assembly with void in solder joint

COLOR CODE BY PROPERTY ID

INPUT CURSOR CONTROL COMMANDS TO DEFINE THE START OF THE TITLE
 INPUT THE TITLE
 MATERIAL PROPERTIES

EN

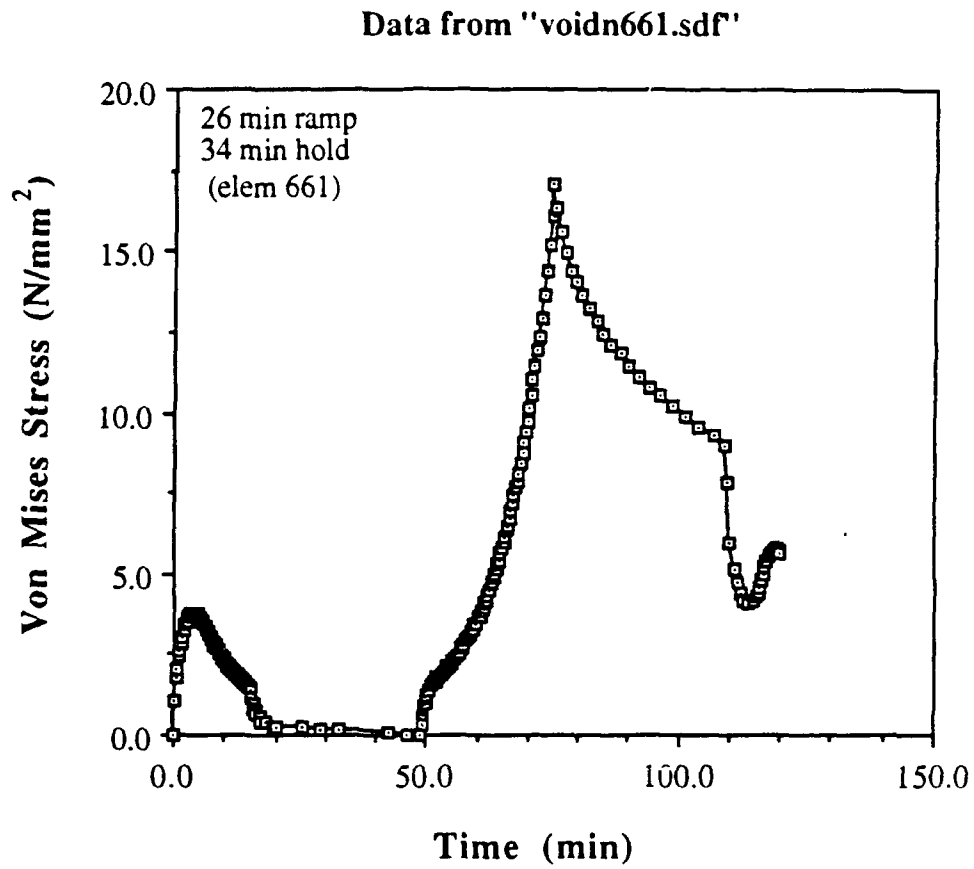


Figure 3.40 Maximum von Mises stress versus time of a cycle for an assembly with void in solder joint

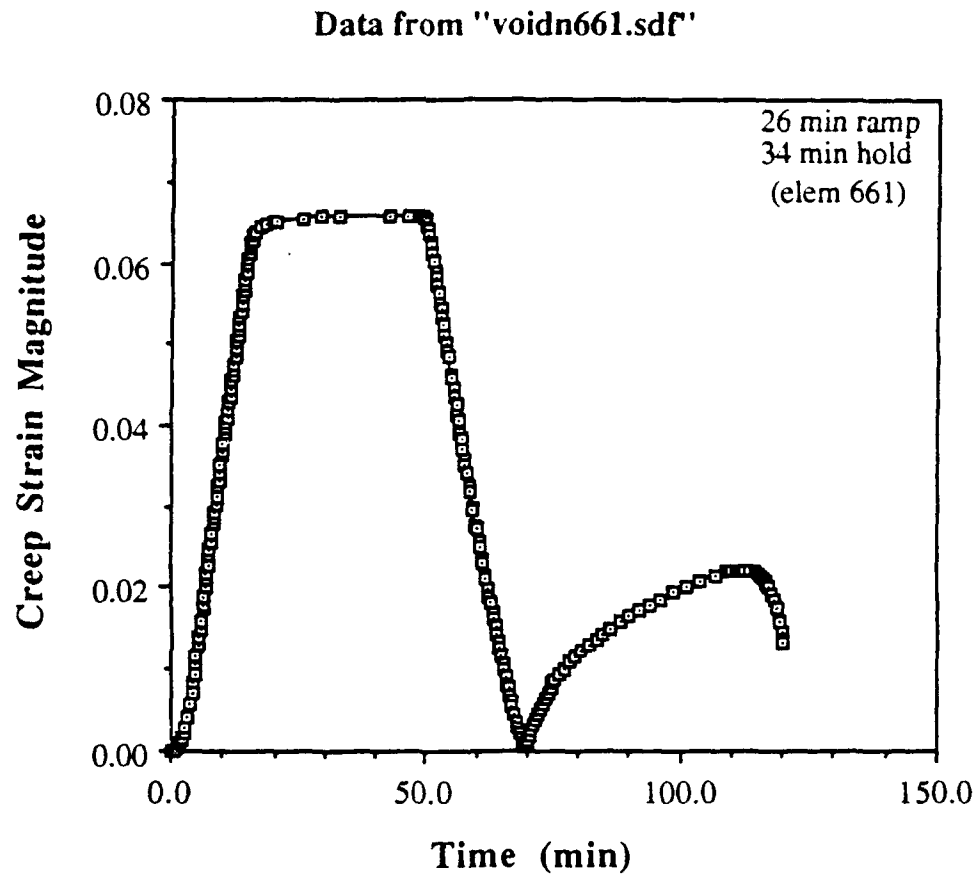


Figure 3.41 Maximum creep strain magnitude versus time of a cycle for an assembly with void in solder joint

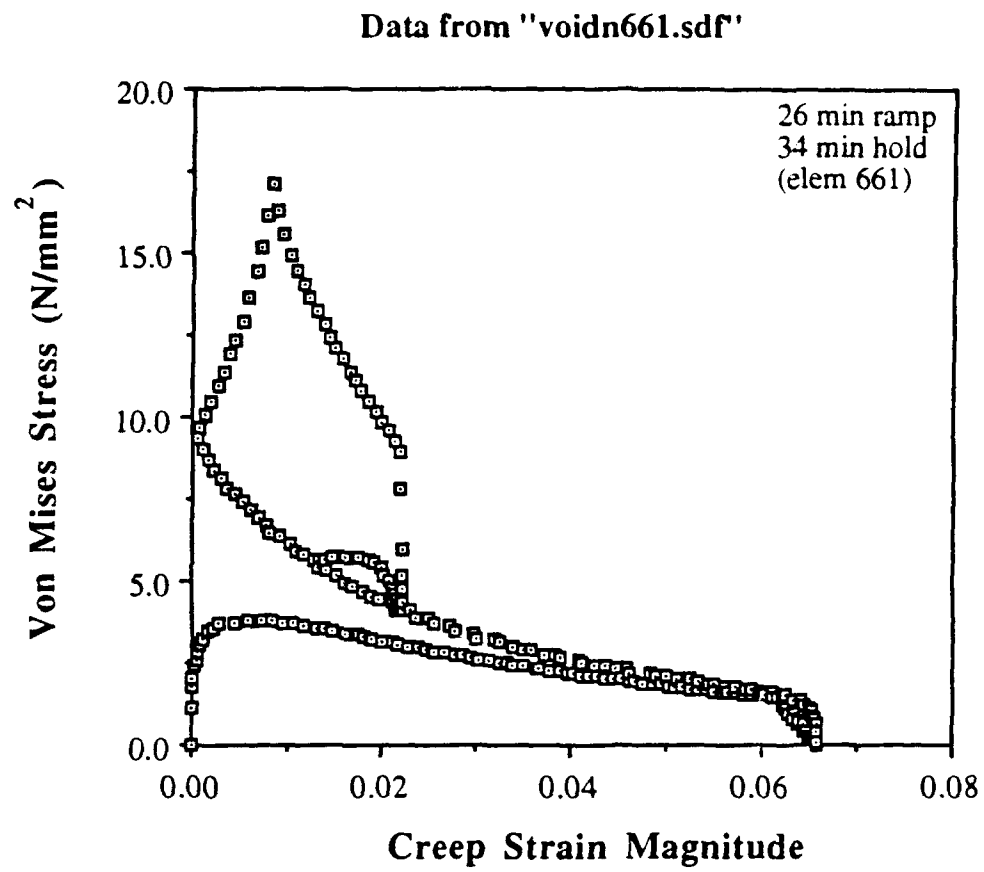


Figure 3.42 Creep energy dissipation density

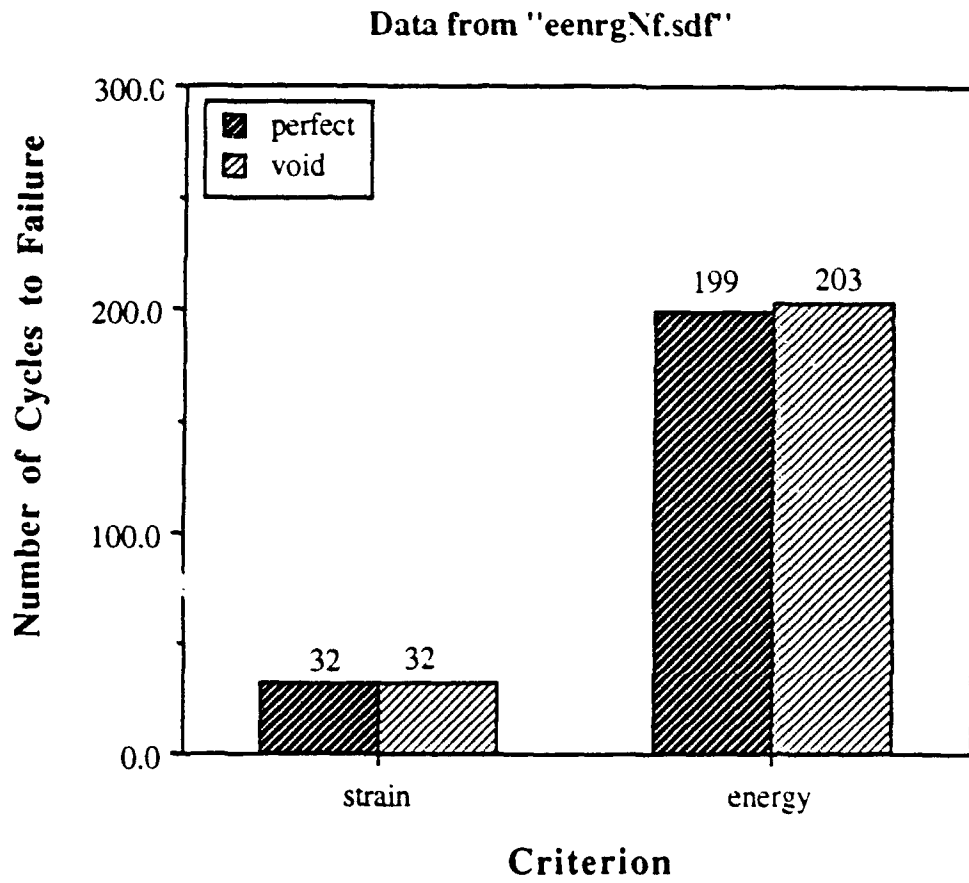
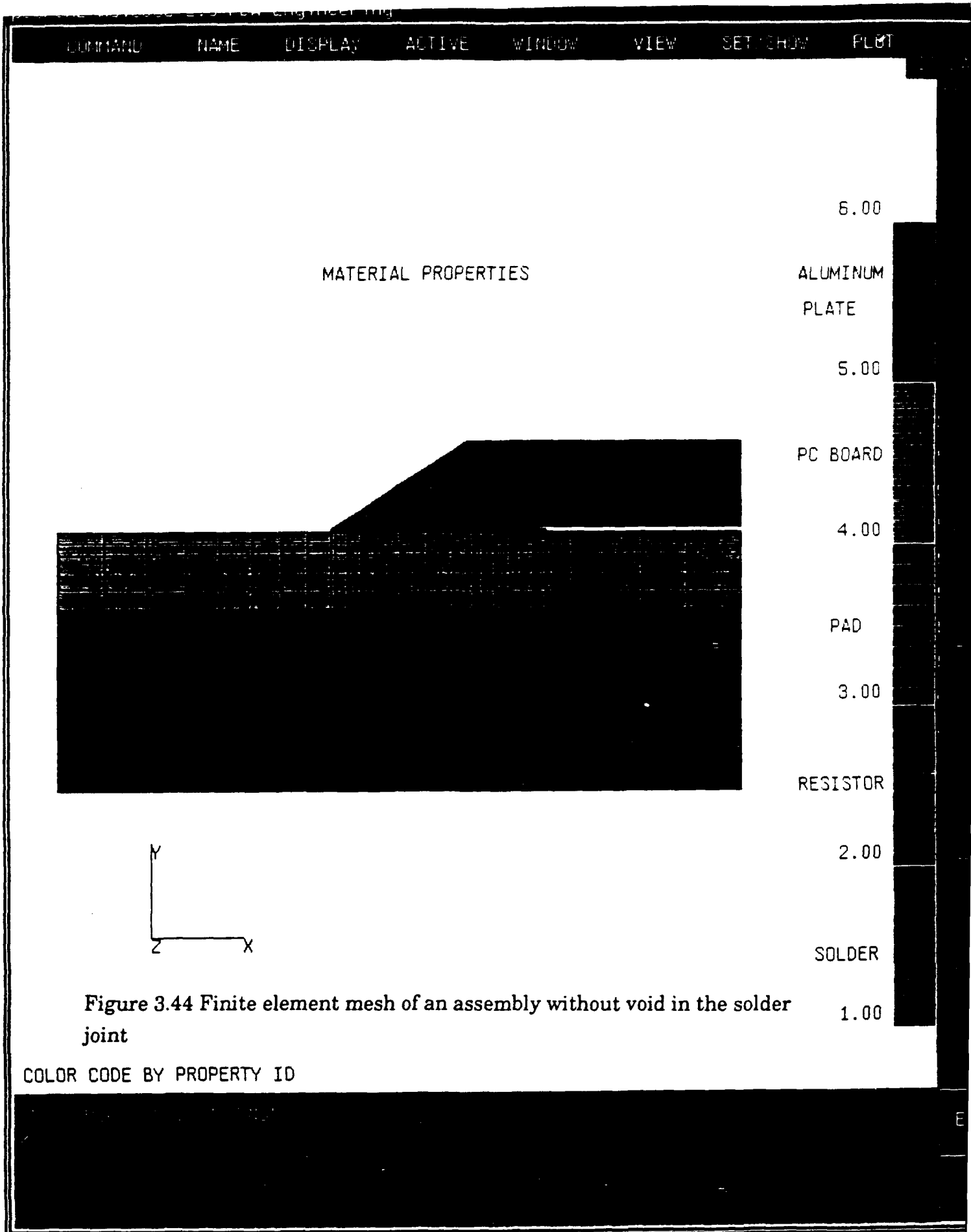


Figure 3.43 Fatigue life of the solder predicted by both failure criteria



patric and reference 2.5 FOR Engineering

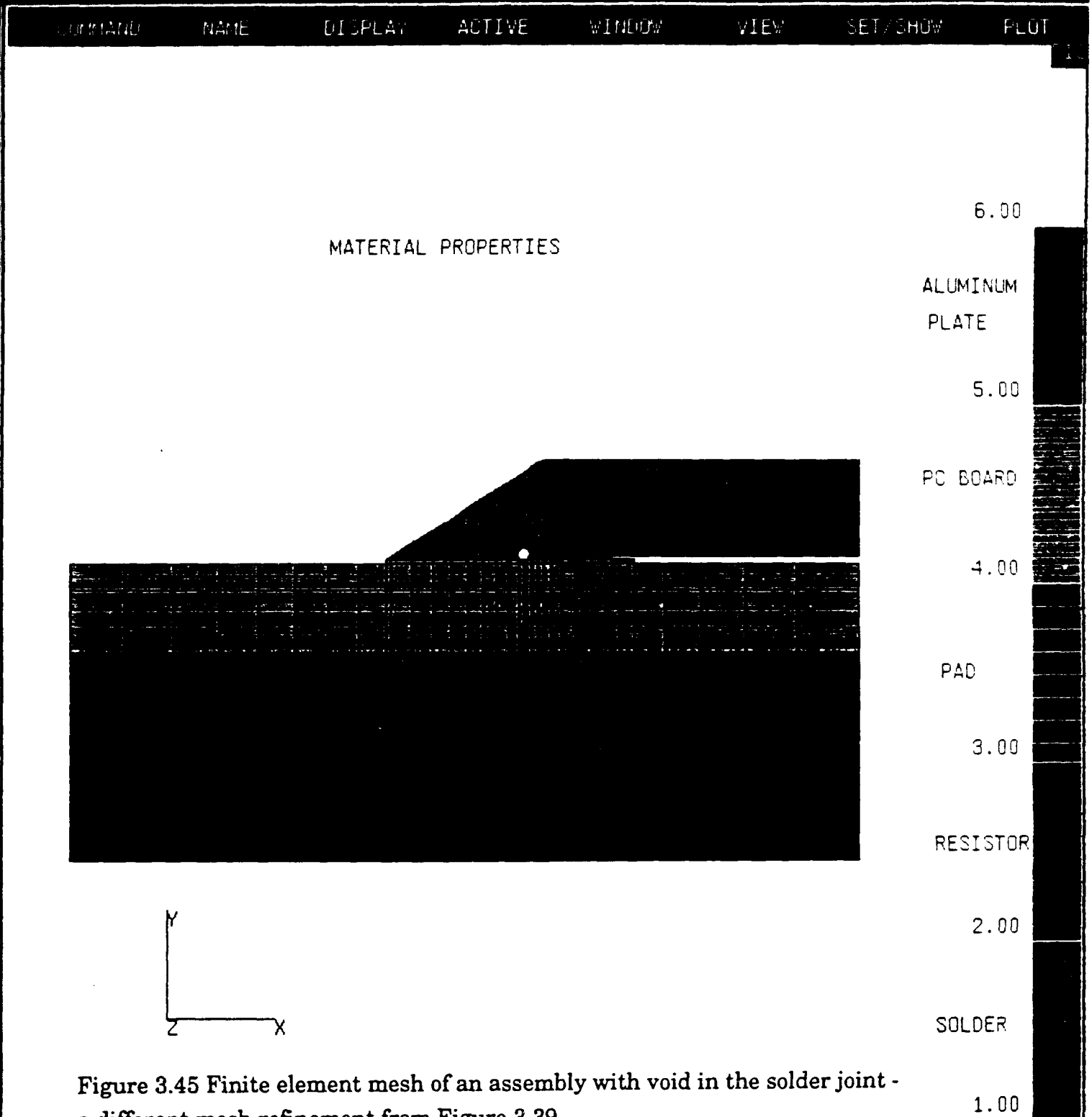


Figure 3.45 Finite element mesh of an assembly with void in the solder joint - a different mesh refinement from Figure 3.39

COLOR CODE BY PROPERTY ID

4. CONCLUSIONS

A creep-plasticity model is implemented for thermal load response of solder joints. Factors affecting the prediction of solder joint life are studied. Some important results are summarized as follows:

1. Results for cyclic thermal loads indicate excessive stresses and strains. Fatigue damage of solder joint is mainly because of the excessive accumulation of cyclic inelastic strain. It is observed that plastic strains are dominant under faster ramp (ramp time < 2 min), creep strain are dominant under slower ramp (ramp time ≥ 2 min), elastic strains are negligible. The strains are highest at the end of the loading cycle, while the highest stresses take place at the end of first step when the temperature ramp from the highest to the lowest.
2. Although the existing models and material properties show disparity, calculated total inelastic strains are in close agreement. The higher Young's modulus for solder results in higher maximum von Mises stress and equivalent plastic strain, but lower maximum equivalent creep strain. Thermal expansion mismatch between solder and ceramic causes high stress and strain concentrations at sharp corners.
3. Finite element modeling of stress and strain concentrations require excessive mesh refinements and hence lead to expensive solutions, especially in 3D. Choosing a close proximity of a concentration point as the point to monitor for predicting fatigue is a more cost effective and reliable solution strategy.
4. The increase of hold time at the maximum and the minimum temperatures in cyclic thermal loading results in the reduction of the life to

failure. The increase of ramp time results in the decrease of the total strain. The effect of grain size and initial temperature on the thermal fatigue life to failure is insignificant.

5. The plane stress model gives the results which are reasonably close to the 3D model, while the plane strain model, as expected, has less accuracy in predicting the strain for this special case. For irregularly shaped solder geometry, the use of three-dimensional models may, however, be more important.
6. The number of life to failure predicted by strain-energy partitioning is more sensitive to the variations in creep properties, while the one predicted by strain-life relationship is less sensitive.
7. The energy-based failure criterion gives the results which is more close to the ones from experiment test.
8. The results from the strain energy-partitioning method are insensitive to mesh refinement even at singularity points, while the strain-life relationship is less sensitive only at the location far enough from the singularity point.
9. For the limited studies made here, the energy-based and strain-based failure criteria may give conflicting predictions of fatigue damage accumulation, and therefore, conflicting predictions of fatigue life.
10. The void in the solder joint has insignificant effect on the fatigue life to failure in the case studied here.
11. Due to nonlinearity of the problems and requirements for considerably fine meshes the CPU times are extensive. Table 4.1 summarizes some typical CPU times.

Table 4.1 CPU times for some typical 2D cases

Cycle time in minutes	Number of elements	Number of nodes	Machine	CPU in minutes
30	121	150	Sun/Sparc2	27
30	232	266	Sun/Sparc2	55
30	378	430	Sun/Sparc2	100
30	887	963	Sun/Sparc2	259
30	1701	1808	Sun/Sparc2	798

REFERENCES

- ABAQUS , 1989, "Users' Manual," Hibbitt, Karlsson & Sorensen, Inc., Version 4.8.
- Akay, H. U., Tong, Y., and Paydar, N., 1993, "Thermal Fatigue Analysis of an SMT Solder Joint Using Nonlinear FEM Approach," *International Journal of Microcircuits and Electronic Packaging*, Vol. 16, Number 2, pp. 79-88.
- Coffin, L.F., Jr. and Schenectady, N. Y., 1954, "A Study of the Effects of Cyclic Thermal Stresses on a Ductile Metal," *Transactions of the ASME*, Vol.76, pp. 931-950.
- Dasgupta, A., Oyan, C., Barker, D., and Pecht, M, 1992, " Solder Creep-Fatigue Analysis by an Energy-Partitioning Approach," *ASME Journal of Electronic Packaging*, Vol. 114, pp.152-160.
- Engelmaier, W., 1983, "Fatigue Life of Leadless Chip Carrier Solder Joints During Power Cycling," *IEEE Transactions on Components, Hybrids, and Manufacturing Technology*, Sept. pp. 232-237, Vol. CHMT-6, No. 3.
- Frear, D.R., Jones, W.B., and Kinsman, K.R., 1990, (Editors), *Solder Mechanics - A State of the Art Assessment*, The Minerals, Metals and Materials Society, EMPMD Monograph Series, Santa Fe, New Mexico.
- Grivas, D., Murty, K. L., and Morris, J. W., Jr., 1979, "Deformation of Pb-Sn Eutectic Alloys at Relatively High Strain Rates," *Metallurgica*, Vol. 27, pp. 731-737.
- Lam, S. T., Arieli, A., and Mukherjee, A. K., 1979, "Superplastic Behavior of Pb-Sn Eutectic Alloy," *Materials Science and Engineering*, Vol. 40, pp. 73-79.

Lau, J.H, 1991, (Editor), *Solder Joint Reliability*, Van Nostrand Reinhold, New York.

Mohamed, F. A., and Langdon, T. G., 1976, "Deformation Mechanism Maps for Superplastic Materials," *Scripta Metallurgica*, Vol. 10, pp. 759-762.

Mohamed, F. A., and Langdon, T. G., 1975, "Creep Behavior in the Superplastic Pb-62% Sn Eutectic," *Philosophical Magazine*, Vol. 32, pp. 697-709.

Manson, S. S., *Experimental Mechanics*, 1965, Vol. 5, No. 7, pp. 193-226.

Pan, T. -Y., 1991, "Thermal Cycling Induced Plastic Deformation in Solder Joints - Part I: Accumulated Deformation in Surface Mount Joints," *Transactions of the ASME*, March, Vol. 113, pp. 8-15.

PATRAN, 1990, "User Manual," PATRAN Division, PDA Engineering, Vols.I & II.

Paydar, N., Tong, Y., and Akay, H. U., 1992, "A Finite Element Study of Factors Affecting Fatigue Life of Solder Joints," submitted to *ASME Journal of Electronic Packaging*.

Paydar, N., Tong, Y., and Akay, H. U., 1993, "A Finite Element Study of Fatigue Life Prediction Methods for Thermally Loaded Solder Joints," submitted to *ASME International Electronics Packaging Conference*, September 29-October 2, 1993, Binghamton, New York, USA.

Solomon, H. D., 1990, "High and Low Temperature Strain Life Behavior of a Pb Rich Solder", *ASME Journal of Electronic Packaging*, Vol. 112, pp. 113-128.

Wen, L. C. and Kovak, J., "Private Communication", Jet Propulsion Laboratory, Pasadena, California, 1993.

PART TWO

CREATION OF FINITE ELEMENT MESHES FROM INSPECTION MACHINES

1. STATEMENT OF THE PROBLEM

Historically, solder joint inspection has been visually performed by human inspectors who base the reliability of a solder joint on the cosmetic appearance of the visible surface judged in accordance with US Department of Defense (DoD-STD-2000) solder standards. However as the manufacturing of circuit boards becomes more complex due to the drive for a decrease in space utilization, the visual inspection process becomes difficult if not impossible. Hence, there is a need for numerical modeling of solder joints of these boards for improvement of reliability and manufacturability. These joints are typically in various geometric forms and sizes, and determination of their accurate geometries is extremely difficult. The purpose of this work is to integrate Four Pi X-ray laminography, Robotic Vision Systems, Inc. (RVSI) laser-vision, and image processing to construct a 3-D image of the joint for finite element modeling. The Four PI and RVSI are imaging systems that are designed for inspection of solder joints. Four PI is an x-ray system that provides cross-sectional images, while RVSI is a laser system that provides surface geometry. An automatic finite element mesh generation algorithm is implemented for surface mounted solder joints. The program generates a session file to be used in the commercial FE software package PATRAN.

The key to the success of this project centers around two main areas. The first area is in the ability to acquire accurate geometry data. The second area is the ability to produce accurate 3-D reconstruction. The type of solder joint inspection system used determines the accuracy of the geometry data. The developed algorithm determines the accuracy of 3-D reconstruction.

1.1 Solder Joint Inspection System

There are presently several different types of inspection systems, among them are: human, laser-vision, and x-ray. Human inspectors can no longer identify defects which will cause failure because of new technologies which include:

- Decrease in printed wiring components (less than 20 mils)
- Decrease in lead pitch (less than 20 mils)
- Solder joints are partly hidden by the component case
- Rapid growth in number of components per package

Also the visual inspection criteria may be too exclusive in the reliability requirement of a leadless surface mounted component according to a study by the ADSP/MANTECH program (Millard, 1989). From this study several evaluation parameters were determined to be inspection necessities:

- Investigating the interface composition
- Determining the location and volume of voids
- Assessing the mechanical reliability of the material
- Assessing the volume and geometry of the solder joint

The other inspection systems such as laser-vision and x-ray systems were developed to overcome the shortcomings of the visual inspection method.

1.1.1 Laser-Vision Systems

In laser-vision system, a laser is used to scan the solder and surrounding area. Several sensors detect the reflected light. The signals of the sensors are processed by a computer using geometrical triangulation to create a 3-D model. The system can provide the surface geometry of the joint, but it cannot investigate the interface composition, assess the mechanical reliability of the material, or determine the location and volume of voids.

1.1.2 X-Ray Systems

There are two different solder joint x-ray inspection methods. The first method, transmissive radiography, uses a fixed source and detector; the second method, laminography, uses a rotation source and a synchronized detector to create an image. This system can determine the geometry and the size of voids located within slices, however it cannot investigate the interface composition or assess the mechanical reliability of the material.

Table 1.1 shows a comparison of the different solder inspection systems. The task of the project is to produce a 3-D reconstruction. The capabilities of an inspection system to assess solder volume and geometry and locate voids are indispensable for an accurate 3-D reconstruction of a solder joint. Because the x-ray laminography is the only inspection system that can determine the location of voids in the joint, it was chosen for this project.

1.1.3 Solder Joints

The first laminography machine was patented in France in 1922. Laminography was used in medical imaging until it was replaced by Computer Tomography. Computer Tomography provided better contrast between materials with similar densities and lowered the patient's radiation dose required for imaging. Laminography technology returned to use in 1986 when Four Pi Systems Corporation pioneered work in Scanned-Beam Laminography (SBL). Laminography is best suited to planar objects with high density contrast. Since printed wiring boards (PWB) are planar objects and solder provides a sharp contrast, laminography is well suited for imaging solder joints.

Table 1.1 Summary of the evaluation parameters for the different solder joint inspection systems

Type of System	Assess Solder Volume and Geometry	Investigate Interface Composition	Determine Mechanical Reliability	Locate Voids
Laser-vision	Yes	No	No	No
X-Ray Laminography	Yes	No	No	Yes

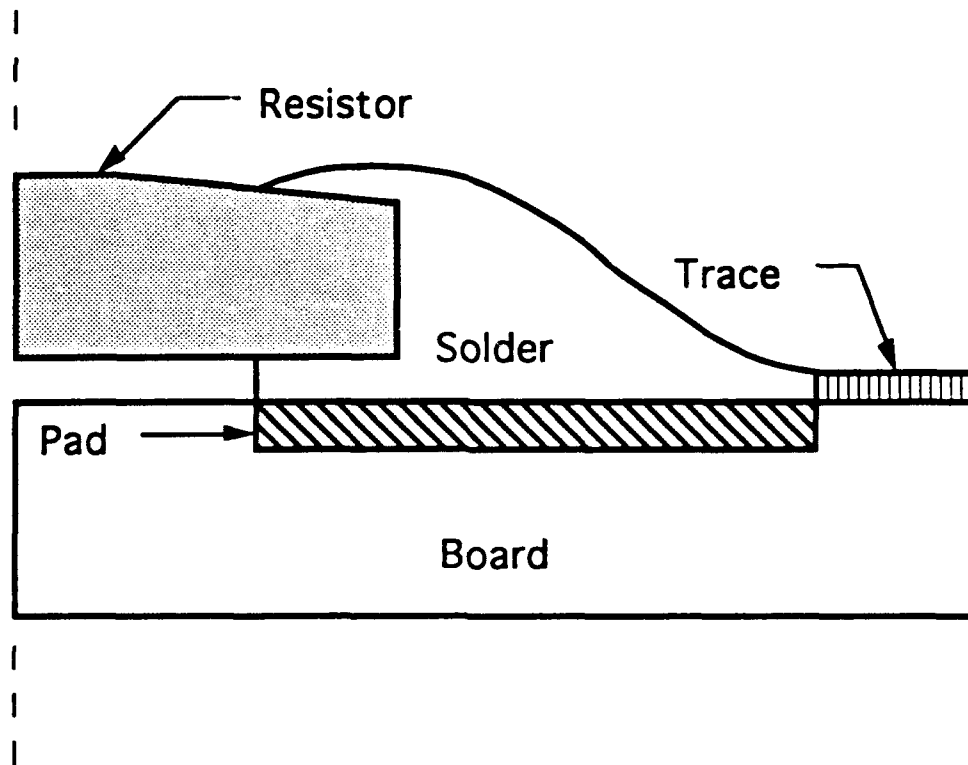


Figure 1.1 Surface-mount chip resistor

2. CREATION OF MESHES FROM FOUR PI SYSTEM

The first laminography machine was patented in France in 1922. Laminography was used in medical imaging until it was replaced by Computer Tomography. Computer Tomography provided better contrast between materials with similar densities and lowered the patient's radiation dose required for imaging. Laminography technology returned to use in 1986 when Four Pi Systems Corporation pioneered work in Scanned-Beam Laminography (SBL). Laminography is best suited to planar objects with high density contrast. Since printed wiring boards (PWB) are planar objects and solder provides a sharp contrast, laminography is well suited for imaging solder joints.

2.1 Four Pi and Its Characteristics

A laminograph is created by rotating the x-ray source and a synchronized detector as shown in Figure 2.1. The rotation produces a focal plane parallel to the x-y plane through which all the x-rays pass. The features of the object in the focal plane fall on the same location of the detector for any angle of rotation of the source, while features in other planes will appear in various locations on the detector. By integrating the image over a full rotation the features within the focal plane will contribute a constant intensity at the same location on the detector and thus on the final image. This same integration of the features outside the focal plane will produce a variable intensity over a greater area than the size of the object and thus will appear as a blur in the final image. Features located far from the focal plane will appear as a faint, very large blur in the final image, whereas features located closer to the focal plane will generate a smaller, greater intensity blur. Since the solder is one

solid mass (except for maybe some voids) contributions of features from very close to very far are introduced into the final image.

2.2 Procedure for Creating Geometry

The procedure used in automated generation of 3-D finite element computer meshes is shown in Figure 2.2. The flow of the problem solving stages is: solder joint, image acquisition, image processing, image segmentation, image recognition, image conversion, and session file preparation for the mesh generation program PATRAN. The image acquisition stage is done with Four Pi's 3DX Series 2000 Automated Digital Laminography System. The remaining stages are done from a FORTAN program. From the figure each step has an interaction with a knowledge base.

2.2.1 Knowledge Base

The knowledge base is information known about the object being imaged. This would include the size and orientation of the object. For the surface mounted resistor the knowledge base would include pad and resistor dimension and orientation of the solder joint. The standoff height of the solder will also have to be included in the knowledge base. The standoff height can be obtained from an external source for each solder joint or a value could be set for each pad and capacitor arrangement. Presently a RVSI laser vision system is the external source used to find the standoff height. One obvious disadvantage to an external source is that the solder joint must now be inspected by two different systems.

2.2.2 Image Acquisition

The laminographs can be obtained from two methods.

Method 1 - Automatic mode

- This mode is used in the inspection process of PWB.
- CAD data of the PWB, number of slices per solder joint, and location of slice with reference to the PWB is inputted into the Four Pi computers.
- This method demands the creation of several files before the inspection process can start.
- These files are time consuming to develop and are geared to provide information that is needed for the algorithms the company has written.

Method 2 - Manual mode

- In this mode the user moves the solder joint within the view of the video camera.
- The user positions the focal plane and triggers a laminograph to be taken.
- The user then saves the image into a file.
- A quick adjustment of the focal plane and the procedure is ready to be repeated.

We are presently using the manual mode. The image files are copied onto computer disks for transportation to the CAD/CAM laboratory where the files are copied to a Sun SPARC station 2. The FORTRAN program will start with the Four Pi images at the image processing stage and finish with the creation of a session file in the session file stage.

2.2.3 Image Processing

In the image processing step each slice is processed to enhance contrast and remove noise. Smoothing filters and sharpening filters are used in this stage. Smoothing filters are lowpass spatial and median filters, whereas sharpening filters are highpass spatial, high-boost, and derivative.

Sharpening filters are used to emphasize or locate edges. Smoothing filters are used to remove local distortions without removing larger features such as edges. But smoothing filters blur edges and other sharp details during operations. If the objective is to achieve noise reduction rather than blurring, an alternative approach is to use median filters. In the median filter the gray level of each pixel is replaced by the median of the gray level in a neighborhood of that pixel, instead of by the average. Several different 3X3 filters are listed in Table 2.1. A new image is created by replacing each pixel with a weighted average of the pixels in a surrounding NXN window.

Derivative filters use gradient values to find or sharpen edges. The Sobel operator and the Prewitt operator are common methods of estimation local gradients. These operators use a NXN window to estimate the partial derivatives in the x and y directions. Each operator consists of a pair of filters, one is for the x direction the other is for the y direction. Table 2.2 shows these two operators.

2.2.4 Image Segmentation

The image segmentation step partitions an input image into its constituent parts. Once the image processing is done a threshold value is applied to the data. Pixels above or equal to the threshold value are "on", those below are "off". The pixels that were "on" are now checked to see if they are part of the perimeter. A 3X3 window is looked at for each of these pixels. With the pixel of interest in the middle of the window, there are 8 neighboring pixels in the window. A search of the neighboring pixels is done to see if any of them are "on". If the number of neighboring pixels that are "on" are from 3 to 6 then the middle pixel is marked as part of the perimeter. Figure 2.3 shows the boundary found using the program. The scale on the right shows the 0 to 255 gray levels that are defined using the true color method in SunPHIGS 2.0 software. Gray level values are represented as different RGB triples.

2.2.5 Image Recognition

Image recognition step consists of three parts. The first part is to check if the boundary found in the previous step is reasonable. The second part is to select the best possible location for the pad from the first laminography. The third part is to correct image distortions. These distortions are directly related to the nature of laminography and the Four Pi Systems hardware used to produce the images. Two corrections are currently being used. The first is to correct for rounded corners. Rounded corners can be seen in Figure 2.3. The large straight line on the left is the boundary between the solder and the capacitor. The ends of this line show that the data is distorted by the rounding effect of the image taking method. The second correction is to provide a smooth boundary between the solder and the capacitor.

2.2.6 Image Conversion

The image conversion step has two parts. The first is the conversion of pixel data to inches. The image file produced by Four Pi assigns each pixel a row and column number. These numbers are used for the x and y local coordinate axes. But these numbers are in pixels and need to be converted to inches using the pixel dimension of 1 pixel equals 0.78125 mils. The second part is to write the component data into a session file.

2.3 Generation of a Session File

The finite element (FE) software package PATRAN is used in the automated generation of 3-D FE computer meshes. A session file is always produced as an output from a PATRAN execution. The session file is an exact copy of all input to the system from any source: keyboard, cursor, digitizer, and external files. The information is recorded in a card image format which can be edited or even created with a standard editor. A session file can be used to drive the system. This ability provides two major capabilities.

1. Model reconstruction from a session file.
2. Disaster recovery in case of error or equipment failure.

This project is directed at creating a session file. The session will be used in a variation of the first capability above. The solder joint will be constructed instead of reconstructed from the session file. The session file contains commands that will define geometric entities. Geometric entities - grids, lines, patches, and hyperpatches - are used to reconstruct a piecewise continuous representation of the solder joint geometry.

The session file is created from several steps. The program defines grid points as the pixels found to be the solder boundary. The grid points are divided into groups which will define lines. Two or more lines are then used to define patches. Two or more patches are used to define hyperpatches. Patches are comparable to a defined area, whereas hyperpatches are comparable to a defined volume. Once the grids, lines, patches, and hyperpatches are defined by the program, the program will write the appropriate command for the generation of the required item. A sample session file is shown in Appendix A.

2.4 Computer Program

The computer program is a modification of programs written by David Read (1991) of the Materials Reliability Division of the National Institute of Standards and Technology (NIST). Read's method for automated finite element mesh generation for SMT solder joints consist of three programs. The programs and their major functions are listed below:

DSH

- Reads in Four Pi raw data
- Averages rows to compensate for interlace problem
- Threshold and gradient methods to find perimeter

COMBINE

- Reverses data points
- Finds maximum and minimum values for each laminography
- Writes all data into a binary file

SLICE4P

- Reads file created in combine
- Finds average aspect ratio in the x-y plane
- Uses aspect ratio to help define the boundaries between hyperpatches
- Grids located on the boundaries are defined as end points of lines
- Lines are defined
- Patches are defined from four lines
- Hyperpatches are defined from patches on two different laminographs
- Arranges the defined entities (grids ,lines, patches, and hyperpatches) into a keyboard input format
- Writes formatted information into session file

2.4.1 Limitations of the Existing Program

Meshes produced from the existing program are not accurate representation of the solder joint images. The major factors that produce this problem are:

- Limited use of image processing
- One program designed to handle all SMT solder joints
- Does not use any known information of the object being imaged
- Does not adjust for distortions

2.4.2 Modifications of the Existing Program

The following modifications have been made to Read's (1991) program to remove some of the above disadvantages:

- Simplify three programs down to one program
- Use of different image processing techniques
- Subroutines developed to handle one type of SMT solder joint
- Program relies heavily on a knowledge base
- Program adjusts for some distortions
- Converts pixel coordinates to inch coordinates

In the development of the program three assumptions are made to facilitate the automated generation of computer meshes.

- The first assumption is that the solder completely covers the pad.
- The second assumption is that the capacitor is parallel to the pad.
- The third assumption is that the first slice is at the z distance of the standoff height

The program starts with reading the files produced from each laminograph and the distance from board level. The files are read in order of increasing distance from the PWB. The data is stored in a 3 dimensional array for processing. The pixel's columns and rows correspond to x and y values, respectively. These are the first two dimensions of the array. This defines a local x and y axes at the top left corner of the image. The third dimension of the array is the file number. Since each file is assigned a z value as the distance the laminograph was taken above the board, a local z axis is defined. These local axes are used in processing the data and in ultimately the 3-D generation of the object.

2.4.3 Boundary Finding Techniques

The boundary finding techniques are part of the image segmentation step shown in Figure 2.2. The program uses the threshold and gradient techniques from the existing program. The threshold method has been modified in the technique used to locate the solder perimeter.

2.5.3.1 Threshold Method

The threshold method works best with a bimodal gray level histogram. A image containing an object on a contrasting background produces a bimodal histogram (Figure 2.4). The dark gray pixels inside the image produce the rightmost peak in the histogram. The leftmost peak is due to the large number of light gray pixels in the background. Relatively few mid-gray pixels around the edge of the object produces the dip between the two peaks. A threshold gray level chosen in the area of the dip will produce a reasonable boundary for the object. When using the threshold method for image segmentation, all pixels at or above the threshold level are assigned to the object. The boundary is then that set of the pixels that has at least two neighbors outside the object. The area of the object defined by the gray level threshold T is given by

$$A = \int_T^{\infty} H(T) dD$$

Increasing the threshold level from T to T' causes only a slight decrease in the area.

2.5.3.2 Gradient Method

The gradient method uses the 3X3 Sobel operator (Table 2.2) to estimate local x and y gradients. But before this method can be used a gray scale calibration must be performed. The reason for this is that the gray level information for each pixel represents the brightness at that location, however this information does not correspond linearly to density. X-ray absorption is not linear, but is exponential, as shown in Figure 2.5. This curve is obtained from the gray scale values of 9 small solder disks located on the calibration board. The thickness of these disks are known and range from 1 to 22 mils. Changes in the pedestal gain and voltage gain of the camera alters the shape and position of the curve; therefore, a gray scale calibration must be done for each different camera settings.

After implementing gray scale calibration, the adjusted pixel values are used to find the local gradient values in the x and y directions. The gradient value for each pixel is found from

$$G^2 = G_x^2 + G_y^2$$

where G is the gradient value,
 G_x is the gradient value in the x direction,
 G_y is the gradient value in the y direction.

The integer value of the gradient results is then used to find the boundary. From this point on a method similar to the threshold method is used. A threshold value is set and all pixels equal to or greater than this value are segregated. These pixel are the solder boundary instead of the solder in the threshold method.

2.5 3-D Reconstruction Process

The heart of the reconstruction process starts after the boundary is determined and any distortions are corrected. The process includes the following steps:

- The program takes the boundary found from each slice and divides the data into two parts by finding a middle axis parallel to the long axis of the component as shown in Figure 2.6.
- The two data points that fall on the middle axis are flagged as the end points of lines.
- Next the maximum and minimum of the pixel location that define the boundary between solder and the component are flagged as end points of lines as shown in Figure 2.7.
- Two corners of the pad are used to locate the next two data points to be flagged. A search is made for the point on the boundary slice that is the minimum distance from each corner as shown in Figure 2.8.
- Figure 2.9 shows seven lines that are defined from the six flagged data points of each slice.
- Now two patches are defined from the seven lines.

- The above steps are repeated for each slice.
- Each group of two patches are matched up with two patches of a slice immediately above the slice to define a hyperpatch.
- This step is repeated for each slice except the last (top) slice.

Once the grids, lines, patches, and hyperpatches are defined by the program, the program will write into a file the commands needed for the generation of the required geometric entities.

Table 2.1 Typical 3X3 edge finding filters

Sobel operator			Prewitt operator		
-1	0	1	-1	0	1
-2	0	2	-1	0	1
-1	0	1	-1	0	1
-1	-2	-1	-1	-1	-1
0	0	0	0	0	0
1	2	1	1	1	1

Table 2.2 Gradient 3X3 edge finding filters

Horizontal edge enhancement	Vertical edge enhancement		Laplacian		
-1	-1	-1	-1	-1	-1
2	2	2	-1	8	-1
-1	-1	-1	-1	-1	-1
divide by 1	divide by 1		divide by 1		

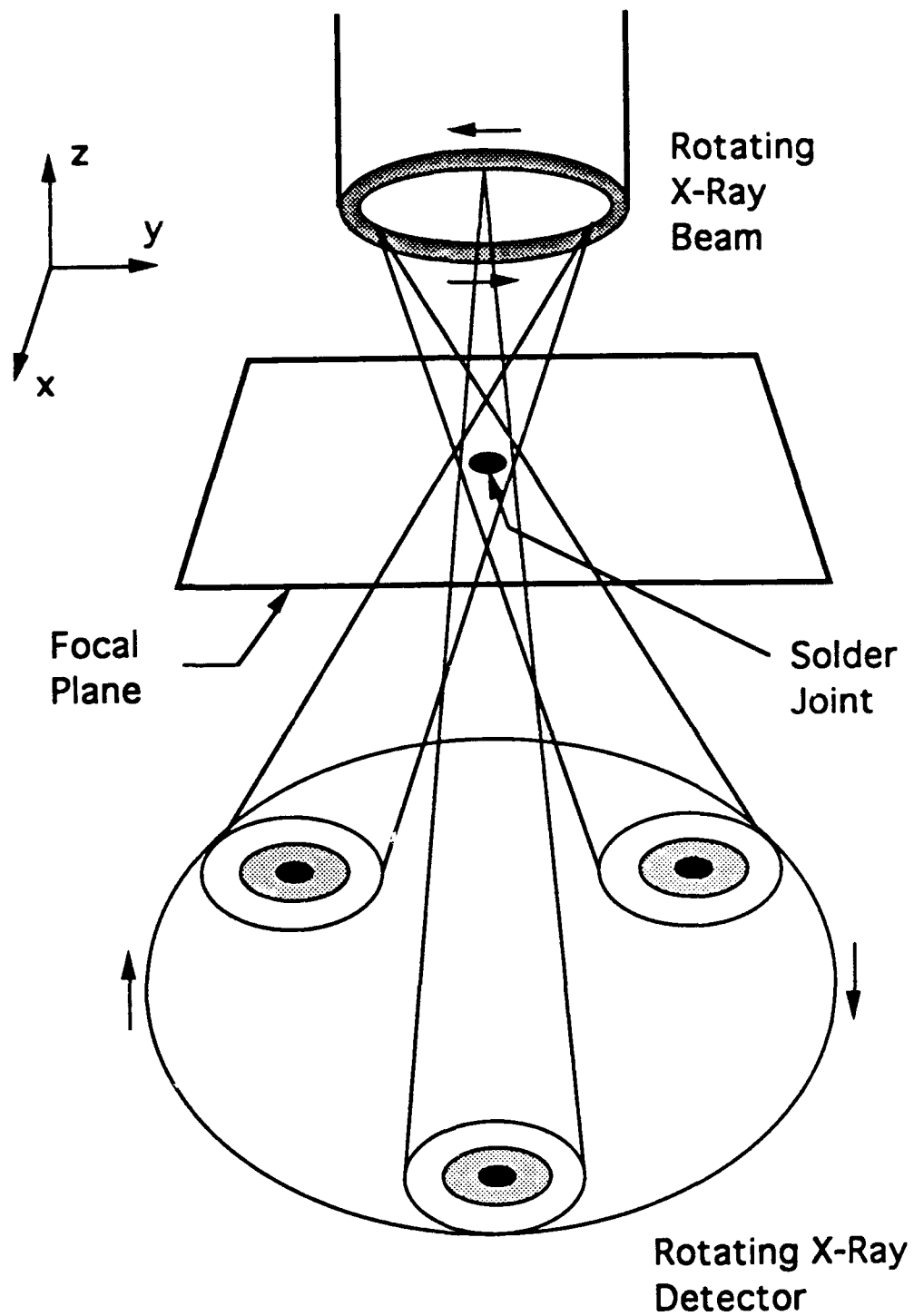


Figure 2.1 Scanned-beam laminography

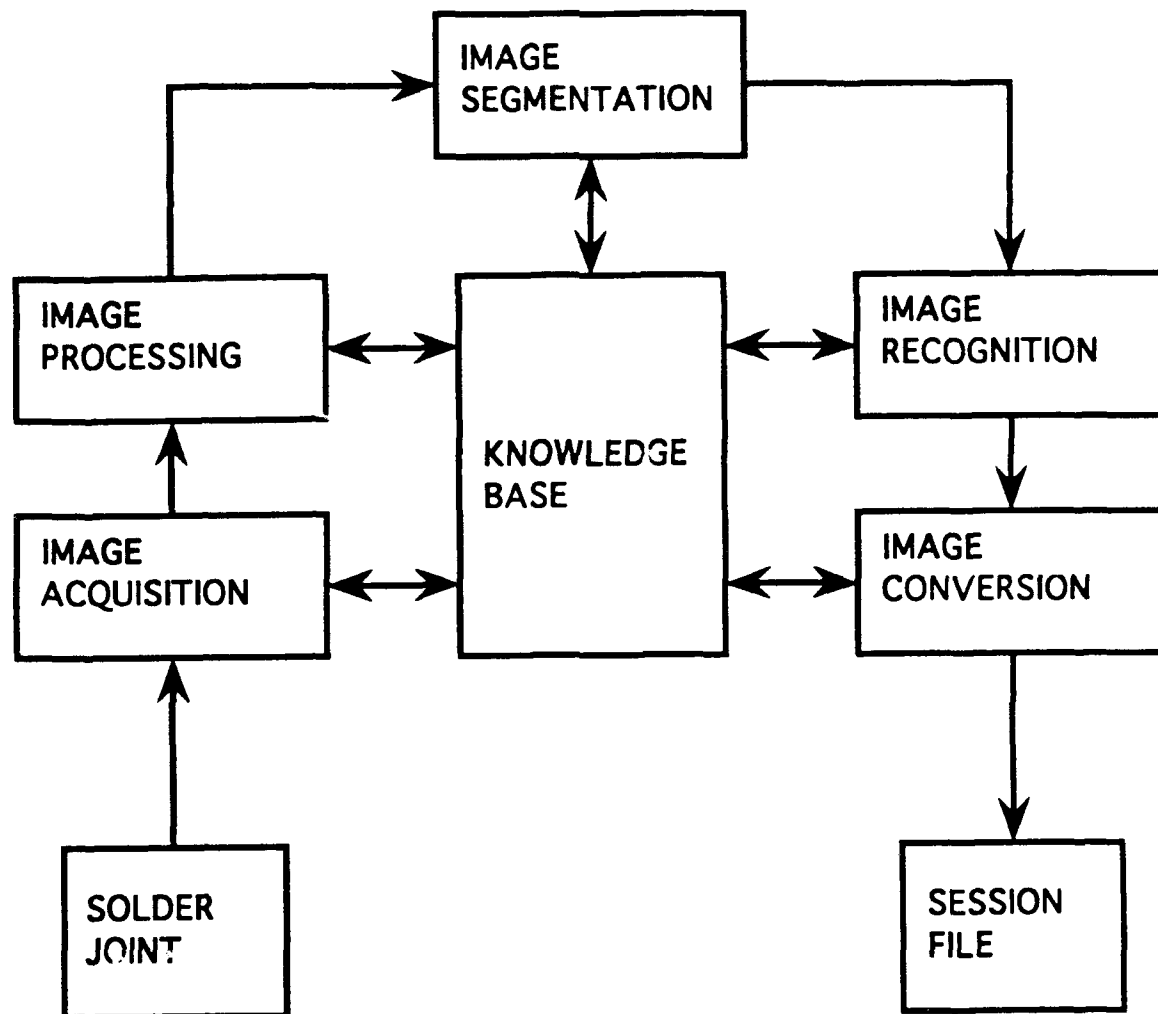
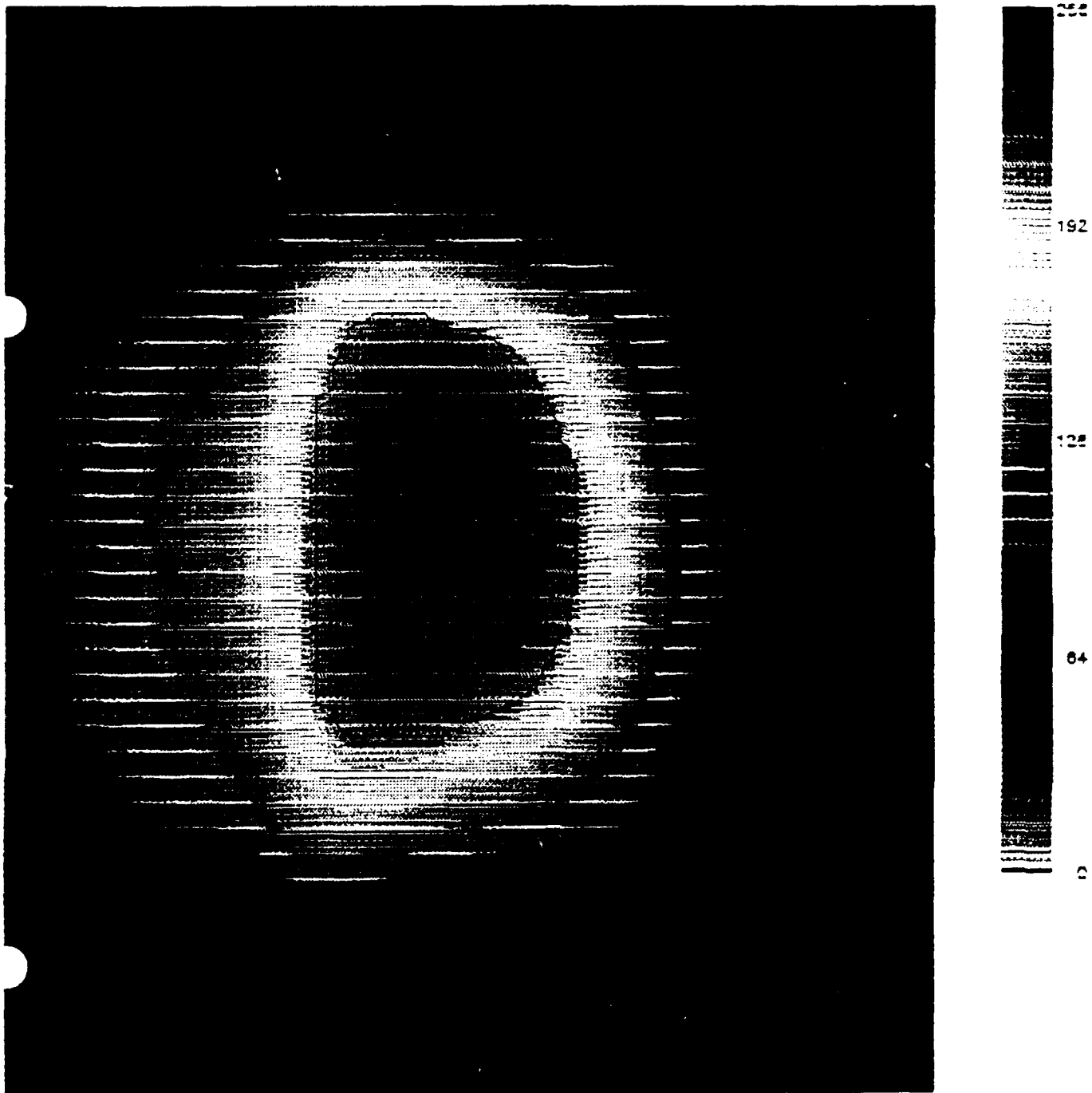


Figure 2.2 Four Pi problem solving flow chart

Figure 2.3 Typical laminography of a chip resistor



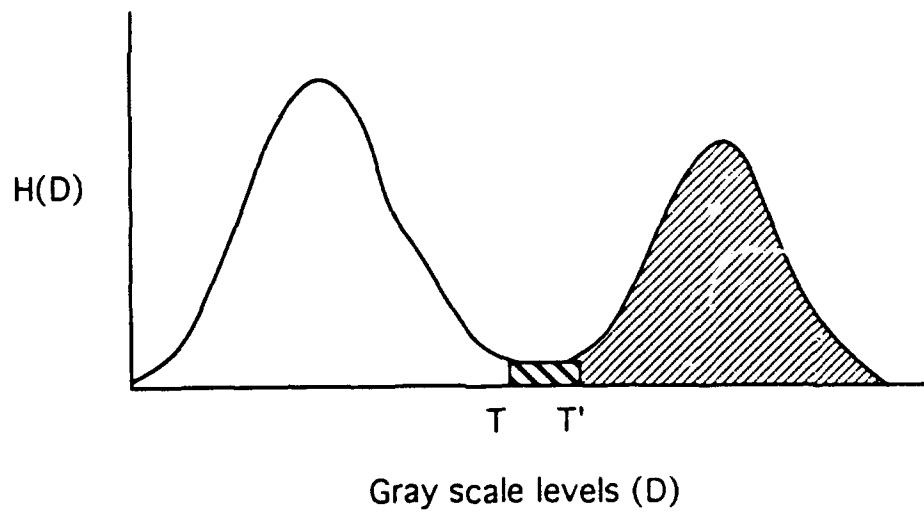


Figure 2.4 Bimodal gray level histogram

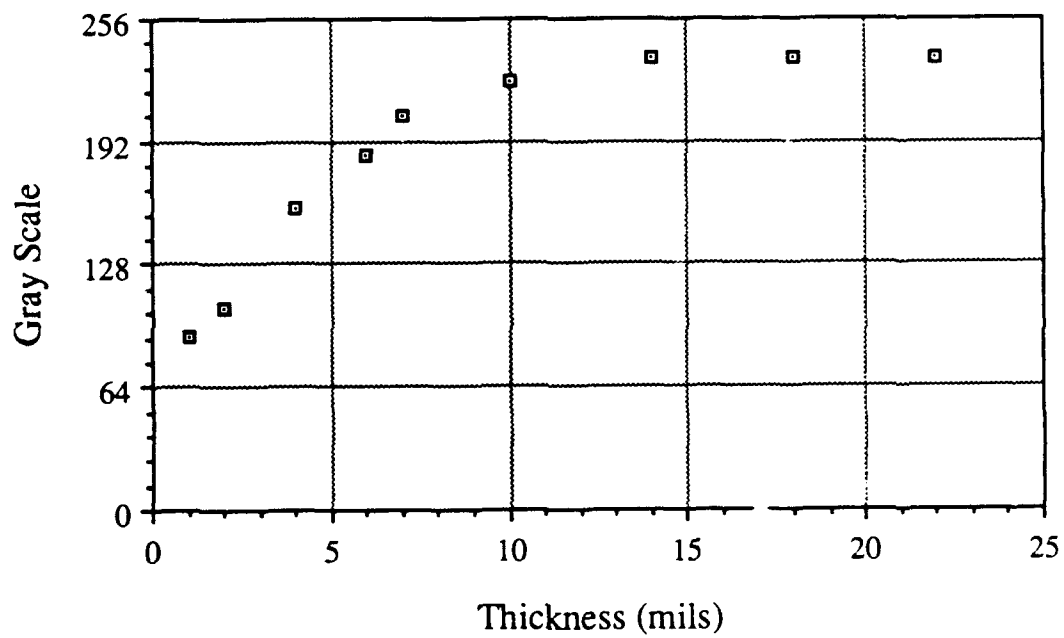


Figure 2.5 Thickness versus gray scale

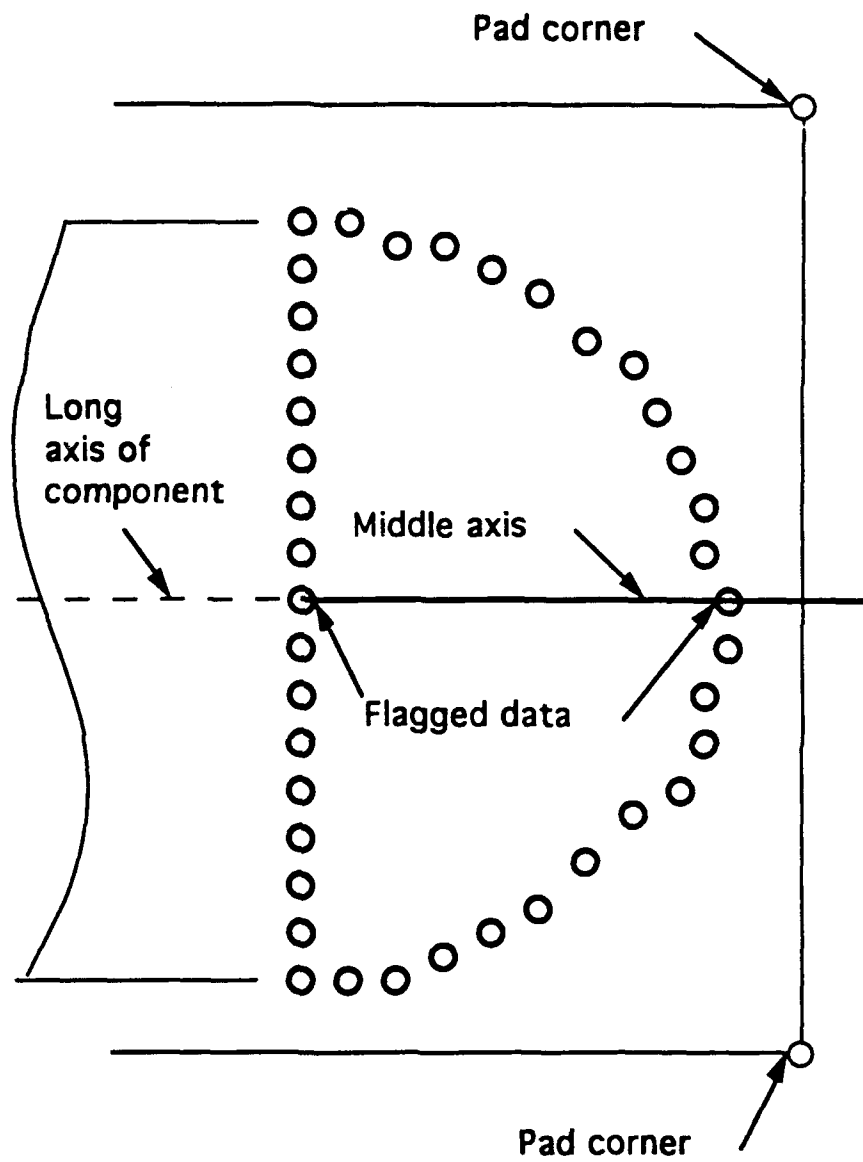


Figure 2.6 Flagging first pair of data points

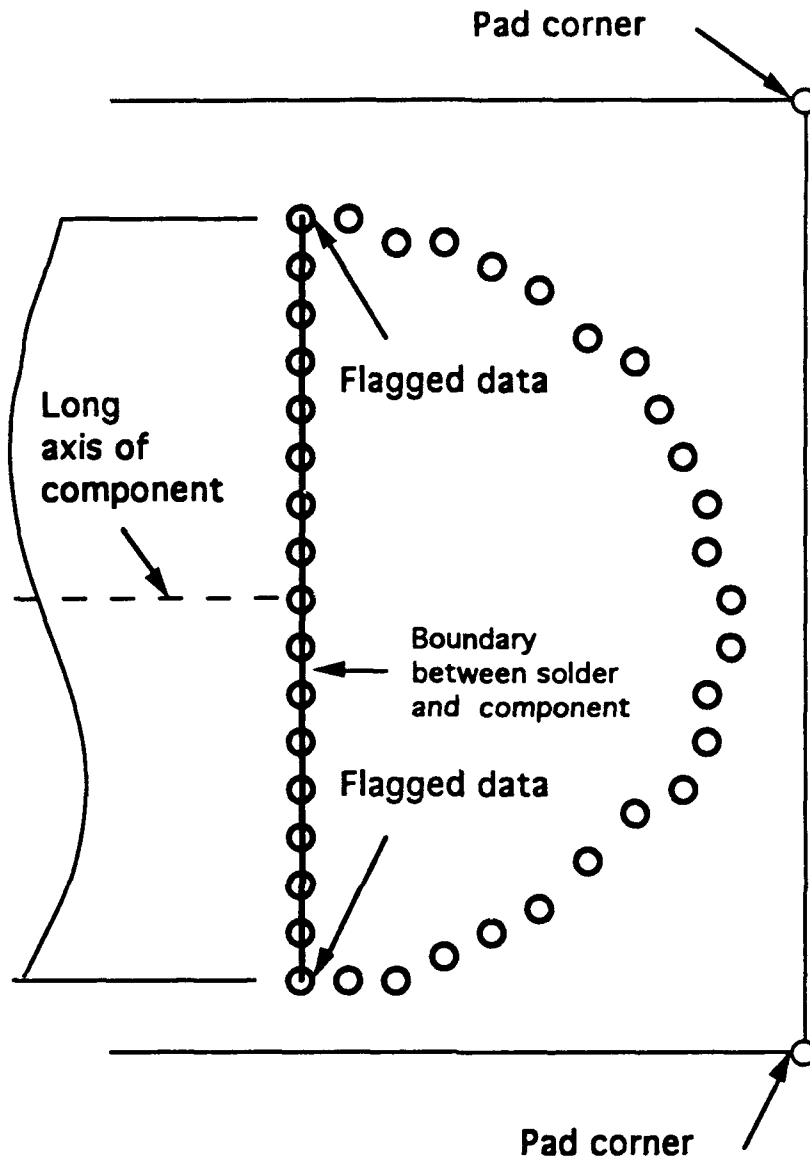


Figure 2.7 Flagging second pair of data points

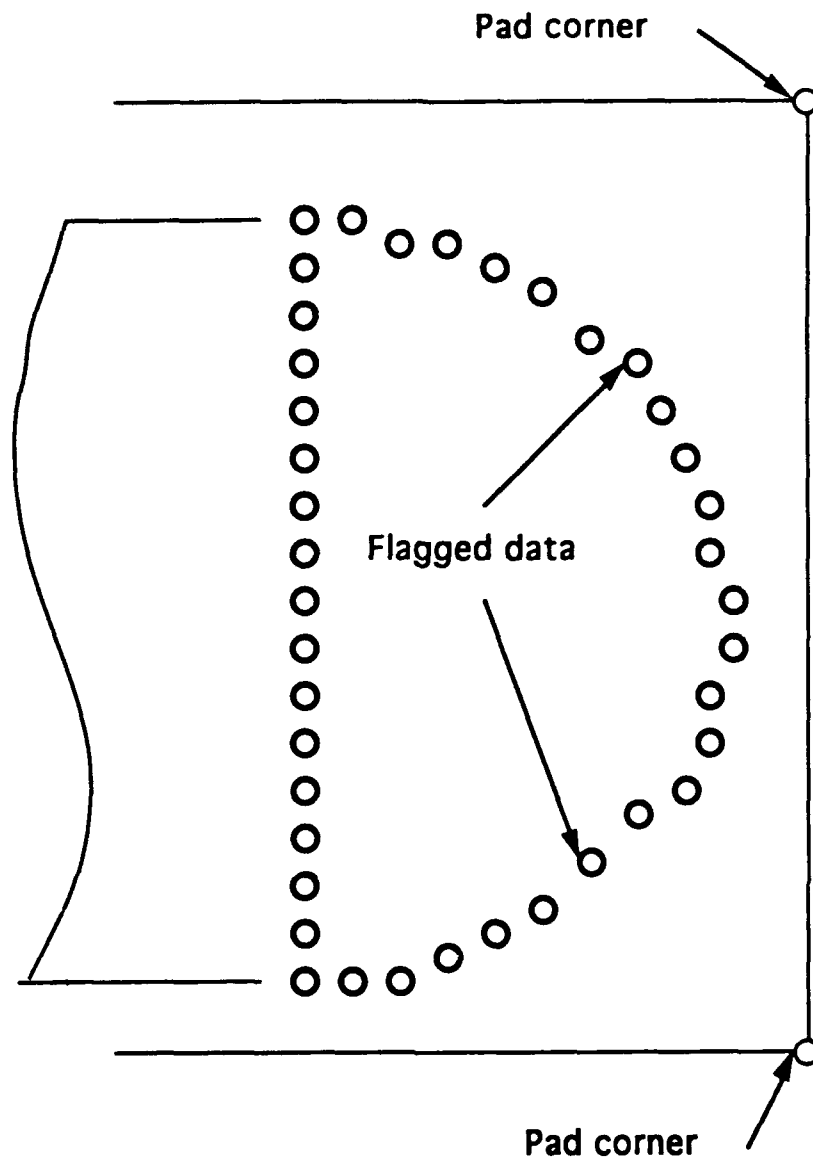


Figure 2.8 Flagging third pair of data points

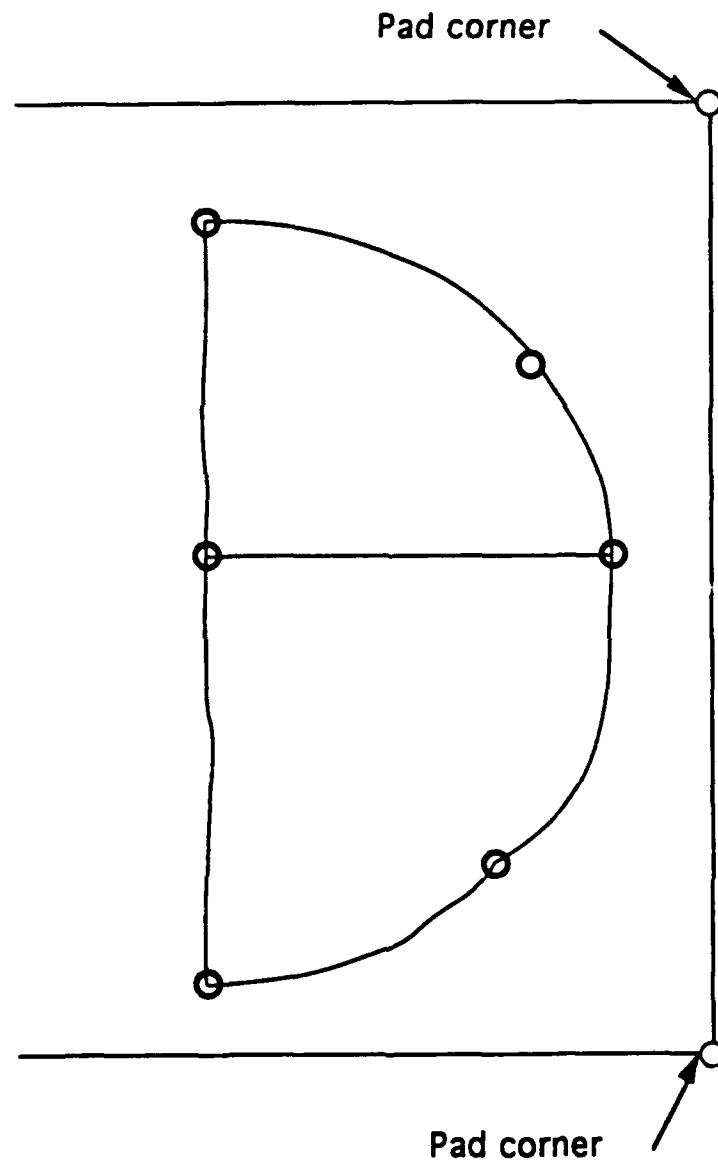


Figure 2.9 Defining seven lines between the six flagged data points

3. CREATION OF MESHES FROM RVSI SYSTEM

The machine used for the reflectance inspection system is the RVSI HR-2000. RVSI developed this system after it became involved with the US Navy Manufacturing Technology Program CCAPS (Circuit Card Assembly and Processing System) in 1986.

3.1 RVSI and Its Characteristics

This system uses a noncontact 3-D measurement - "structured light". The structured-light measurement technique consists of the projection of a known, controlled laser beam onto the solder joint. A solid-state camera is located at a known angle and distance from the projector. The camera captures the reflection of the laser beam projected onto the solder joint. The RVSI HR-2000 uses a proprietary optical triangulation 3-D vision system to produce a data set. The solder joint's 3-D geometry is mathematically described in the data set by thousands of independent x,y,z surface measurement points.

3.2 Procedure for Creating Geometry

The procedure for creating geometry with the RVSI (Figure 3.1) is a modification of the procedure used with the Four Pi Laminography system as shown in Figure 2.4. The flow of the problem solving stages is: solder joint, image acquisition, image processing, image segmentation, and session file preparation for the mesh generation program PATRAN.

We have divided solder joints into two classifications based on geometric characteristics. This is needed because different amounts of solder require

different approaches in the subdivision of the solder joint constituents (i.e., solder, board, resistor). The two classifications are defined as whether or not the solder covers the top of the resistor. Figure 3.2 shows solder that covers the top of the resistor, which will be called type A joint. Figure 3.3 shows solder that does not cover the top of the resistor, which will be called type B joint.

The proper subdivisions of the solder constituents are critical in the development of computer meshes. The geometric entities (patches for 2-D, hyperpatches for 3-D) must be defined in such a manner that ensures there are no mesh interface problems between any of the subregions. The solder in a type A joint is divided into ten subregions as shown in Figure 3.2. The top view shows that the solder joint is divided into halves. The center line is found by locating the position of the trace. The side view shows that each half is then divided into five subregions. The solder in a type B joint is divided into six subregions as shown in Figure 3.3. Again the solder is divided into halves. Since the solder fails to cover the top of the resistor the top two subregions for each half are not needed. The differences in the types of joints will require two separate approaches in the subdivision of the resistor to ensure a proper interface between resistor subregion meshes and adjacent solder subregion meshes.

The program was written for the type A joint. Some separate subroutines will have to be written to process a type B joint. The procedures defining the bottom two subregions on each half will be the same for both solder types.

3.2.1 Knowledge Base

The knowledge base information is the same information used for the Four Pi Laminography method except for the standoff height. The RVSI laser vision system determines the standoff height from the thickness of the resistor subtracted from the measured top of the resistor. The thickness of the resistor comes from the manufacture's design specifications, as shown in Figure 3.4.

3.2.2 Image Acquisition

Figure 3.5 shows the data set output of the image acquisition stage. The data set is a high resolution geometric map of the solder joint along with the surrounding resistor and board. The amount of surrounding area included is programmed manually or directly from CAD downloading prior to imaging.

The measurement points are stored within a file as x, y, z coordinates and a slice number. A slice is a scan of data points having approximately the same y value. Table 3.1 shows that each scan's data points are listed in increasing x values.

3.2.3 Image Processing

The image processing stage consist of methods to process the data points. One of the methods used is to average the y value within each slice and then replace the y coordinate with that slice's average value. A second method is the generation of data points in area where there are missing data points. The third method is averaging the x and z values of the data points before and after a data point. This is done for each point within the slice then these averaged x and z coordinates are used to replace the x and z coordinates of the middle data point. The third method is show in Figures 3.6 and 3.7. The x and z coordinates for points one and three are averaged and stored an array. The procedure moves down the file to the next data point. Point three of the previous step is now point two. Later the averaged point values replace their corresponding raw data points. Figure 3.7 shows the smoothed data points as a result of using this method.

The third method is used to smooth the data points because of the variation of the y coordinates within a slice. Table 3.1 shows the center portion of a slice. In each slice the y coordinates may vary by up to 1 mil between data points. The major problem is at the center of the scan where a large jump (1.0 to 2.5

mils) occurs in the y coordinates. In the table the jump occurs between an x value of 10.5987 and 10.6003. The magnitude of this jump is 2.3 mils.

3.2.4 Image Segmentation

Image segmentation will use knowledge base information to help locate the pad and component boundaries and then selectively removing data points outside of these boundaries. Next the program divides the data points to fit into subregions as shown in Figure 3.2. Lines are fit on these subregional data points for each slice. Patch and then hyperpatches are then generated. The same method used with Four Pi defines geometric entities and then writes this information into a session file.

3.3 Generation of a Session File

RVSI laser-vision system measures the locations of points on the surface of a SMT solder joint and its joining chip resistor. A typical data supplied by RVSI included over 5500 data points arranged in 85 slices. The data were listed as integers in which one unit represented 10^{-4} in (i.e., 2.54 mm). The slices were separated by about 15 original integer units (i.e., 38 mm) in the local y-direction. *Each slice was an open curve of data points running up one side of solder, across the top, down the other side.* Figure 3.8 shows the grid points of slice 34 of the joint imaged by laser vision.

The following procedure were used to generate PATRAN session file from the surface points of RVSI laser-vision.

The data from RVSI was read by a FORTRAN program. For each slice, the program records all the points above the solder pad, closes the open curve of each slice by adding new grid points along the interface between solder joint and solder pad. Figure 3.9 shows the closed curve of slice 34. The average y coordinate of each slice was calculated and was assign to every point in this

slice (since the original data points do not have constant y coordinate in the same slice). Also, it converts unit from ' 10^{-4} in' to 'mm'. All the grid points were then stored in a session file preparation for the mesh generation program PATRAN.

The following two methods were used to generate finite element meshes from grid points of the session file using PATRAN pre-processing. In Method 1, as shown in Figure 3.10, the vertical cross sections are created first. These sections are then connected to each other to create the solid model of the joint. In Method 2, as shown in Figure 3.11, the outer surface of the solder joint is created first, followed by filling the interior to create the solid model.

The steps followed in these two methods are illustrated below.

Method 1. Hyperpatches from cross-sectional patches.

For each slice, lines are fitted and drawn to the grid points, as shown in Figure 3.12. Edge patches, defined by lines on all four sides, are drawn and blended as shown in Figure 3.13. Two-patch hyperpatches are defined between pairs of patches on adjacent slices, as shown in Figure 3.14. All the hyperpatches are blended in order to smooth the model. The hyperpatches are then filled with eight-noded finite elements, as shown in Figure 3.15. Figure 3.16 shows the solid model of the assemble created by Method 1.

Method 2. Hyperpatches from surface patches.

For each slice, lines are fitted and drawn to the grid points. In order to make the lines smooth and without losing its original shape, the curve of each slice is divided into five sections. Lines are then fitted and drawn to the grid points along each section. Three lines at upper level are merged as one curve, it is then broken into two lines in the middle point, these two lines are blended with the bottom two lines in order to keep the model smooth. Additional lines are created to connect the joining point of the lines for the purpose of generating patches later. Between two adjacent slices, lines are also created to connect the corresponding grids which join the lines in order to generate surface patches later. Figure 3.17 shows the lines between slices 34 and 36 of the solder joint imaged by laser vision. Four edge patches at upper level and three two-line patches at lower level are generated between two slice, as

shown in Figure 3.18. The patches on the surface are then blended. Two-patch hyperpatches are defined. The two on the top are made by upper-lower patches, while the two on the bottom are made by left-right patches, as shown in Figure 3.19. The hyperpatches at the joining area between solder joint and the chip resistor and behind the joining area were generated from cross-sectional patches, as it was described in the Method 1. The hyperpatches are then filled with eight-noded brick finite elements, as shown in Figure 3.20. Figure 3.21 shows the solid model of the assembly created by Method 2.

As may be observed from the comparison of Figures 3.15 and 3.20, Method 2 tends to yield smoother surface, although it is more difficult to automate. This is also concluded by comparison Figures 3.16 and 3.21.

Table 3.1 Portion of RVSI HR-2000 data slice

X inch	Y inch	Z inch	Slice Number
10.5902	10.1686	2.4537	60
10.5913	10.1683	2.4540	60
10.5931	10.1685	2.4538	60
10.5945	10.1685	2.4538	60
10.5957	10.1683	2.4540	60
10.5972	10.1683	2.4540	60
10.5987	10.1685	2.4538	60
10.6003	10.1708	2.4543	60
10.6020	10.1708	2.4545	60
10.6036	10.1708	2.4547	60
10.6051	10.1707	2.4545	60
10.6066	10.1707	2.4545	60
10.6080	10.1707	2.4545	60
10.6092	10.1708	2.4545	60

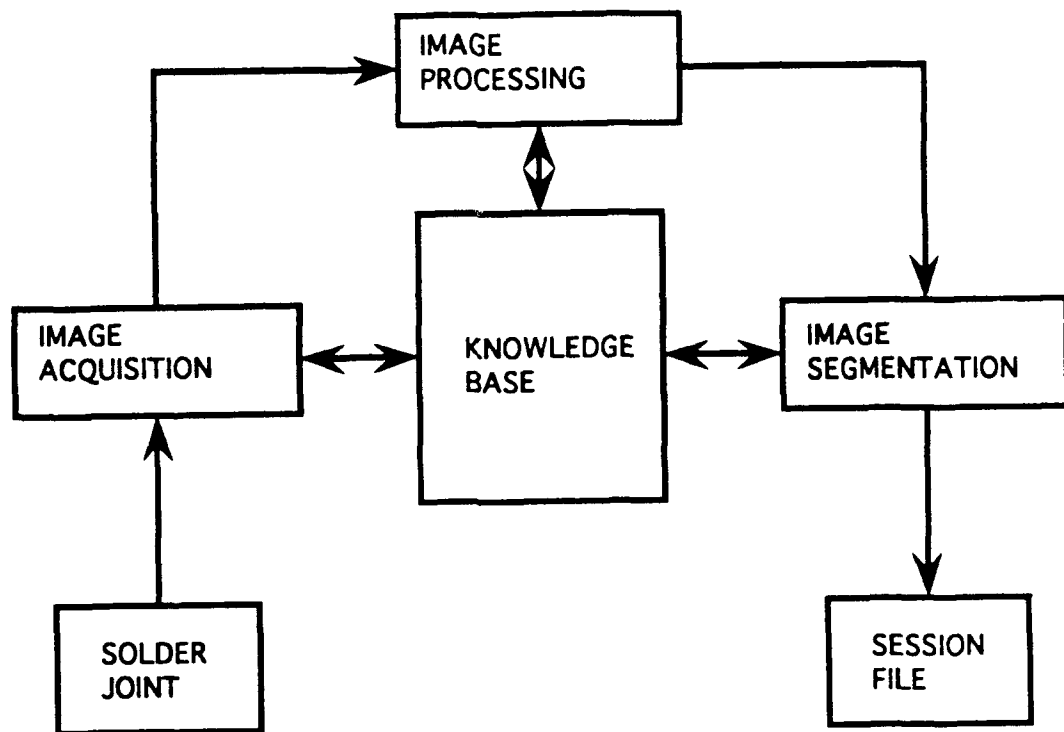
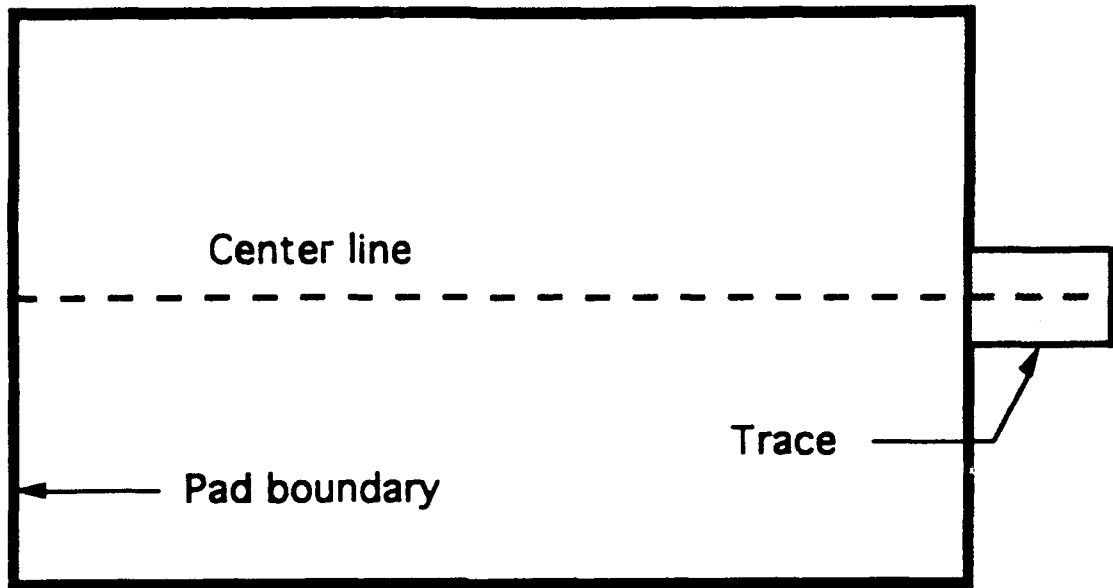
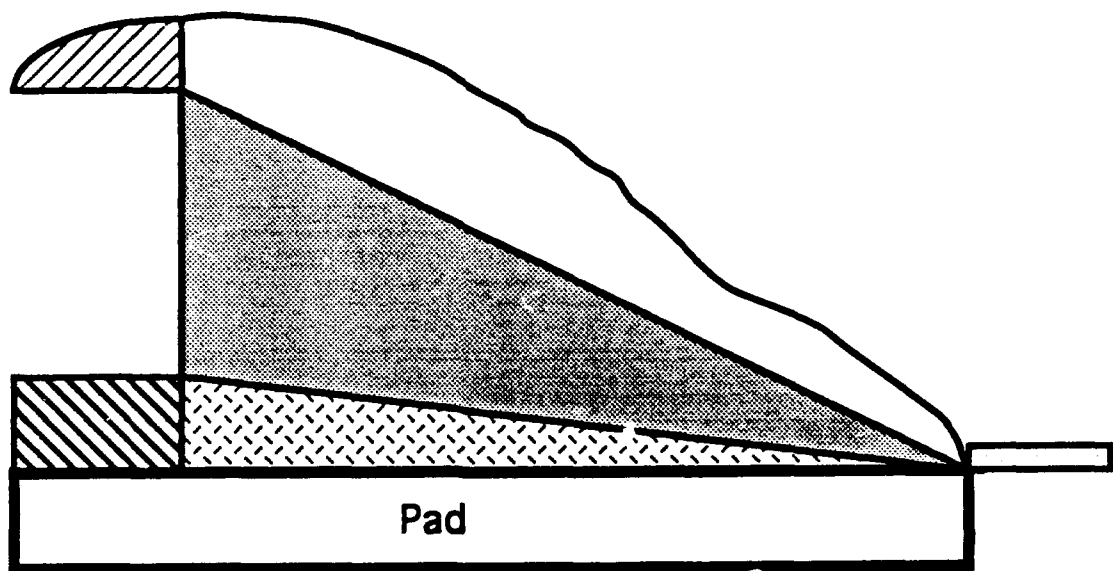


Figure 3.1 RVSI problem solving flow chart

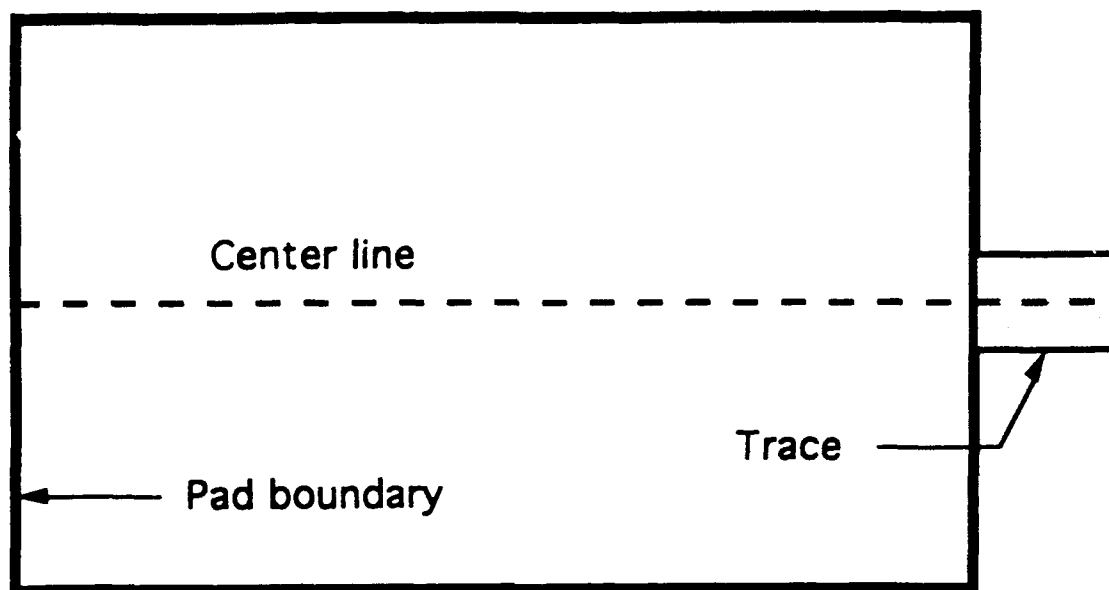


(a) Top view

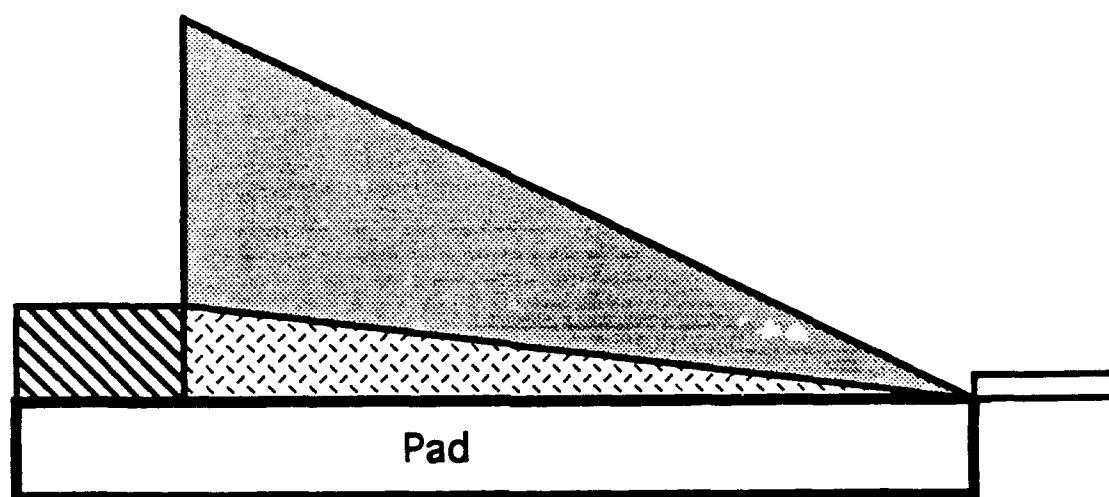


(b) Bottom view

Figure 3.2 Type A joint

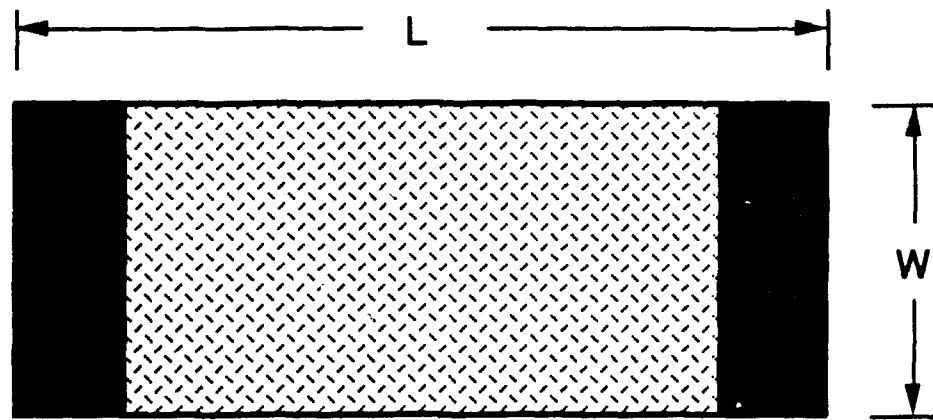


(a) Top view

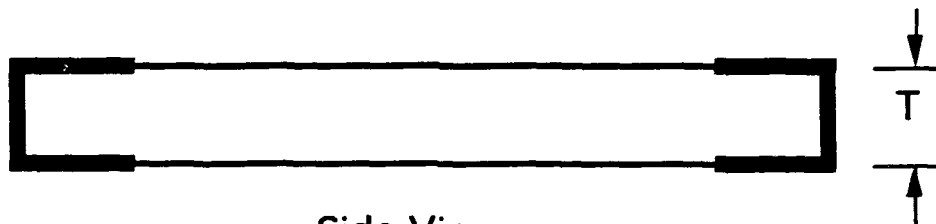


(b) Bottom view

Figure 3.3 Type B joint



Top View



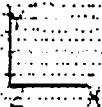
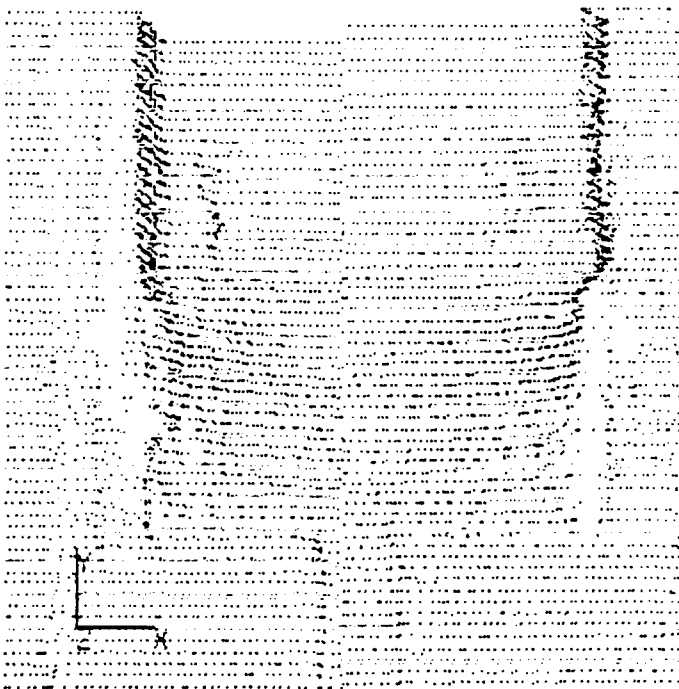
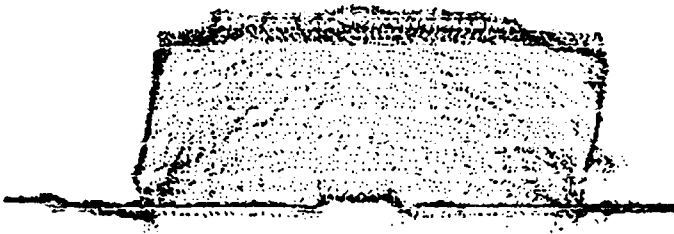
Side View

Dimension of Chip Resistor
(Inches)

Size Code	Length (L)	Width (W)	Thickness (T)
1206	$.126 \pm .008$	$.060 \pm .008$.020

Figure 3.4 Manufacture's design specifications of the chip resistor

COMMAND NAME DISPLAY ACTIVE WINDOW VIEW GET/SHOW PLOT



5. INTERFACE 6. STOP 7. PDA PCL 8. USER MENU

ET MENU

"MENU" IS NOW ON

Figure 3.5 Output data points from RVSI HR-2000

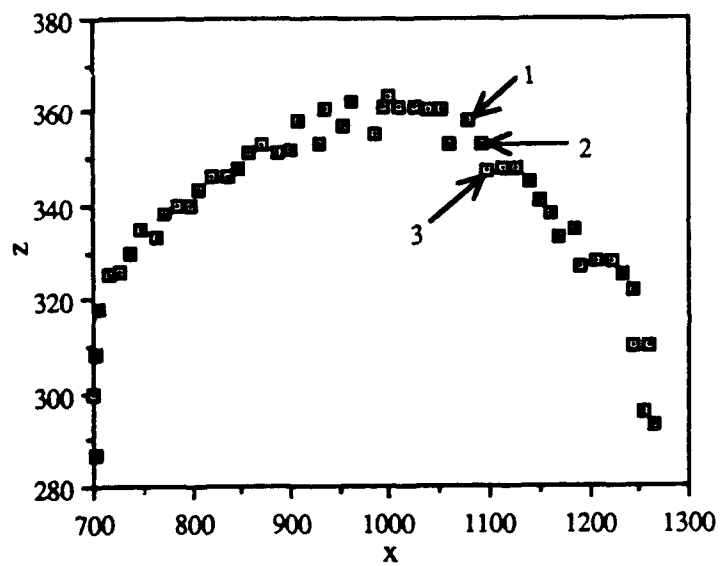


Figure 3.6 Raw data from slice 26

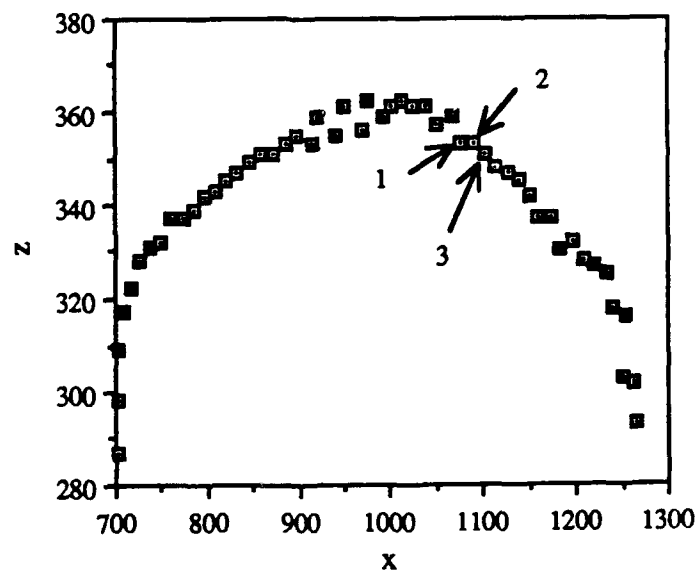
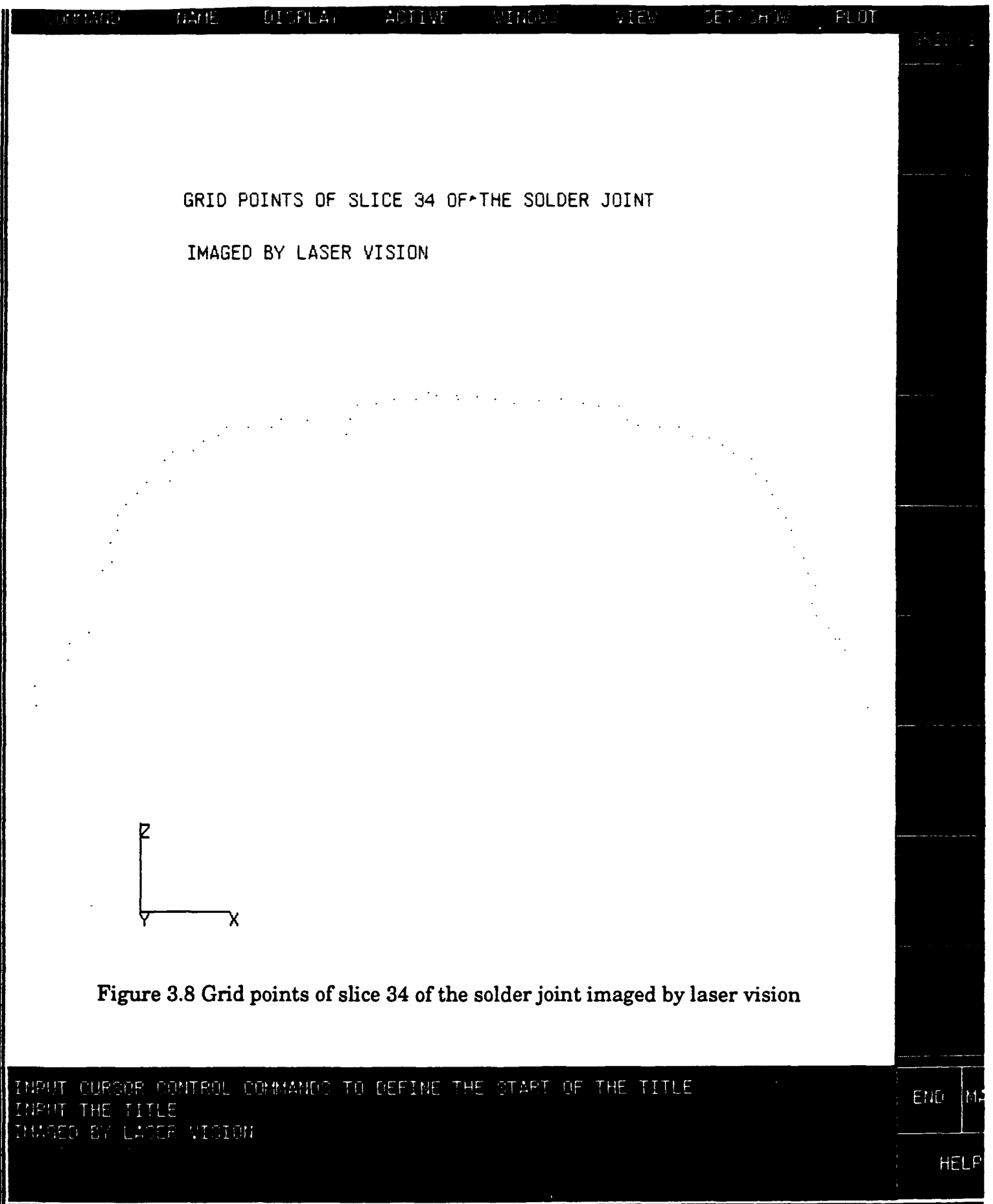


Figure 3.7 Averaged data from slice 26



COMMAND NAME DISPLAY ACTIVE WINDOW VIEW SET SHOW PRINT

CLOSED CURVE OF SLICE 34

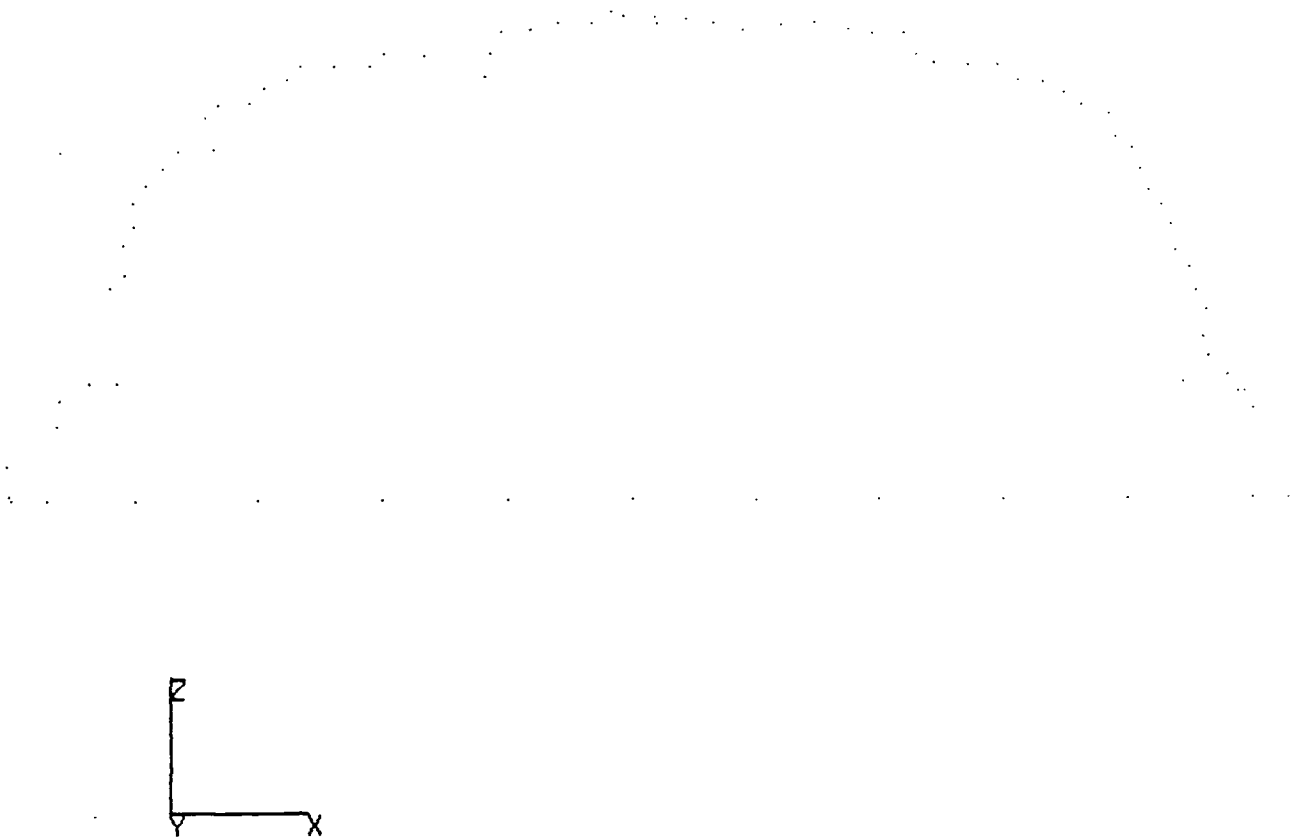


Figure 3.9 Closed curve of slice 34

INPUT CURSOR CONTROL COMMANDS TO DEFINE THE START OF THE TITLE
INPUT THE TITLE
CLOSED CURVE OF SLICE 34

END

HE

COMMAND	NAME	DISPLAY	ACTIVE	WINDOW	VIEW	GET/SHOW	PLOT	MODE
---------	------	---------	--------	--------	------	----------	------	------

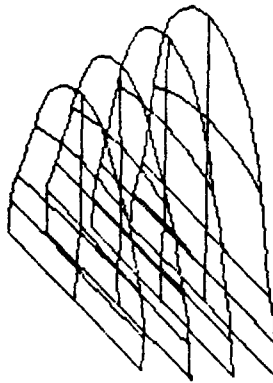


Figure 3.10 Method 1 (Hyperpatches from cross-sectional patches)

```

CHOOSE ANY OPTION
INPUT MAGNIFICATION POWER FOR SCREEN 1
0.5

```

GEOME

ANALY
MODEL

ANALY

RESUL

INTER

STOP

POA_P

USER_

END

HE

FORMAT NAME DISPLAY ACTIVE WINDOW VIEW SET COLOR PLOT

EDGE

4-ED

BPED

ELEF

FILL

MAT

WHO

CHO

MOF

EN

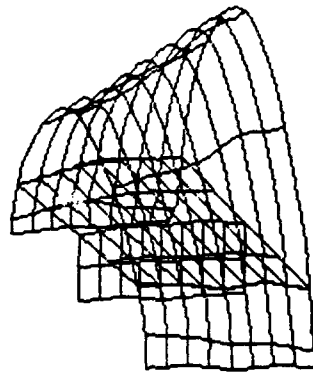


Figure 3.11 Method 2 (Hyperpatches from surface patches)

CHOOSE ANY OPTION
INPUT MAGNIFICATION POWER FOR SCREEN 1
0.5

COMMAND	NAME	DISPLAY	ACTIVE	WINDOW	VIEW	SET SHOW	PLOT
---------	------	---------	--------	--------	------	----------	------

LINES FITTED AND DRAWN TO THE GRID POINTS IN SLICE 34 OF
 THE SOLDER JOINT IMAGED BY LASER VISION

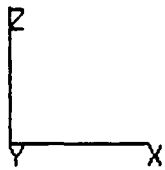
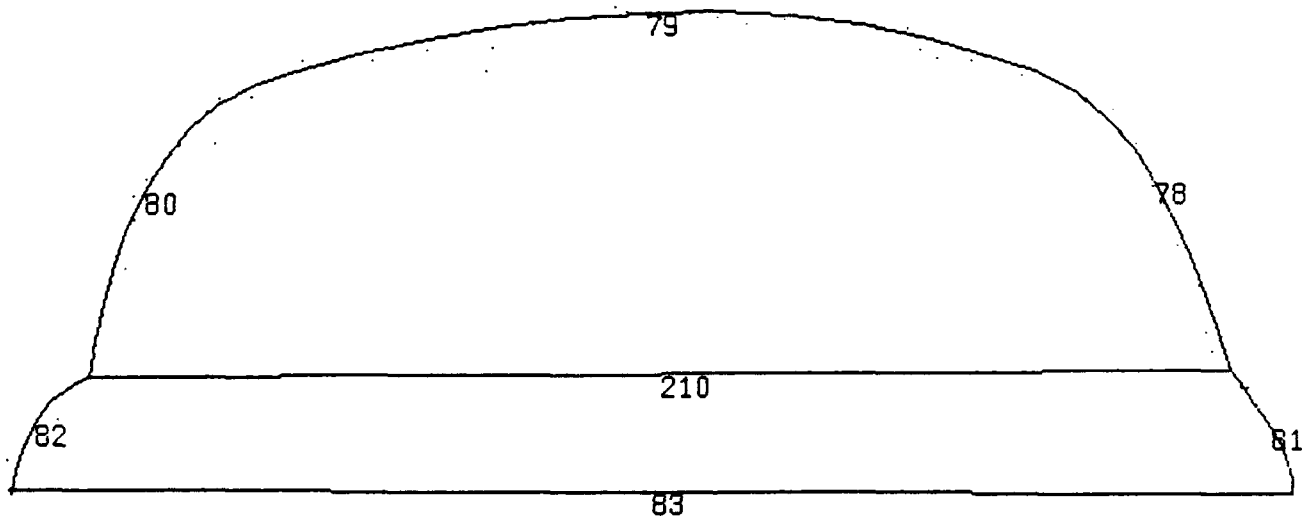


Figure 3.12 Lines fitted and drawn to the grid points (method 1)

INPUT CURSOR CONTROL COMMANDS TO DEFINE THE START OF THE TITLE
 INPUT THE TITLE
 THE SOLDER JOINT IMAGED BY LASER VISION

END MA

HELP

COMMAND	NAME	DISPLAY	ACTIVE	WINDOW	VIEW	DETAILS	PLOT
---------	------	---------	--------	--------	------	---------	------

EDGE PATCHES DEFINED BY THE LINES ON SLICE 34 OF
THE SOLDER JOINT IMAGED BY LASER VISION

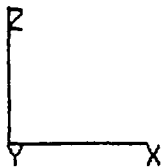
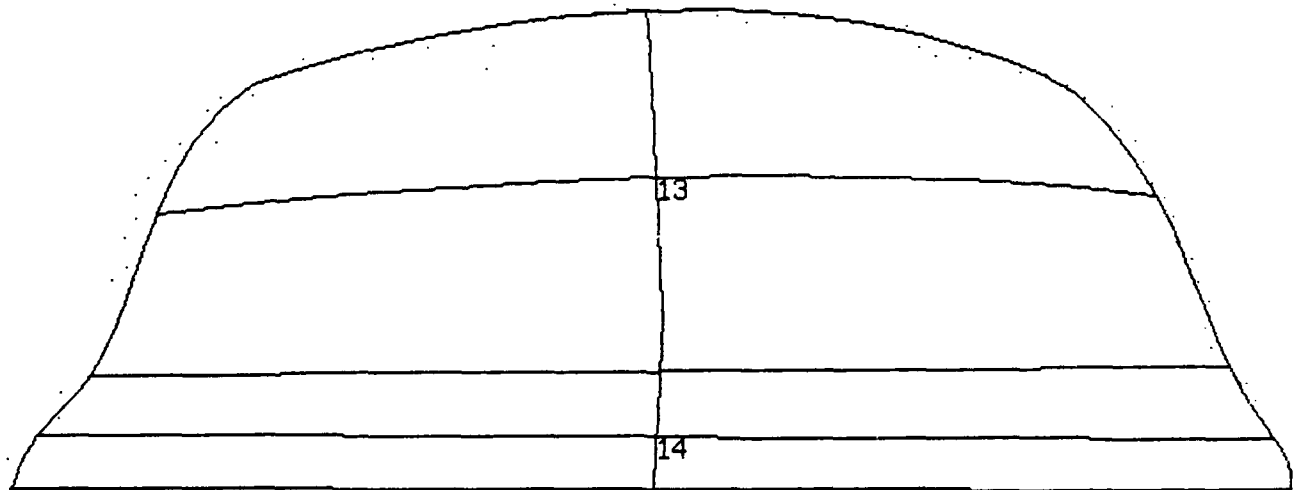


Figure 3.13 Edge patches defined by the lines (method 1)

INPUT CURSOR CONTROL COMMANDS TO DEFINE THE START OF THE TITLE
INPUT THE TITLE
THE SOLDER JOINT IMAGED BY LASER VISION

END

H

COMMAND NAME DISPLAY ACTIVE WINDOW VIEW LET:SHOW PLOT

HYPERPATCHES DEFINED BETWEEN PAIRS OF PATCHES
ON ADJACENT SLICES

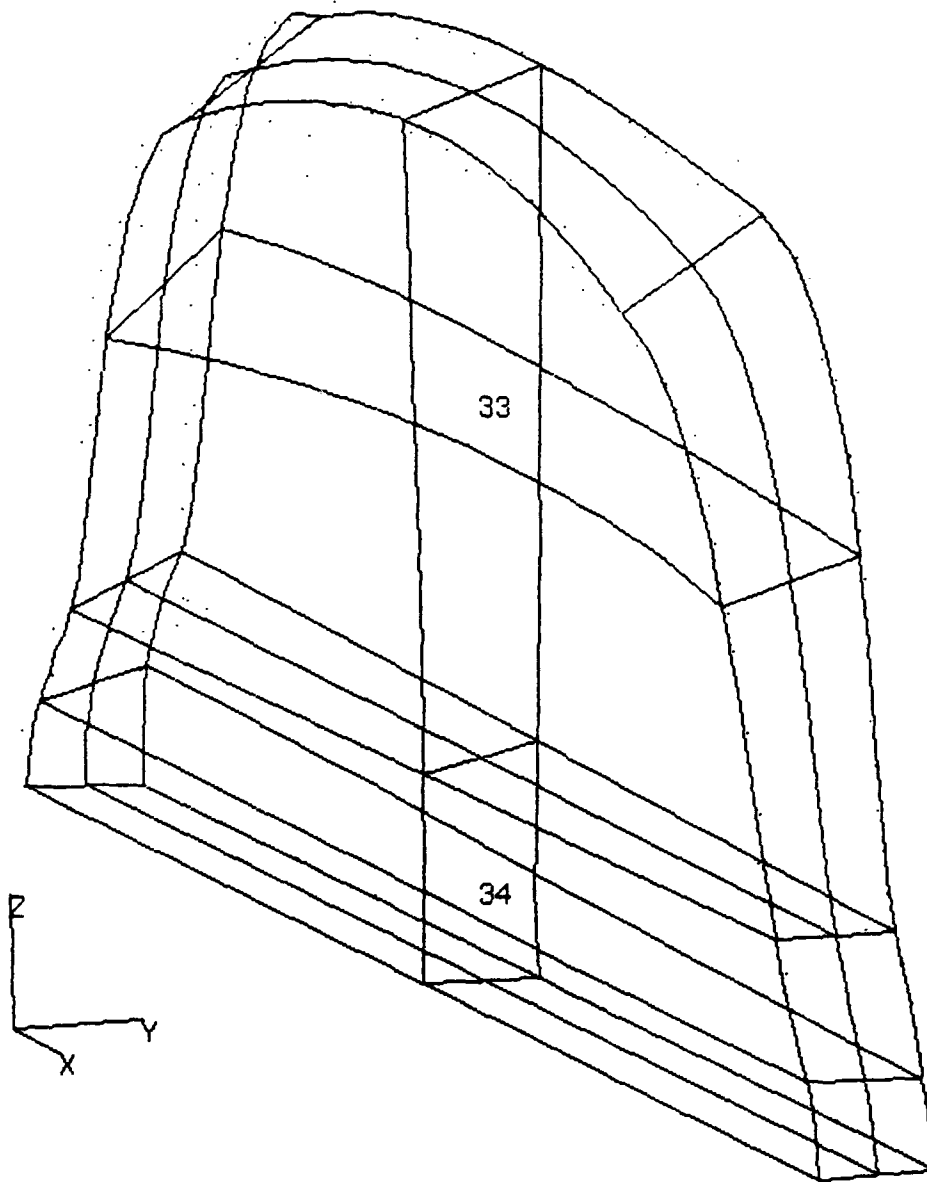


Figure 3.14 Hyperpatches defined between two patches (method 1)

INPUT CURSOR CONTROL COMMANDS TO DEFINE THE START OF THE TITLE
INPUT THE TITLE
ON ADJACENT SLICES

END MA

HELP

COMMAND	NAME	DISPLAY	ACTIVE	WINDOW	VIEW	DETAILS	PLOT
---------	------	---------	--------	--------	------	---------	------

FINITE ELEMENT MESH

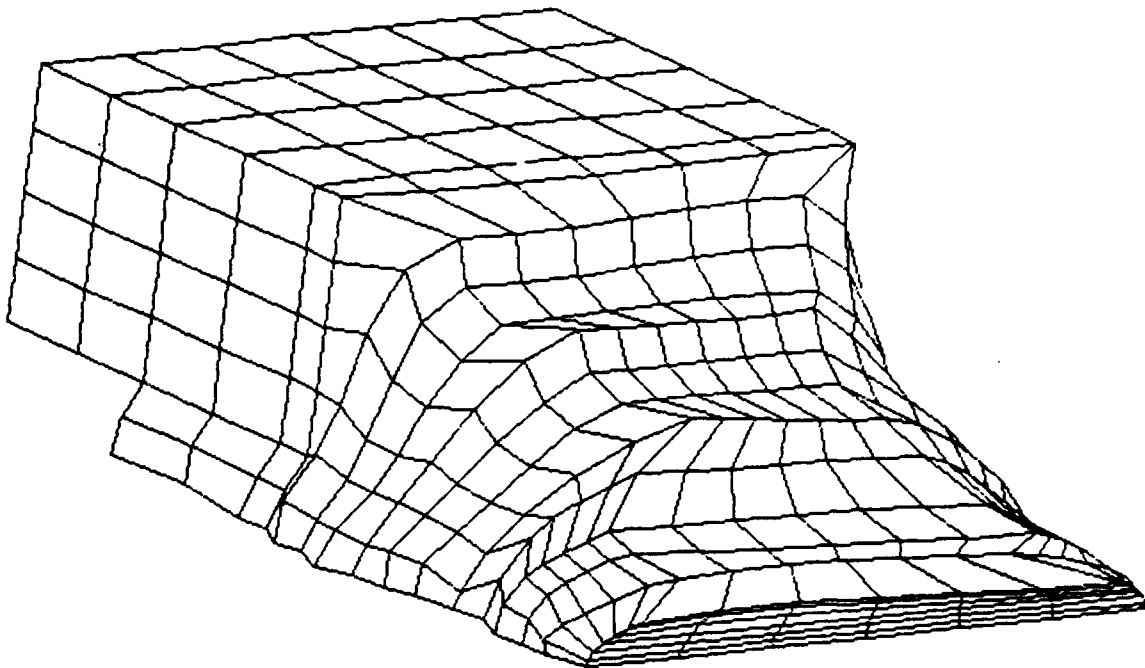


Figure 3.15 Finite element mesh (method 1)

```
INPUT CURSOR CONTROL COMMANDS TO DEFINE THE START OF THE TITLE
INPUT THE TITLE
FINITE ELEMENT MESH
```

END

HI

COMMAND NAME DISPLAY ACTIVE WINDOW VIEW DETACHMENT PLOT

SOLID MODEL

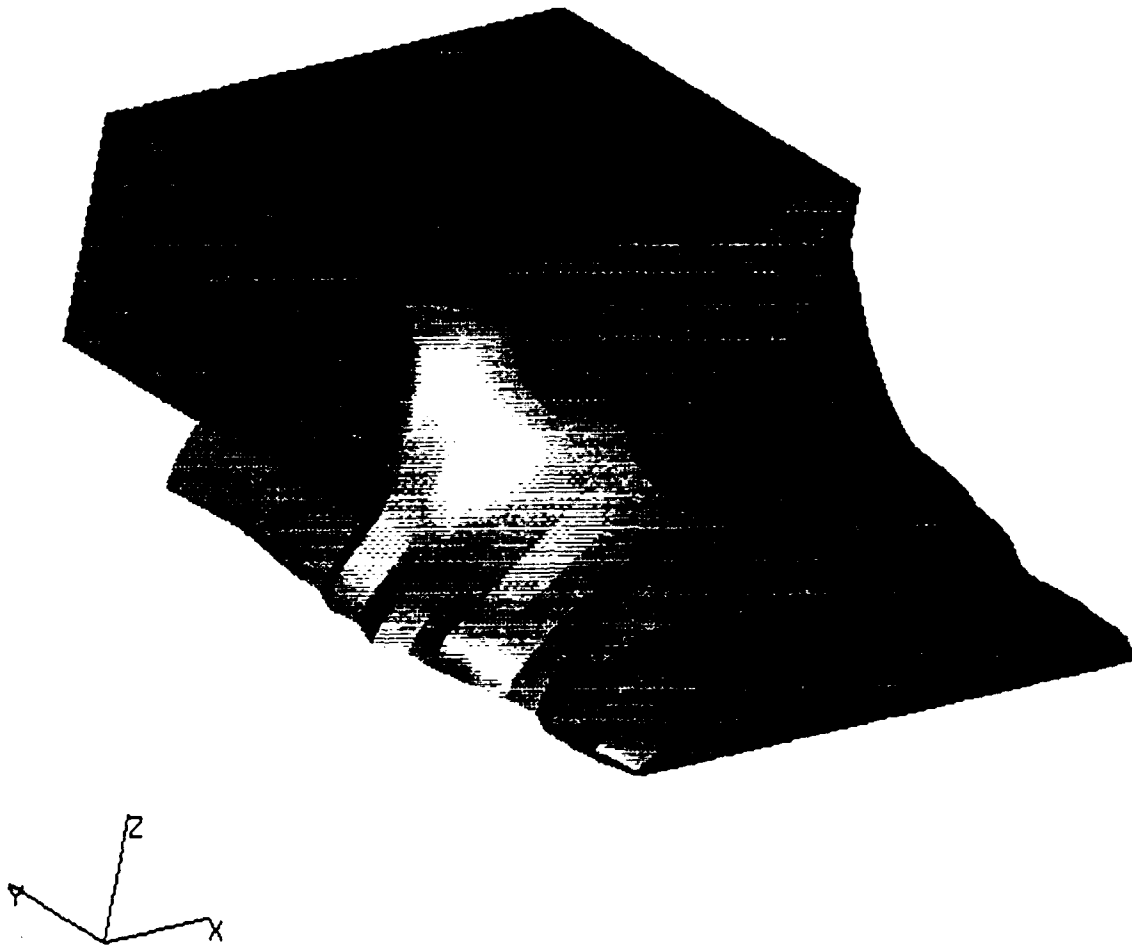


Figure 3.16 Solid model (method 1)

END OF VIEW

END

H

COMMAND NAME DISPLAY ACTIVE WINDOW VIEW SET CHG PLOT

LINES FITTED AND DRAWN TO THE GRID POINTS IN
SLICES 34 AND 36 OF THE SOLDER JOINT
IMAGED BY LASER VISION

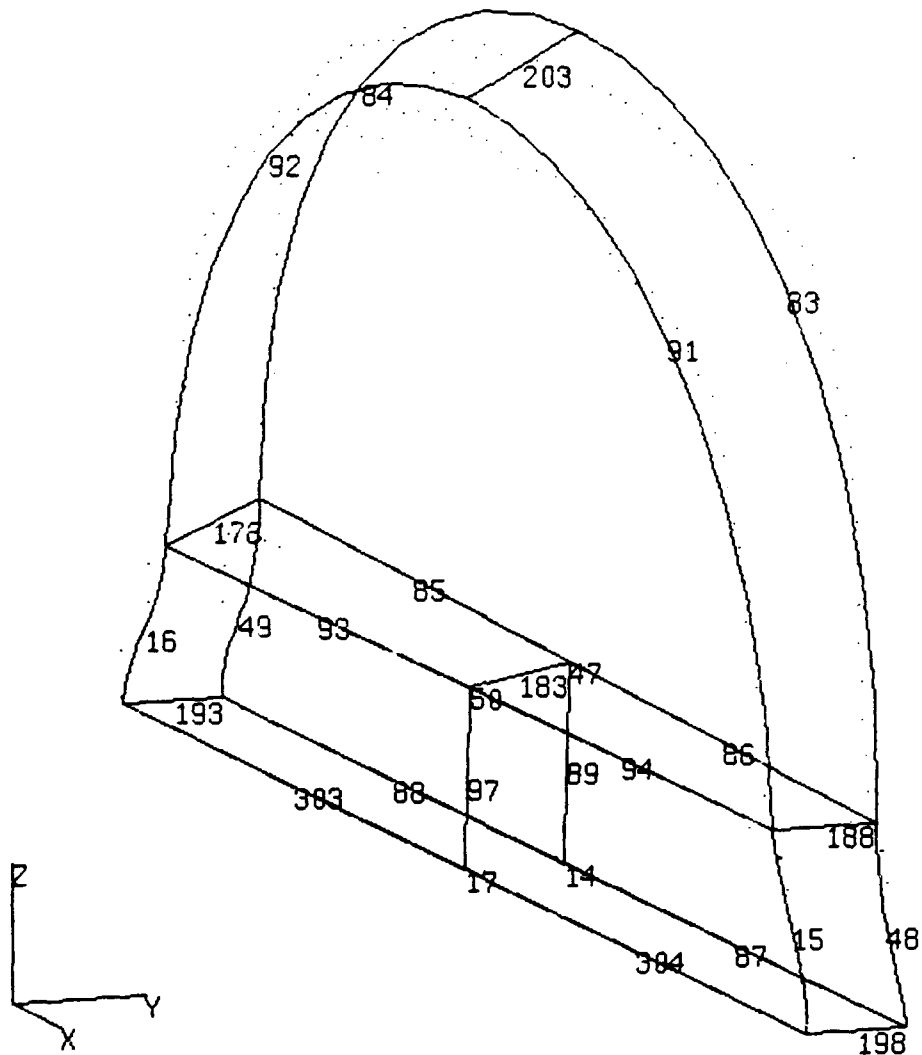


Figure 3.17 Line fitted and drawn to the grid points (method 2)

INPUT CURSOR CONTROL COMMANDS TO DEFINE THE START OF THE TITLE
INPUT THE TITLE
IMAGED BY LASER VISION

COMMAND NAME DISPLAY ACTIVE WINDOW VIEW SET/SHOW PLOT PATT

SURFACE PATCHES DEFINED BY THE LINES BETWEEN
SLICE 34 AND 36 OF THE SOLDER JOINT

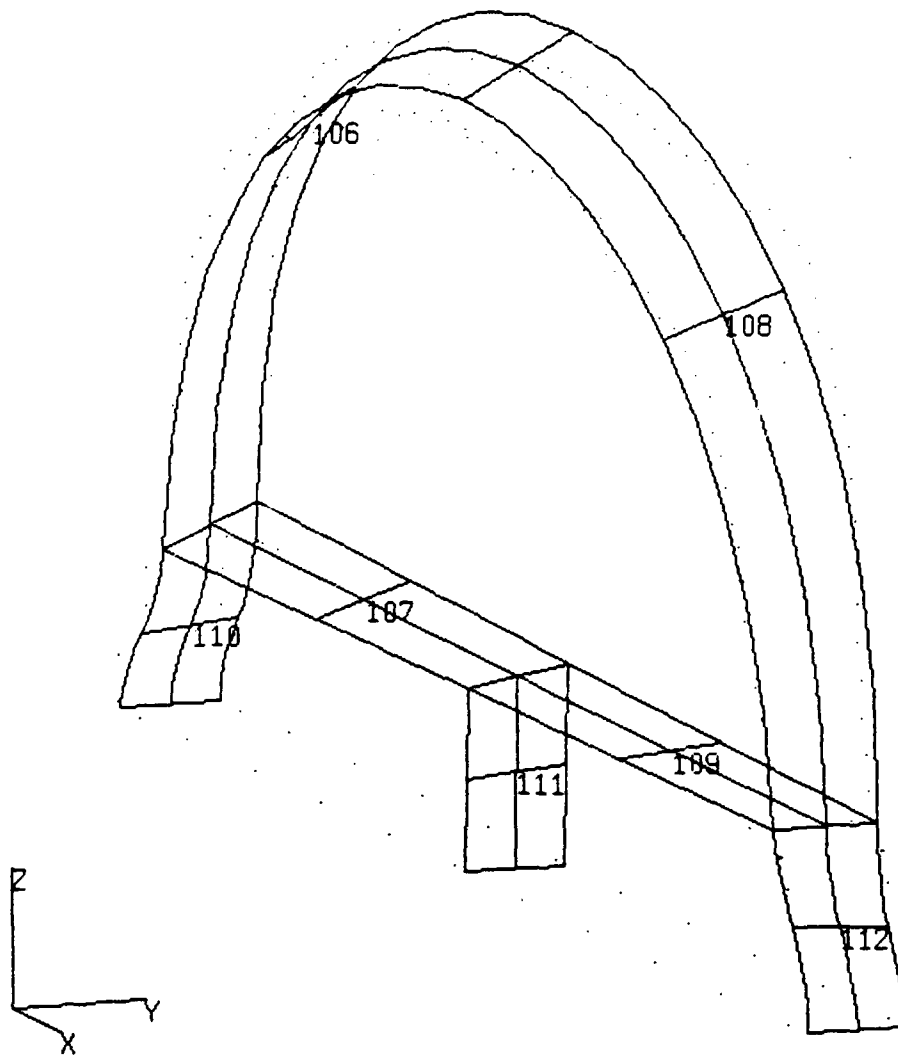


Figure 3.18 Surface patches defined by the lines (method 2)

INPUT CURSOR CONTROL COMMANDS TO DEFINE THE START OF THE TITLE
INPUT THE TITLE
SLICE 34 AND 36 OF THE SOLDER JOINT

END

H

COMMAND	NAME	DISPLAY	ACTIVE	WINDOW	VIEW	DET/CHOW	PLOT
---------	------	---------	--------	--------	------	----------	------

HYPERPATCHES DEFINED BY SURFACE PATCHES

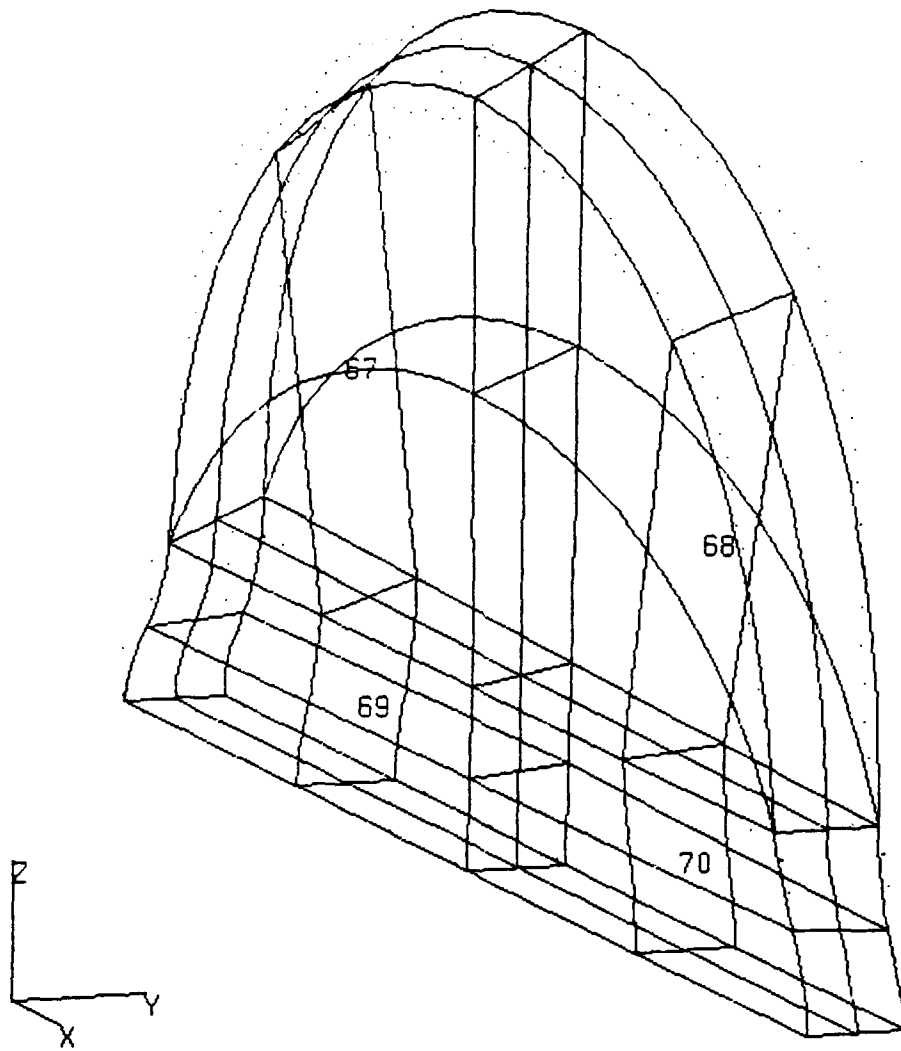


Figure 3.19 Hyperpatches defined by surface patches (method 2)

```

INPUT CURSOR CONTROL COMMANDS TO DEFINE THE START OF THE TITLE
INPUT THE TITLE
HYPERPATCHES DEFINED BY SURFACE PATCHES

```


COMMAND NAME DISPLAY ACTIVE WINDOW VIEW SET/SHOW PLOT HIDE

FINITE ELEMENT MESH

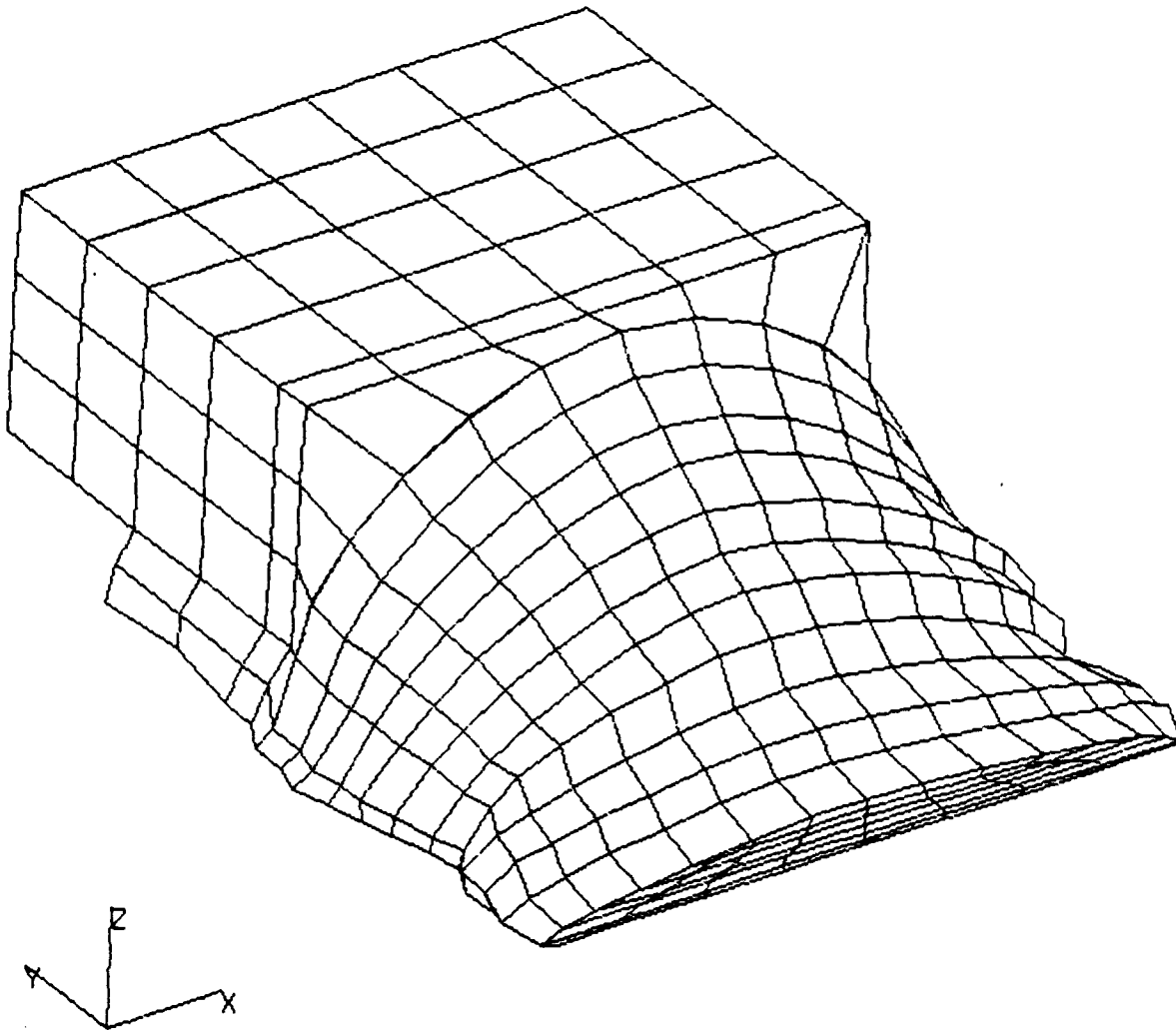


Figure 3.20 Finite element mesh (method 2)

INPUT CURSOR CONTROL COMMANDS TO DEFINE THE START OF THE TITLE
INPUT THE TITLE
FINITE ELEMENT MESH

END

HE

COMMAND

NAME

DISPLAY

ACTIVE

WINDOW

VIEW

SET/SHOW

PLOT

SOLID MODEL

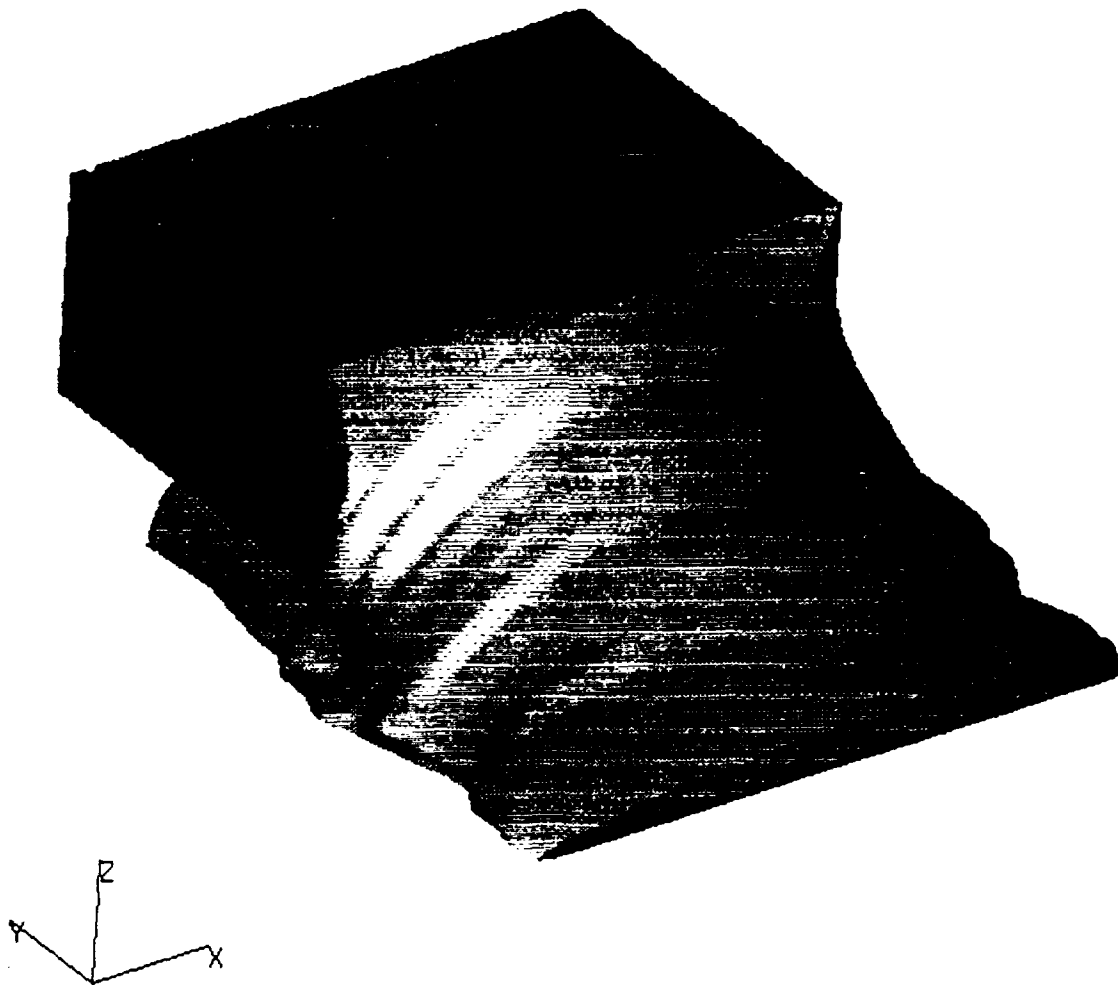


Figure 3.21 Solid model (method 2)

END OF FILE OR "END"

E/

4. ADDITIONAL RESULTS AND DISCUSSIONS

The results obtained from the Four Pi data appeared distorted when compared to the solder joint being imaged. Tests were performed on the Four Pi system to verify the severity of the distortion if in fact it does exist. The results of these tests are discussed below.

4.1 Repeatability

A repeatability test was done on a known solder object. A disk was filed down to produce the object shown in Figure 4.1. For this test the object was placed on a PWB. The PWB was loaded into the x-ray machine and serves to support the object during the test.

The purpose of the repeatability test is to compare the results of the boundary found for two different sets of laminographs. The two sets are taken of the same object on different days using the same camera settings. Also the same number of frame averages was used. The first set of x-rays was taken on 3 Dec. 1992, while the second was taken on 22 Jan. 1993. On each day the first slice was set at 5 mils above the board level. Additional slices were taken every 10 mils apart.

All laminographs were processed using a 5X5 median filter. A constant threshold value was used to find the boundary of the object. Because of the inability to accurately measure the relationship between the local coordinate system for each day and a global coordinate system, just the dimension of the object in the y direction was determined. The results are shown in Table 4. In

all slices the length found from the first set was greater than or equal to the length found from the second set.

4.2 Accuracy

Although the Four Pi system showed that results are repeatable, these same results show distortions of the object. These distortions are directly related to the nature of laminography and the hardware used to produce the images. Unlike previous reports (Adam, 1989, Siewert and Austin), our results showed incorrect height measurements in all reconstruction. Our incorrect height measurements agreed with a previous study (Black, 1991) of solder joint reconstruction from SBL images. The same known object used in the repeatability test shows this distortion in Figures 16. In the figure the known object is shown to scale with the 3-D mesh generated from the laminographs using the program. A distinct cone is seen above the object in Figure 4.2. Laminographs taken below the surface of the board would produce a similar cone only pointing downward. These results show solder at 75 mils above the top of the known object, or 170% higher than actual height. All of our 3-D reconstruction shows this distortion. This distortion is directly related to the nature of laminography and the Four Pi Systems hardware used to produce the images. The amount of distortion is a factor of camera settings and the image segmentation procedures as shown in Figure 4.3.

A surface mounted capacitor was imaged with Four Pi and processed as mentioned earlier. The 3-D mesh is shown in Figure 4.4. The model was produced by rejecting any slice that was above the z height of the top of the capacitor. A look at these rejected slices would show solder present at 10 mils of 42% higher than actual height. The distortion seen with the known object is also seen on the solder joint. Even with the slices rejected the results are far from accurate. The boundaries found are distorted to some degree, with the top laminographs producing greatly exaggerated boundaries (Figure 4.5). The view is from the side of the joint and the red line shows the maximum extent of the solder surface found from RVSI.

The same capacitor was imaged with RVSI and processed as mentioned earlier. The program is not complete, therefore only the solder below the top of the component was found and inputted into the session file. The 3-D mesh is shown in Figure 4.6. This is the first attempt in automated generation of 3-D finite element computer meshes for a solder joint using RVSI data. It can be seen that this model is a better reconstruction of the imaged solder joint than the reconstruction obtained from x-ray laminography.

4.3 Discussions

The tests conducted on the accuracy of the Four Pi system showed that the distorted 3-D finite element computer meshes are not a result of the program development. The distortions are directly related to the nature of laminography and the Four Pi Systems hardware used to produce the images. These distortions are so great that laminography is excluded as an inspection system that can assess the geometry of a solder joint for this project. The project course is now changed to use the RVSI HR-2000 as the primary image system. This will limit internal information as shown from summary of inspection system in Table 1.1. Later work may incorporate Four Pi Laminography for void presence and location.

Understanding the characteristics of solder joints will help to develop the knowledge base of Figure 3.1. This knowledge along with knowledge of manufacturing techniques is a key to generating more accurate computer meshes.

4.3.1 Four Pi Versus RVSI

Capabilities and limitations of manufactured object are inherit in the product output because of project goal, design criteria, and reliability standards. A comparison of the capabilities and limitations of the x-ray laminography and laser vision inspection system is shown below.

4.3.1.1 Four Pi System

Capabilities

- Only inspection system that can determine void locations
- High speed (100 milliseconds per image)
- Slice data is all in one plane on the z axis
- Provides solder data separate from the other solder joint constituents
- High resolution (.78 mils in x and y direction, while 1 mil in z direction)

Limitations

- Data is distorted
- Sharp corners are rounded off during the image acquisition stage
- Data is in discrete slices; therefore, important boundary transitions can be missed if these boundaries fall between slices
- Location of resistor and pad with respect to solder difficult to find

4.3.1.2 RVSI System

Capabilities

- High speed (12 joints per second)
- High resolution (0.1 mils in x, y, and z directions)
- Provides information on all solder constituents

Limitations

- System noise
- Missing data points in critical areas
- Has line of sight limitations; that is, what can not be seen can not be imaged
- Difficulty in separation of the data into the solder joint constituent groups

The RVSI HR-2000 limitations can be overcome with knowledge based information, however, the limitations of the Four Pi will be very hard if not impossible to overcome.

Table 4.1 Repeatability test results of the known object;. The difference between the measured y direction is shown along with the percentage this difference is of the actual length

Slice number	Distance above board level	Difference in pixels	Difference in percentage of actual length
1	5	4	2.3
2	15	3	1.7
3	25	1	0.7
4	35	1	0.7
5	45	0	0.0

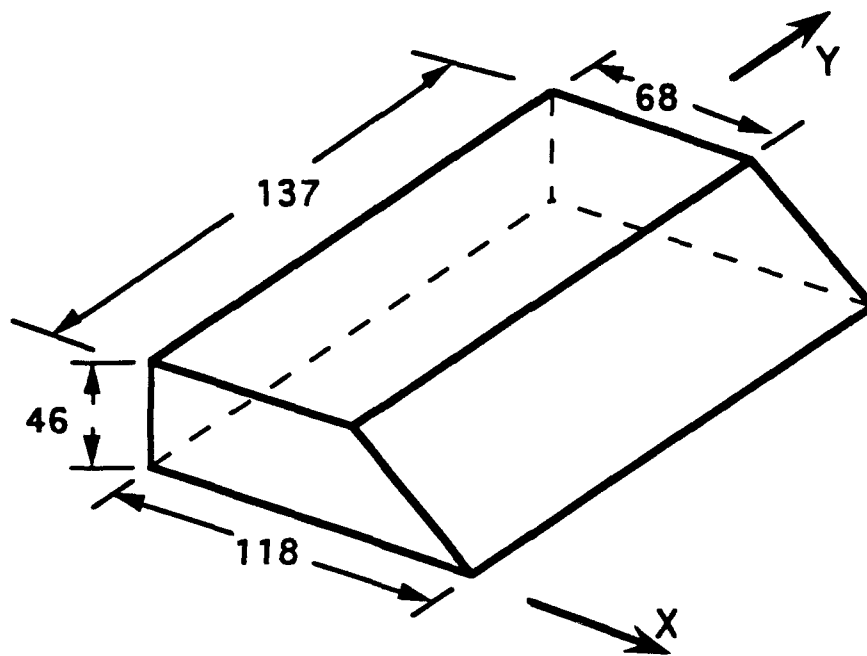


Figure 4.1 Dimensions (in mils) of known solder object

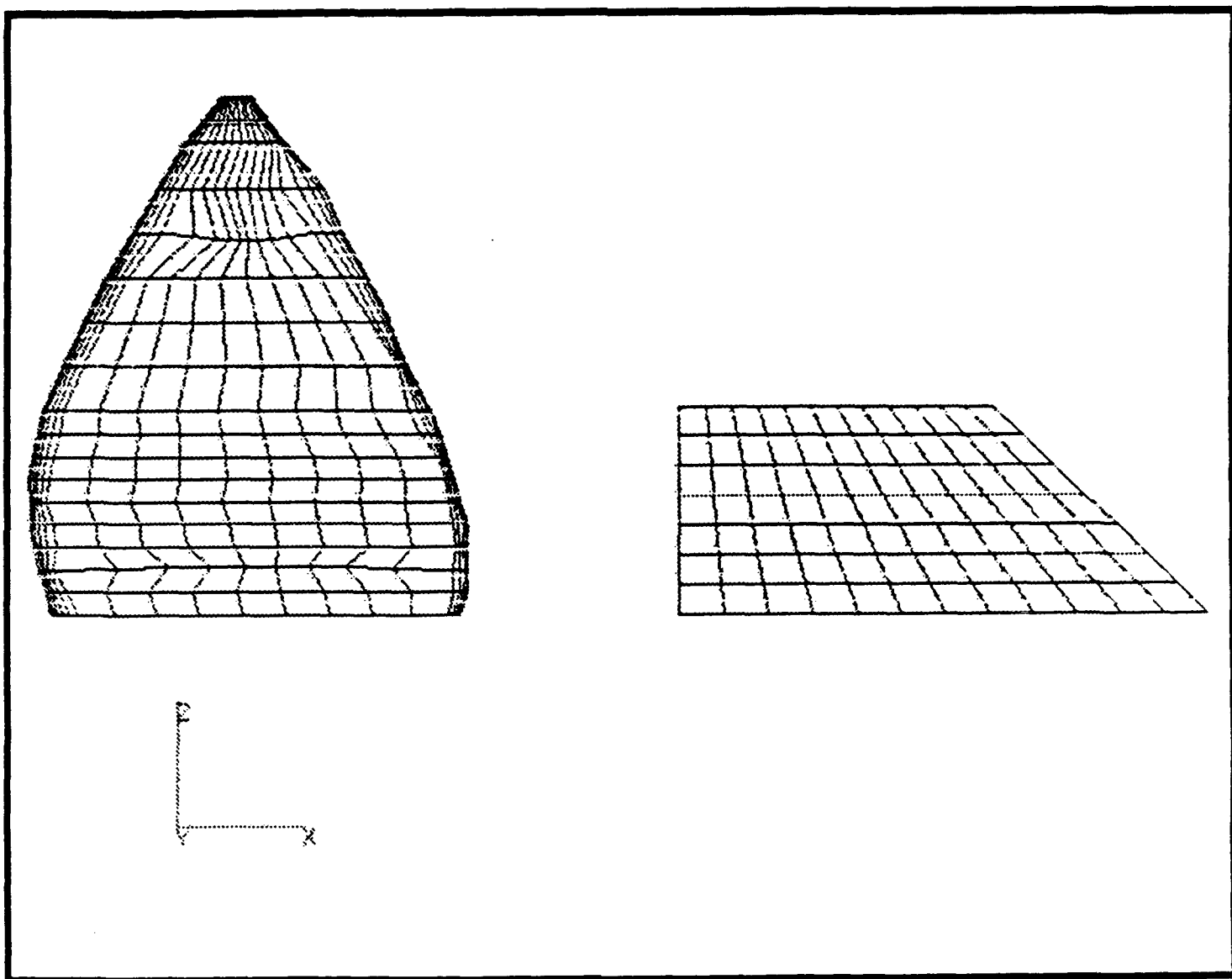


Figure 4.2. Comparison of known solder object with Four Pi imaging results

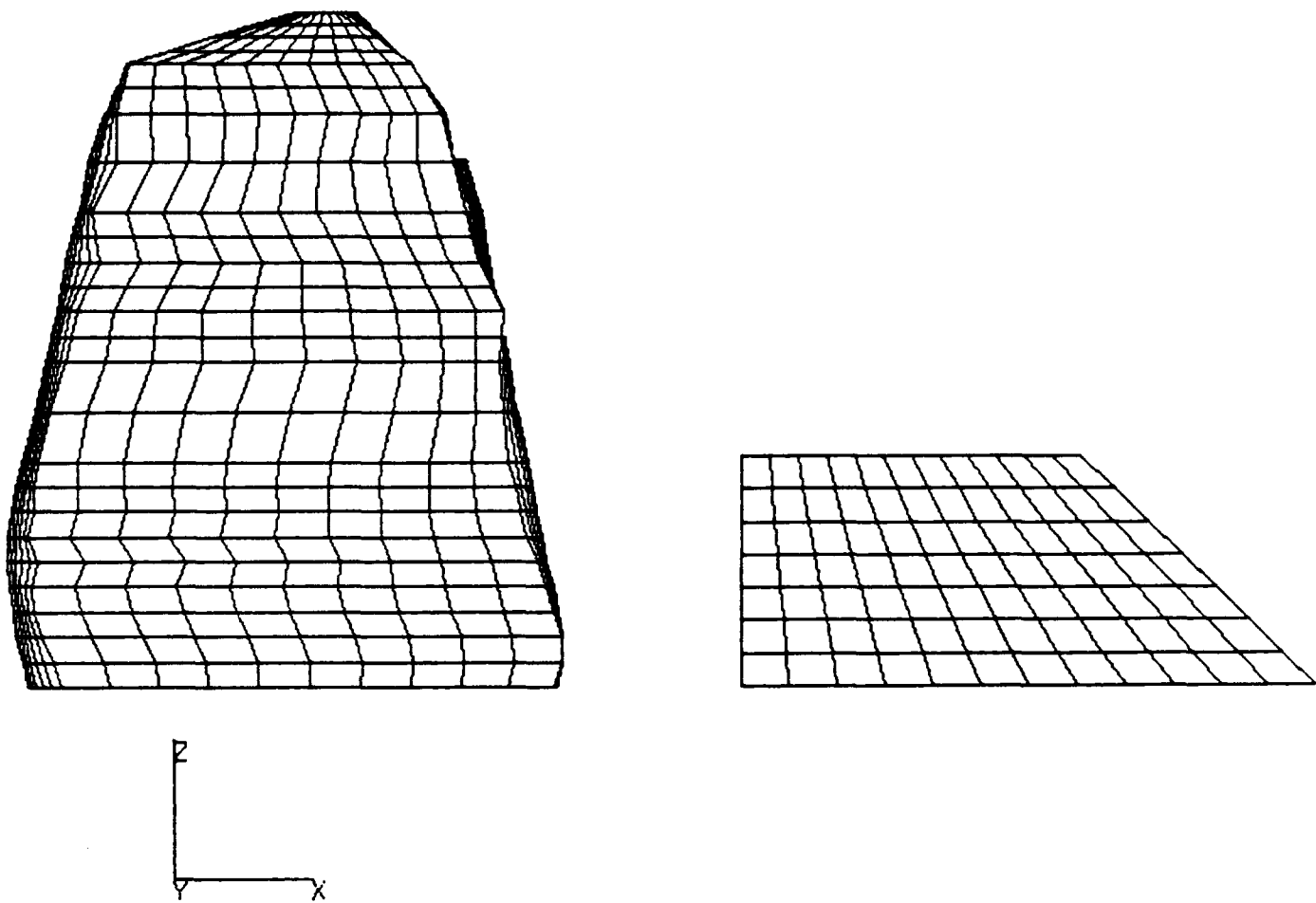


Figure 4.3. Different camera settings showing how the distortion can change for the same known solder object used in Figure 4.2

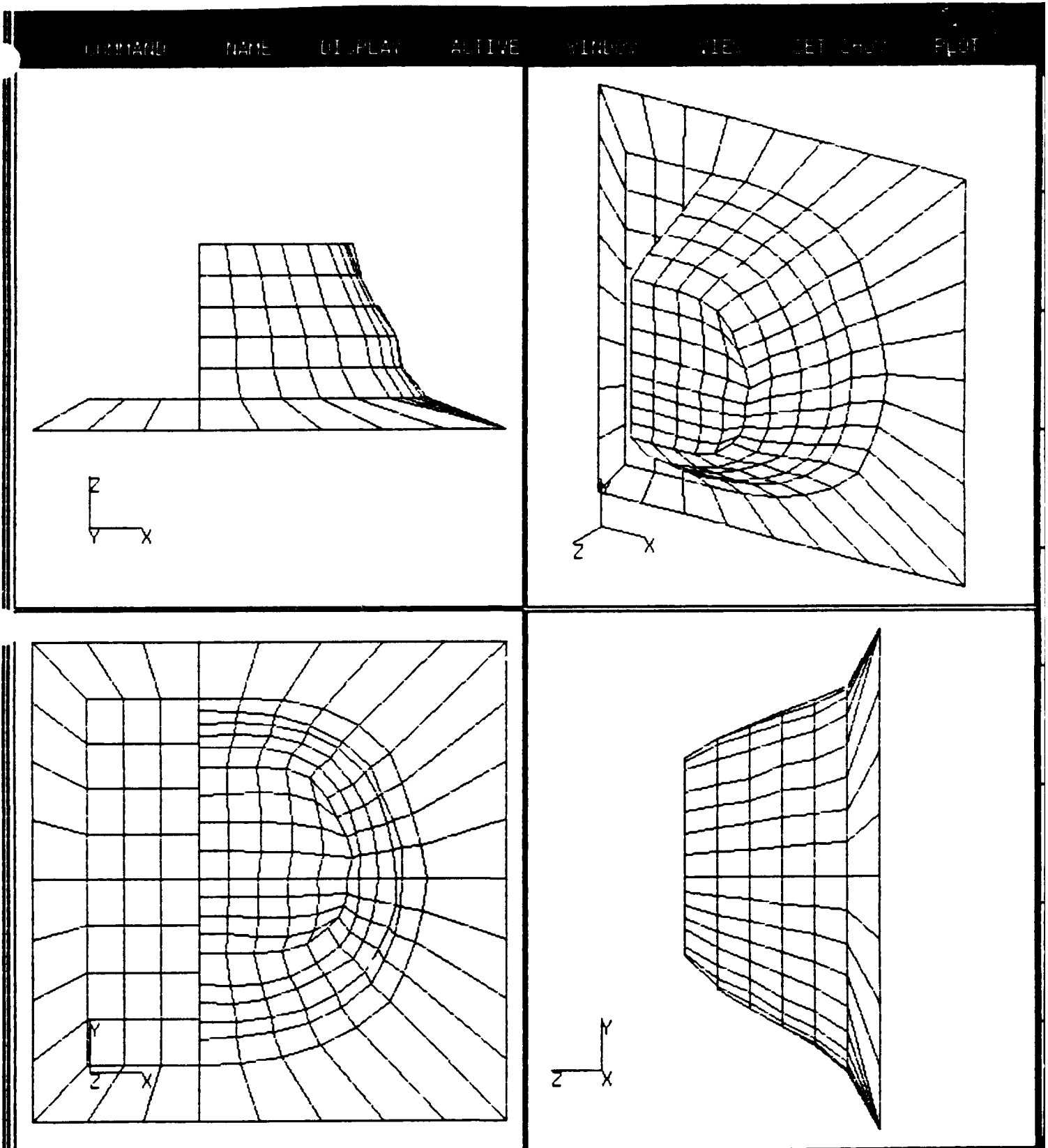


Figure 4.4. Mesh obtained from the modified program using Four Pi data

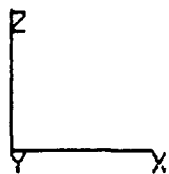
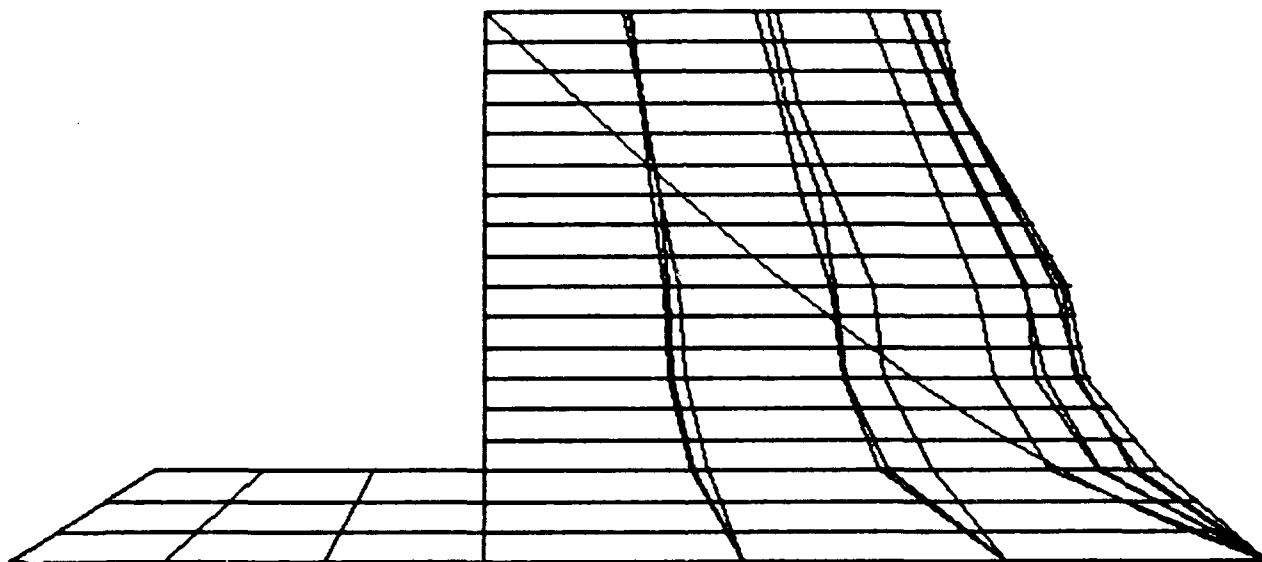


Figure 4.5. Side view comparison of Four Pi results (purple) to RVSI results (red)

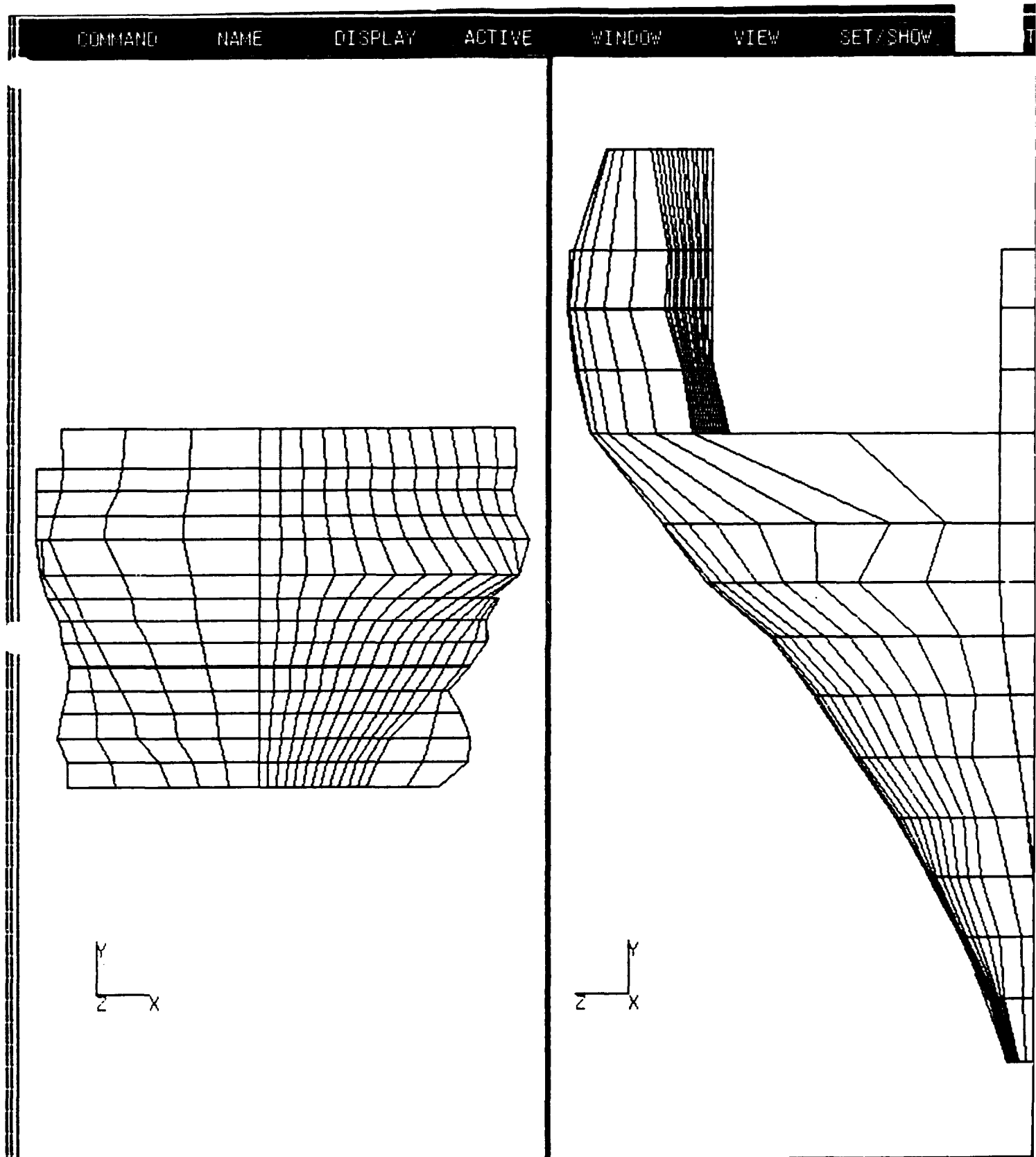


Figure 4.6. Mesh obtained from program using RVSI data

5. INTERACTIVE MESH GENERATION WITH RVSI DATA

An interactive method to generate 3D computer meshes is now being developed. The automated method failed to produce computer meshes because of several shortcomings of the program. The first shortcoming is the difficulty in separation of the data into the solder joint constituent groups. A surface-mount chip resistor (Figure 1.1) has five major constituent groups: board, pad, trace, resistor, and solder. The program needs to identify the boundary between the solder joint constituent groups before a computer mesh can be generated. These boundaries are between:

- Trace and board
- Trace and solder
- Trace and pad
- Pad and solder
- Pad and board
- Resistor and solder

The automated method had difficulty in accurately identifying two of the above listed boundaries. These two boundaries were the pad and solder, and the resistor and solder.

5.1 Problems with Locating Boundaries

The program determined the pad and solder boundary by looking at the data near the parameter edge of the pad. The pad's location is determined by looking at a portion of the pad that is not covered with solder. The data points that fall into this category are then averaged to determine the pad and solder boundary. Several assumptions are made using this method:

- The pad's surface is smooth with few irregularity.
- The board is not warped or twisted.
- The pad's local coordinate system is parallel to the inspection system's global coordinate system.

An investigation of these assumptions was done by inspection a pad before manufacturing the solder joint. The results show that the surface of the pad is not smooth. This surface is the boundary between the pad and solder. Table 5.1 shows selected portions of four slices from the pad inspection. Slice 17 is at the beginning of the pad (near the trace); whereas, slice 53 is at the end of the pad (portion of pad that would be covered by resistor). Because of the nature of the inspection system and the irregularities of the pad the number of data points that belonged to the pad ranged from 37 to 42. In the table below the last 20 pad data points are listed for each slice. The table shows the distance the pad surface is from the inspection system's global coordinate frame. This distance is in the z direction. The corresponding x coordinates vary for the data points of different slices. Because of this they are not included in the table.

The table shows that the pad surface may change by 2.1 mils. Also a 0.5 mil change between consecutive points is likely. This shows that one or more of the assumptions listed above are not true.

If the solder volume is large enough to cause the solder to be present near the top of the resistor or in some cases to extend over the top of the resistor, the boundary between the resistor and solder is extremely difficult to locate. The reason for this comes from several factors listed below:

- Irregularities in the resistor
- Noise in data
- Excessive solder
- Random scatter of data points
- Wide range of joint size and geometry
- Resistor not in alignment with the pads and board (i.e. resistor is rotated on one or more of it's three axes)

The automated method used four different method in locating the boundary between resistor and solder. Any one of the factors listed above can and did cause the program to select the improper boundary location. A program that could handle all the possible combination of the above factors, if it could be written, would be enormous in size and complexity.

5.2 User Interaction

An interactive method has been developed to overcome the problems with an automated method. A graphics library, SunPHIGS, is used to generate a window that will handle graphics applications. The program displays one slice of data points at a time. The user will view each slice and determine boundaries by flagging slices and picking data points off the screen. Once critical points are selected they will remain on the screen for any other slice viewed. This gives the user reference points to assist in location future critical points. Data points can be deleted and created by the user to overcome some of the factors listed above. Once boundaries and critical points are determined by the user the program automatically generates a session file to be used in the software PATRAN.

5.3 Generating the Mesh

The first mesh obtained from the interactive method is show in Figure 5.1. This finite element mesh consist of only the solder from the boundary of the trace and solder to the boundary of the resistor and solder. The solder joint imaged has excessive solder that has overflowed onto the trace during manufacturing. This is the reason for the abrupt end face at the small end of the mesh rather than the gentle slope of the solder surface down to pad level. The other abrupt end is the surface where the resistor is located. The mesh shown contains 2760 elements.

Table 5.1 Pad height of select portion of four slices from RVSI results

Slice 17 inch	Slice 31 inch	Slice 42 inch	Slice 53 inch
2.4470	2.4470	2.4471	2.4473
2.4467	2.4470	2.4471	2.4472
2.4476	2.4473	2.4465	2.4472
2.4462	2.4470	2.4467	2.4463
2.4467	2.4467	2.4468	2.4467
2.4467	2.4471	2.4467	2.4471
2.4467	2.4472	2.4467	2.4472
2.4466	2.4473	2.4471	2.4467
2.4475	2.4470	2.4470	2.4463
2.4472	2.4472	2.4472	2.4472
2.4467	2.4468	2.4468	2.4471
2.4470	2.4467	2.4472	2.4470
2.4472	2.4472	2.4470	2.4468
2.4473	2.4466	2.4473	2.4472
2.4471	2.4468	2.4466	2.4468
2.4475	2.4470	2.4468	2.4468
2.4471	2.4470	2.4471	2.4472
2.4476	2.4467	2.4468	2.4472
2.4473	2.4470	2.4477	2.4471
2.4478	2.4483	2.4476	2.4481

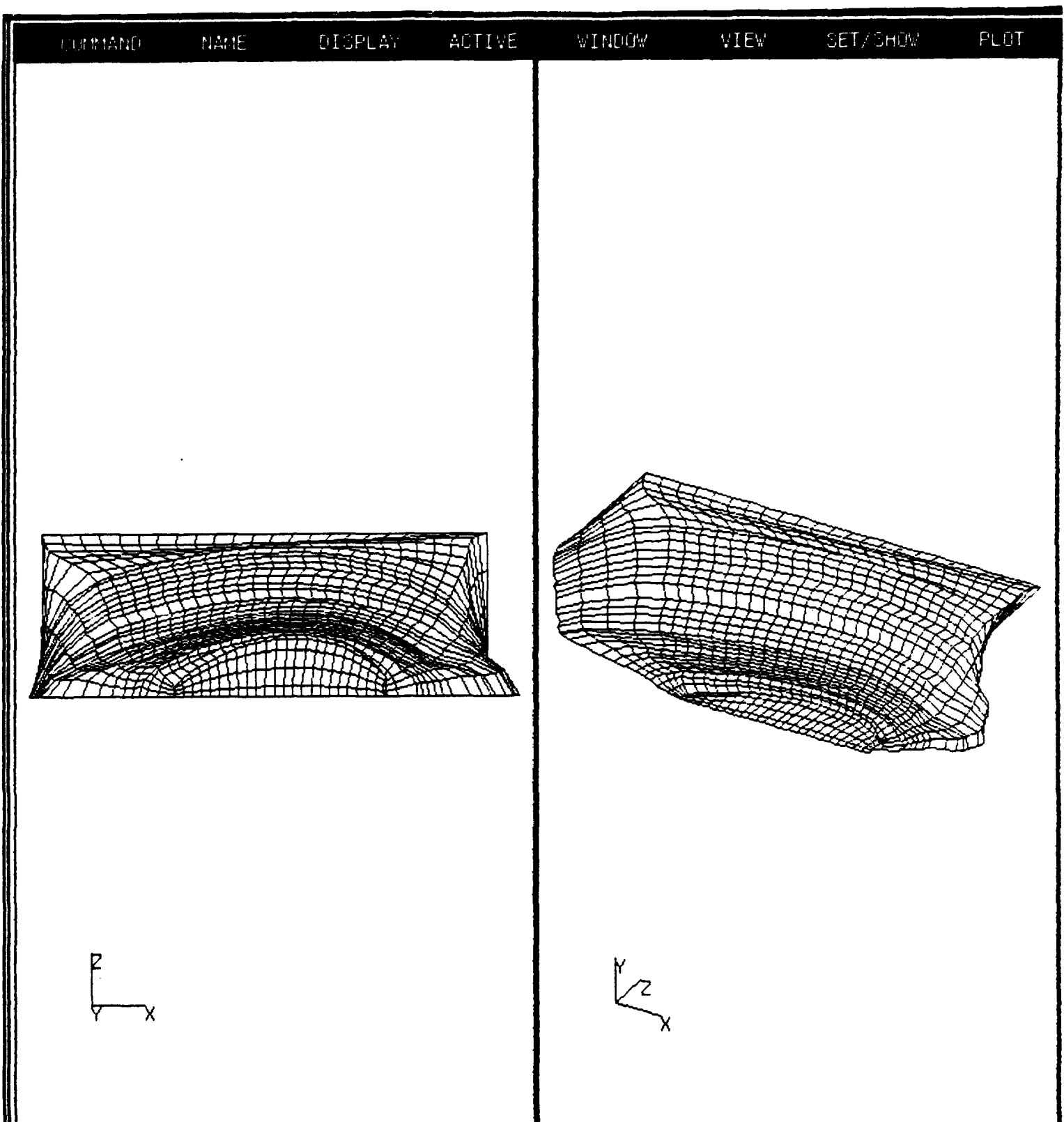


Figure 5.1 The finite element mesh obtained from the interactive method

6. CONCLUSIONS

The Four Pi system performed well in the repeatability test, however it performed poor in accuracy. It has the ability to show internal defects although the accuracy of the exact geometry of the defects may be questionable. The laminographic images contain characteristic distortions that are directly related to the nature of laminography and the hardware used to produce the images. These effects must be taken under consideration in order to build an accurate 3-D reconstruction. The Four Pi data must be processed to recover the distorted images before the reconstruction process begins. This may be accomplished by either using the existing drawings of packages, or the surface geometry provided by RVSI.

The Four Pi program works well with surface mounted capacitors. By adding new subroutines, data from other types of solder joints can also be processed. From the early stages the RVSI program has provided better reconstruction of the imaged solder joint than the Four Pi program. This is because of the large distortion of the x-ray laminography data. If a surface smoothing method or a better method to define the reconstructed surface can be written into a code then the RVSI data should be able to provide an accurate automated generation of 3-D finite element computer meshes for a solder joint.

The interactive mesh generation displays the flexibility to handle a verity of solder joint sizes and shapes. In development of the mesh unwanted data points were deleted and new data points were generated. Key data points were selected and then the program automatically generated a session file to produce the mesh shown in Figure 5.1. Work is in progress to further investigate this algorithm (Boehmer, 1993).

REFERENCES

Adams, John, "New 3-D X-Ray System Provides Real-Time Data for Solder Quality Process Control", Presented at the *Surface Mount 89 Exposition and Conference*, San Jose, CA, Aug. 28-31, 1989.

Black, S., "Solder Joint Reconstruction from Scanned-Beamed Laminography Images", *Master's Thesis* submitted to Rensselaer Polytechnic Institute, Troy, NY, Aug. 1991.

Boehmer, W., "Automated Generation of 3-D Finite Element Meshes from Solder Inspection Systems", *Master's Thesis*, Department of Mechanical Engineering, IUPUI, Indianapolis, Indiana, 1993 (to be completed).

Millard, Don L., "Solder Joint Inspection". *Electronic Materials Handbook*, ASM International, Volume 1, 1989, pp. 735-739.

Read, David T. and Lucey, George K., Jr., "Automated Finite Element Mesh Generation for SMT Solder Joints", Presented at the ASME Winter Annual Meeting, Dallas, TX, Nov. 25-30, 1990, ASME Paper No. 90-WA/EEP-31, *ASME Journal of Electronic Packaging*, Vol. 113, Jun. 1991, pp. 178-185.

Siewert, T. A. and Austin, M. W., "Evaluation of Four Pi X-ray Laminography System", *A Report to Harry Diamond Laboratory from the Materials Reliability Division of NIST*.

APPENDIX A

Session Files for PATRAN

The session file is a list of commands written in card image format. The first three lines are for the initialization of PATRAN. The first line, "GO", signals the program to start a normal run. The second line, "1", defines that a new PATRAN execution is to begin, rather than a restart of an old PATRAN execution. The third line, "SET,LAB1,OFF", turns off all geometry model labels, including LABG, LABL, LABP, LABH. What this means is that the labels of geometric entities - grid, line, patch, and hyperpatch - are not displayed along with their corresponding entity.

The remainder of the session file is divided into four sections. The largest section is the grid generation commands. The x, y, and z coordinates are left in units of pixels. This allows the reader to easily visualize the object generated. Remember that each entry is a pixel that was flagged as being the solder boundary. The next section is the line generation commands. The program uses two different line generation commands. One command is the two grid, 2G, method, the other is the best fit, FIT, method. In the two grid method a straight line is generated from first grid point the second grid point. In the best fit method a line is generated from a least square approximation for the grid points listed. The third section is the patch generation commands. A patch is an area defined by four grid points, QUAD, as the corner locations of a rectangle, or an area defined by four lines, EDGE, as the perimeter of the area. The last section is the hyperpatch generation commands. A hyperpatch is a volume defined by two patches, 2P, as the surface faces of two opposite faces of a three-dimensional object.

GO

1

SET,LAB1,OFF

GRID,1,,281/261/0

GRID,2,,307/261/0

GRID,3,,350/261/0

GRID,4,,350/227/0

GRID,5,,350/192/0

GRID,6,,307/192/0

GRID,7,,281/192/0

GRID,8,,281/227/0

GRID,9,,307/227/0

GRID,10,,307/256/5

GRID,11,,309/256/5

GRID,12,,311/256/5

GRID,13,,314/256/5

GRID,14,,315/256/5

GRID,15,,316/256/5

GRID,16,,317/256/5

GRID,17,,318/256/5

GRID,18,,319/256/5

GRID,19,,320/256/5

GRID,20,,321/256/5

GRID,21,,322/255/5

GRID,22,,323/255/5

GRID,23,,324/255/5

GRID,24,,325/255/5

GRID,25,,326/255/5

GRID,26,,327/254/5

GRID,27,,328/254/5

GRID,28,,329/254/5

GRID,29,,330/253/5

GRID,30,,331/253/5

GRID,31,,332/252/5

GRID,32,,333/252/5

GRID,33,,334/251/5

GRID,34,,335/250/5

GRID,35,,336/249/5

GRID,36,,337/248/5

GRID,37,,338/247/5

GRID,38,,338/246/5

GRID,39,,339/245/5

GRID,40,,339/244/5

GRID,41,,340/243/5

GRID,42,,340/242/5

GRID,43,,340/241/5

GRID,44,,341/240/5

GRID,45,,341/239/5

GRID,46,,342/238/5

GRID,47,,342/237/5
GRID,48,,342/236/5
GRID,49,,342/235/5
GRID,50,,343/234/5
GRID,51,,343/233/5
GRID,52,,343/232/5
GRID,53,,343/231/5
GRID,54,,343/230/5
GRID,55,,343/229/5
GRID,56,,344/228/5
GRID,57,,344/227/5
GRID,58,,344/226/5
LINE,1,2G,,1,2
LINE,2,2G,,2,3
LINE,3,2G,,3,4
LINE,4,2G,,4,5
LINE,5,2G,,5,6
LINE,6,2G,,6,7
LINE,7,2G,,7,8
LINE,8,2G,,8,1
LINE,9,2G,,8,9
LINE,10,2G,,9,2
LINE,11,2G,,9,4
LINE,12,2G,,9,6
LINE,13,FIT,,10T37
LINE,14,FIT,,37T57
LINE,15,2G,,57,106
LINE,16,FIT,,57T77
LINE,17,FIT,,77T105
LINE,18,2G,,105,106
LINE,19,2G,,10,106
LINE,20,FIT,,110T134
LINE,21,FIT,,134T152
LINE,22,2G,,152,195
LINE,23,FIT,,152T169
LINE,24,FIT,,169T194
LINE,25,2G,,194,195
LINE,26,2G,,110,195
LINE,27,FIT,,196T199/201T221
LINE,28,FIT,,221T238
LINE,29,2G,,238,278
LINE,30,FIT,,238T253
LINE,31,FIT,,253T277
LINE,32,2G,,277,278
LINE,33,2G,,196,278
LINE,34,FIT,,279T299/301T304
LINE,35,FIT,,304T319
LINE,36,2G,,319,355
LINE,37,FIT,,319T332

LINE,38,FIT,,332T354
LINE,39,2G,,354,355
LINE,40,2G,,279,355
LINE,41,FIT,,356T376
LINE,42,FIT,,376T390
LINE,43,2G,,390,421
LINE,44,FIT,,390T401
LINE,45,FIT,,401T420
LINE,46,2G,,420,421
LINE,47,2G,,356,421
LINE,48,FIT,,422T438
LINE,49,FIT,,438T451
LINE,50,2G,,451,477
LINE,51,FIT,,451T459
LINE,52,FIT,,459T476
LINE,53,2G,,476,477
LINE,54,2G,,422,477
PATCH,1,EDGE,,1/10/9/8
PATCH,2,EDGE,,2/3/11/10
PATCH,3,EDGE,,7/9/12/6
PATCH,4,EDGE,,12/11/4/5
PATCH,5,QUAD,,109/10/106/108
PATCH,6,QUAD,,108/106/105/107
PATCH,7,EDGE,,13/14/15/19
PATCH,8,EDGE,,16/17/18/15
PATCH,9,EDGE,,20/21/22/26
PATCH,10,EDGE,,22/23/24/25
PATCH,11,EDGE,,27/28/29/33
PATCH,12,EDGE,,29/30/31/32
PATCH,13,EDGE,,34/35/36/40
PATCH,14,EDGE,,36/37/38/39
PATCH,15,EDGE,,41/42/43/47
PATCH,16,EDGE,,43/44/45/46
PATCH,17,EDGE,,48/49/50/54
PATCH,18,EDGE,,50/51/52/53
HPAT,1,2P,,1,5
HPAT,2,2P,,3,6
HPAT,3,2P,,2,7
HPAT,4,2P,,4,8
HPAT,5,2P,,7,9
HPAT,6,2P,,8,10
HPAT,7,2P,,9,11
HPAT,8,2P,,10,12
HPAT,9,2P,,11,13
HPAT,10,2P,,12,14
HPAT,11,2P,,13,15

APPENDIX B

List of Participants of the Project

The following personnel participated during this project:

1. Nasser H. Paydar, Ph.D.
Principal Investigator
2. Hasan U. Akay, Ph.D.
Co-principal Investigator
3. Yihong Tong, Ph.D.
Post-Doctorate Research Associate
4. William Boehmer
Graduate Research Assistant
5. David Wetsel
Undergraduate Research Assistant

As a result of his participation in this project, William Boehmer is expected to complete his Master's thesis by the end of 1993. No inventions or copyrighted materials resulted with this project.

APPENDIX C

List of Publications

The following research papers, directly related with this project, were published in technical journals and conference proceedings.

1. N. Paydar, H.U. Akay and Y. Tong, "Thermal Stress Analysis of an SMT Solder Joint Using a Creep-Plasticity Model," *Proceedings of ELECTRECON' 91*, Indianapolis, Indiana, October 22-23, 1991.
2. H.U. Akay, Y. Tong, and N. Paydar, "Thermal Fatigue Analysis of a SMT Solder Joint Using Nonlinear FEM Approach," *IEPS Electronics Packaging Conference*, Austin, Texas, September 27-30, 1992.
3. H.U. Akay, Y. Tong, and N. Paydar, "Thermal Fatigue Analysis of an SMT Solder Joint Using Nonlinear FEM Approach," *International Journal of Microcircuits and Electronic Packaging*, Vol. 16, No. 2, 1993.
4. N. Paydar, Y. Tong, and H.U. Akay, "A Finite Element Study of Fatigue Life Prediction Methods for Thermally Loaded Solder Joints," *ASME International Electronic Packaging Conference*, Binghamton, New York, September 29-October 2, 1993.
5. N. Paydar, Y. Tong, and H.U. Akay, "A Finite Element Study of Factors Affecting Fatigue Life of Solder Joints," *ASME Journal of Electronic Packaging* (submitted for review, November 1992).
6. W. Boehmer, "Automated Generation of 3-D Finite Element Meshes from Solder Inspection Systems," *Master's Thesis*, Department of Mechanical Engineering, IUPUI, Indianapolis, Indiana, 1993 (to be completed).